University of Naples Federico II
School of Polytechnic and Basic Sciences

Department of Structures
for Engineering and Architecture

Ph.D. Programme in Materials and Structures
XXVIII Cycle

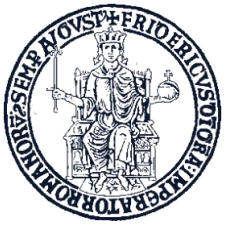

Giancarlo Ramaglia

Ph.D. Thesis

SEISMIC STRENGTHENING OF SLENDER MASONRY BARREL VAULTS: EXPERIMENTAL BEHAVIOUR AND ANALYTICAL MODELLING

Tutor: Prof. Ing. Gian Piero Lignola

2016

Acknowledgements

I want to express all my gratitude to Prof. Gian Piero Lignola for his encouragement, interest and unwavering guidance and will be in the future, an example for me. It was because of his intuition and constant support that the development of my work has been possible.

Special thanks go to Prof. Andrea Prota for his thoughtful support of my work and precious advices during these three years.

I would express my gratitude to Prof. Gaetano Manfredi that gave me the opportunity to be part of an outstanding working team, in particular of the PRIN 2010-2011 (Advanced mechanical modelling of new materials and technologies for the solution of 2020 European challenges).

I am also particularly grateful to the PON-PROVACI project (Technologies for earthquake protection and valorisation of cultural heritage sites); some of the activities presented in this work were developed there. I want to express my thanks to Stress s.c.a r.l. group for their constant support in these years.

Furthermore, a devoted gratitude is to: Prof. Francesca Ceroni, Prof. Giuseppe Maddaloni, Prof. Francesco Russo Spena, Prof. Luigi Di Sarno, Prof. Maria Rosaria Pecce, Prof. Renata Picone and Prof. Valentina Russo; working with them was particularly stimulating.

I want to thank past and present colleagues, in particular: Anna Bozza, Claudio D'Ambra, Claudio Balestrieri, Vincenzo Giamundo, Daniele Losanno, Iolanda Nuzzo, Nunzia Iuliano and Umberto Vitiello.

I want to express my gratitude to my friends: Angela Iodice, Nicola Piramide, Maria Ranisi, Francesco Ricciardiello and Michele Russo who directly or indirectly supported me during this period.

I would express my thanks to my family for their constant presence. Special thank go to Chiara for her sacrifice and constant encouragement.

Finally, thanks to all the members of staff of the Department of Structures for Engineering and Architecture at the University of Naples Federico II.

Without these people this thesis would not have been completed.

Naples, 30/03/2016 *Giancarlo Ramaglia*

Abstract

A significant part of the world cultural heritage is represented by masonry buildings. Many of them are characterized by a complex architecture like as religious buildings and need to be preserved, both from a historical and structural point of view.

The recent earthquakes showed the seismic vulnerability of existing buildings stock. This is an important issue especially for buildings located in high seismic risk zones. The seismic action causes damages in the masonry, hence the reduction of the load capacity and stiffness. These aspects yield to changes in the dynamic and non-linear behaviour.

Furthermore, high-damage has been relieved for heritage building stock, in particular when there are thrusting elements like as arches and vaults.

Over the past years, several innovative materials and technologies have been developed to limit the effects of earthquakes on the masonry structures. The use of composite materials showed to be effective for most structures. In particular, the latest earthquakes have led to manufacturing specific and innovative retrofitting strategies. However, seismic retrofitting measures of historical masonry buildings are not straightforward in terms of compatibility with existing materials, of efficiency and safety.

In this background, the numerical analyses and experimental simulations provide important information about the seismic behaviour of these structures. Furthermore, also the increase of load capacity by means of strengthening systems can be estimated using these theoretical and practical instruments.

Unfortunately, the masonry buildings are characterized by a wide variability in response (construction techniques, regularity, etc.) which are complex to simulate and predict in numerical analyses (like as micro or macro-modelling, FEM-based).

The actual structural response of a masonry building should take several parameters into account, difficult to implement into a numerical model

especially when applied on heritage buildings (where there are vaults and arches).

Furthermore, these approaches not compatible with the common practice, where it is useful to have simplified calculation approaches to estimate seismic capacity of masonry structures with or without strengthening systems.

Therefore, the numerical analysis performed on masonry structures shows some drawbacks.

The Ph.D. thesis starts from a vulnerability study at regional level. This analysis on a typical historical centre located in the Italian region has been performed. This is a preliminary study in order to assess the main parameters which cause vulnerabilities. The result remarks the influence of local mechanisms in the existing masonry buildings, when there are thrusting elements.

For this reason, a structural assessment of masonry vaults, by using a detailed modelling, has been performed.

The work focuses on a particular typology of barrel vaults typically used as roofs in religious buildings. These vaults typically do not include any backfill and are slender. These barrel vaults cannot be analysed through the classical approaches where no-tensile strength is assumed. The tensile strength must be included to assess the seismic capacity.

Therefore a simplified analytical model, in the framework of limit analysis, is proposed which includes the tensile strength. Tensile strength in these analyses is not only affected by the strength of basic materials, but also by the bond at the unit-to-joint interfaces, which could be rather difficult to assess reliably. The proposed model is useful to have simplified calculations to estimate the increase in capacity of vaulted masonry due to the strengthening interventions.

The validation of the analytical model was provided by comparing predictions of the load capacity and the failure mode with those obtained

from shaking table tests. The dynamic test used to validate the analytical model has been performed on a full scale masonry vault, previously tested. In fact, the experimental tests can provide an efficient contribution to the calibration and interpretation of the numerical models. The experimental analysis and numerical modelling comparison are not the only way to improve the understanding of the structural behaviour. They represent a first step towards the development of simplified calculation methods to estimate the capacity of vaulted structures.

Starting from the validation of the proposed analytical model, sensitivity analyses have been performed in order to assess the impact of some mechanical and geometrical parameters on the seismic capacity. These analyses were performed using the proposed analytical model.

Furthermore, the model, previously validated, has been used in order to design dynamic tests on another masonry vault. The proposed method represents a useful modelling tool to design dynamic tests on masonry vaults and to assess their vulnerability.

The physical and mechanical characteristics of the arch profile are similar to the vault previously tested. Conversely, as it will be clarified by following discussion, the global geometry is different.

The dynamic response of the specimen has been investigated by using the shaking table system, before and after application of strengthening systems. In particular, after suffering damage, the vault was repaired and strengthened. Then the strengthened specimen was tested again.

The strengthening techniques are based on TRM system (Textile Reinforced Mortar) in addition to traditional strengthening techniques (steel ties and masonry ribs). The performance of the strengthening vault was assessed comparing the behaviour of two specimens (unreinforced and strengthening) during the several tests. In order to support the experimental studies, several FEM analyses have been performed additionally to the simplified modelling.

The results are intended as a contribution to the understanding of dynamic behaviour and towards the development of simplified models to estimate seismic capacity of vaulted structures.
The experimental results remark the effectiveness of the TRM system coupled with traditional interventions (masonry rib and unidirectional steel tie). In particular, the strengthening system is particularly advisable to safeguard of heritage buildings.
In fact, given the high efficiency and compatibility of the strengthening techniques experimentally used, they have been implemented in a real heritage building (Monastery of Santo Spirito, Ocre (Italy)).

KEYWORDS: *Simplified modelling, Barrel vaults, Arch, Shaking table test, Experimental validation, Strengthening systems, Heritage buildings, Seismic capacity assessment*

Summary

List of tables

List of figures

Chapter 1

INTRODUCTION: OVERVIEW OF MASONRY STRUCTURES

The Egyptian Pyramids, the Colosseum in Rome, the Great Wall of China, are only some of the world's most significant architectural works built with masonry material. The designers have chosen masonry for its durability, versatility and sustainability.

The knowledge of buildings, starting from their history, may provide some important information. It is an essential tool in order to plan retrofit strategies and mitigation of seismic risk into the existing urban areas. The historical assessment is a preliminary strategy less frequently done. Generally, only for heritage buildings an approach based on advanced knowledge is performed.

Given the critical conditions which are typical of existing building stock, planned preventive maintenance and strengthening interventions must be performed. Therefore, the continuing need for every historical centre to be preserved cannot ignore the historical assessment.

Is interesting to note that, in a background where the reinforced concrete (r.c.) structures are threatened by corrosion effects, both the restoration and retrofit of masonry buildings appear a key opportunity. For this reason, an increasing interest will be allocated to the existing masonry structures.

However, the recent seismic events showed the vulnerability of masonry buildings, especially of heritage masonry buildings.

This first part focuses on some main issues typical of existing masonry structures. Some critical aspects were addressed with a broader view.

Finally, starting from an analysis at regional level, the key sources of vulnerability were assessed for existing masonry structures. For this

reason, a typical historical centre located in Italian region has been chosen to estimate the main vulnerability parameters.

1.1. Vulnerability of existing buildings

The safeguard of existing buildings, with particular reference to prevention strategies and mitigation of seismic risk, is currently an issue of great interest for existing building stock. The recent seismic events showed the strong vulnerability of most of existing structures, especially for heritage masonry buildings (figure 1.1).

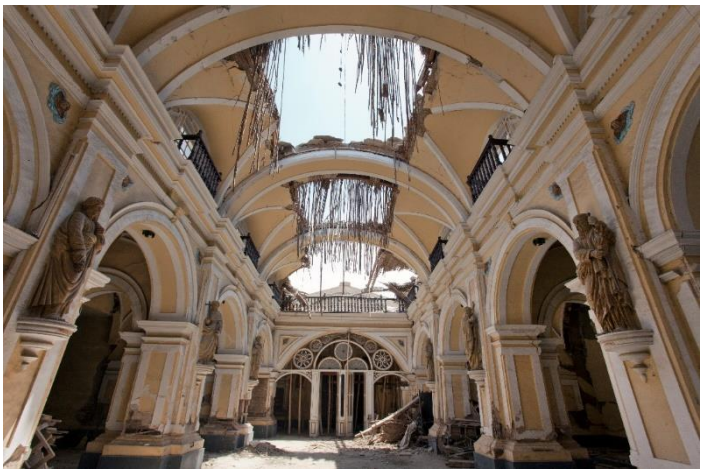

Figure 1.1: *Cathedral of Ica, Ica (Peru), damages after 2011-Earthquake.*

Many issues appear to be caused by the strong variability of the physical and mechanical parameters, which may be detected in the existing building stock.

The assessment of the actual susceptibility of existing masonry structures to be damaged by seismic actions requires complex procedures. In fact, these buildings are characterized by a strong non-homogeneity of construction techniques and by a level of degradation typical of masonry structures.

Furthermore, these structures have been designed and built in periods with no regulations, specific methodologies and calculation tools, favouring a design approach based more on the intuition and experience (e.g. geometrical rules).
The design approaches, which guarantee stability and performance for the buildings, less frequently were applied to the ordinary buildings.
In fact, the structural analysis applied to masonry structures is relatively recent. However, the use of numerical and/or analytical models is not simple, given the fragile architectural and structural context.
The issue is emphasized when the masonry buildings fall into the category of heritage buildings (like as monumental or religious buildings).
In these cases, the structural modelling can be extremely complex. Reliable results can be very difficult to obtain. In fact, the strong non-homogeneity of parameters makes it difficult to generalize the results to other case studies.
This is a critical issue, especially for the ordinary buildings, often designed by using geometrical rules without a suitable structural analysis.

1.2. Masonry buildings: a troubled history

The brick is the oldest manufactured product of the civilization. The first bricks were used in construction of buildings more than 6000 years ago.
The first masonry constructions included low walls made of stones or mud. Where stone was unavailable, masonry was made of local clays and silts.
The first constructions were made of rubble stone using overlap between the several blocks without a specific binder as shown in figure 1.2.

Figure 1.2: *Masonry shed made of rubble stones without binder, Montalbano Elicona, Sicily (Italy).*

Given the lack of mortar, the static capacity depends on geometrical factors. In particular, block sizes and contact surfaces of stones contribute to improve the structural performance *[Milosevic et al. 2015, Mueller et al. 2015, Lombillo et al. 2013 & Tran et al. 2014]*.

The stone was not the only material used for the masonry construction. At the same time, also adobe was used for civil constructions. Generally, these structures were located in the poor areas, where the high cost of construction materials has promoted dissemination of local materials like as mud or clay (figure 1.3).

Figure 1.3: *Example of Adobe masonry, Samassi, Sardinia (Italy).*

However, they are structures typically founded in archaeological or historical areas *[Caporale et al. 2015 & Illampas et al. 2014]*. When the buildings showed the first damages due to seismic events, many builders realized the importance of regular masonry units in order to increase bond between contact surfaces *[Caporale et al. 2014]*.

This was the origin of squared blocks ensuring a perfect contact between masonry elements.

At the same time, the civilizations of Central America, South America and Asia, have developed the technique of the cut stone. The artisans learned to manufacture the stones increasing the accuracy.

The next big step for brick manufacturing occurred in about 4000 B.C.. Starting from this period the builders begun to use brick elements with regular shapes (normalized shape of masonry units).

In order to increase the bond between masonry units, the soil represents the first material used in mortar joints to improve the behaviour of masonry. However, the use of new other materials with higher performance has been supported by the low performance of local materials.

The use of different materials depends on the regional resources. Many materials were used to build the mortar joints.

In the Mesopotamian area, the poor materials were replaced by new local materials. In particular, starting from the 19^{th} century, given the several oilfields, the mortar joints were made of a material based on bitumen.

Some discoveries both in Egypt and Greece showed that gypsum mortars were used starting from third millennium B.C.. These materials are characterized by an extremely fast maturation and showed good resistance to humidity *[Banfill et al. 2016]*.

The Roman Civilization had integrated these construction techniques into their own. During the Roman period, in the Southern Italy, especially in the Campania Region, many limestone caves originated the development of lime-based mortar *[Leone et al. 2016]*. The Pompeii archaeological site (figure 1.4) is a valid proof of these construction techniques.

Figure 1.4: *Pompeii archaeological site, Pompeii, Italy.*

Over time, through the art of turning limestone into lime, the mud was progressively replaced by lime-based mortar.

The lime-based mortars showed cracking due to a strong shrinkage. Some new mixtures using additional natural additives were developed to remedy at the shrinkage effects. In particular, slaked lime and inert sands additives guaranteed a reduction of shrinkage *[Fang et al. 2014]*.

The Romans, already from 3th century B.C., used the ash inert additive, the "pozzolana" *[Falchi et al. 2015]*. This natural additive improves the compatibility properties with the natural stones *[Falchi et al. 2013]*. Furthermore, the high performance of the lime-based mortar additivated with pozzolana guaranteed good performance at least for gravity condition. Then, new construction systems and manufacturing techniques were simultaneously proposed.

When control of Western Civilization passed to Romans, they made the first large-scale use of masonry arches and roof vaults in their basilicas, baths, palaces and aqueducts.

The Roman Heritage is the testimony of a design approach based on a progressive evolution in material and construction techniques.

Then, with the Islamic Civilization, the vaulted masonries were brought to a higher architectural and design level. The Islamic builders have built magnificent palaces, markets and mosques made of brick and often incorporated glazed clay tiles (figure 1.5).

Figure 1.5: *Mosque of Nasir Al-Mulk, also named Rosa Mosque, Shiraz (Iran).*

Instead, in the European areas, the goal focused on fortresses and cathedrals of stone, culminating in the pointed vaults and flying buttresses of the great Gothic churches (figure 1.6.).

Figure 1.6: *Cathedral of Orvieto, Orvieto (Italy).*

Where the money resources did not allow structural restoration of architectural heritage, the existing techniques were improved with the few available resources.

In particular, without natural stones in some continents, the manufacture was supported by the artificial blocks. These first elements were made of poor materials (clay, mud, terrain, etc.) mixed with several additives.

The first structures made of mud/clay were improved by using artificial blocks. The masonry units were made of materials based on a mixture of clay (adobe masonry).

In order to reduce the cracking, the adobe was mixed with natural fibres (e.g. panama). These additive fibres represent the first reinforced technique used in masonry *[Andrejkovičová et al. 2015 & Parisi et al. 2015]*.

Additionally, other additives were considered to improve the behaviour of artificial blocks. In particular, inert sands is a suitable additive to improve the performance and durability of the mixture.

Over time, these building techniques have been changed by a progressive refinement, e.g. in poor areas, the "pisè technique" (figure 1.7).

Figure 1.7: *Qasba 17th, Skpura's Oasis, Morocco.*

This material is a mixture made of clay and natural stone having small sizes *[Rovero et al. 2013]*. In some cases, natural mixtures were added to limit both the cracking and the weight.

The structure was built from modular elements. For each element, shuttering systems made of wooden panels were used. It represents the ancestor of the modern reinforced concrete. The shuttering panels have been designed to allow the construction of elements with any shape. However, the materials used are very cheap compared to the structures made of natural stone. In fact, the "pisè" technique was relegated to poorly buildings. The dissemination was stopped by the low performance of materials, especially in areas at high humidity and/or very rainy *[Sayin et al. 2013 & Quagliarini et al. 2015]*.

The effect of thermal radiations from fire on mud brick walls showed the advantages of the fired brick *[Černý et al. 2015]*, leading to brick kilns birth. In fact, the thermal irradiations provide a significant reduction of vapour permeability. Furthermore, the firing process causes a chemical bond between the clay particles, improving both the durability and the mechanical properties.

Along with the normalized bricks, the fired brick represents a new important step. With the last improving technique, it starts a revolution of the artificial manufacturing of masonry.

Because of the high cost of artificial bricks, dissemination occurred only in some continents. The clay brick wide spreading in the world is the result of development of the modern industries (figure 1.8).

The Industrial Revolution, between the last decades of the 18^{th} century and the first of the 19^{th} century characterizes the development of the building techniques. Following the industrial era, both the building technique and the design approaches suffered a strong change.

In particular, the buildings were not modelled as elements fully decoupled but as several elements mutually connected.

It was discovered that several components can interact if subjected to a seismic action.

Figure 1.8: *University of London, building made of solid clay bricks, England.*

During this period, sophisticated mathematical approaches were applied for the first time to the analysis of curved masonry elements (like as arches and vaults).

Portland cement mortar came into widespread use, enabling the construction of masonry buildings of greater strength and durability.

Through the centuries, the methods for manufacturing brick evolved continuously.

As brick manufacturing becomes highly elaborate, the use of design criteria became more diffuse.

Then, the evolution of design approaches has led to concrete block. The manufacturing of concrete blocks evolved over time. This evolution was prompted by the development of cavity walls. The cavity walls consisted of two separate brick or stone panels with about an inch of air space between them. The cavity masonry was developed to reduce the problems with water penetration.

Starting from this construction technique, several additional expedients have been applied. In 1850 a special block with air cells was introduced. Over the years, these elements have been modified until the modern industry developed standardized artificial elements, still in use.

Introducing the new systems of construction as: reinforced concrete (r.c.), laminated timber, steel, etc., the masonry buildings began to be replaced. Especially in the late 19th century, the masonry began to lose its primacy among the materials of construction. The very tall buildings of the central cities required steel or reinforced concrete frames which replace the thick masonry walls that limited the heights.

The reinforced concrete buildings began to replace brick and stone masonries both for the foundation and elevation. The heavy masonry vaults were replaced by lighter floor and roof structures made of steel and concrete.

In the 19th century the invention of the hollow brick, made of concrete, revitalizes masonry. In fact, over the 21th century, especially after the seismic earthquakes, an increasing interest for the masonry material has been shown.

After more than 6000 years, masonry is still used today. Therefore, the masonry constructions are an important part of the History Civilization that must be safeguarded.

1.3. Seismic behaviour of masonry buildings: in-plane and out-of-plane response

The masonry is a composite material where the mechanical properties are related not only to those of the components (stone, adobe, solid clay bricks, etc.) and mortar (mud, lime, hydraulic lime, etc.), but also to the sizes and shape of the constituents, the interlocking in the external leaves and the transversal connection through vertical and horizontal elements *[Asteris at al. 2014]*.

These aspects contribute to characterize the structural response of masonry buildings, with new techniques, construction and design approaches *[Serhal et al. 2016 & Landi et al. 2015]*.

Masonry constructions are generally brittle in nature and one of the most vulnerable structures under earthquakes. The inertial forces induced by seismic action may cause severe in-plane or out-of-plane effects *[Noor-E-Khuda et al. 2016a, Furtado et al. 2016, Schwarz et al. 2015, Bolhassani et al. 2016, Bruggi et al. 2015, Basili et al. 2016 & Giresini et al. 2016]*.
A masonry panel, if pushed horizontally in a direction perpendicular to its plane (out-of-plane) shows a lower capacity (figure 1.9 a). The same wall, if pushed along its length (in-plane) may show much greater capacity (figure 1.9 b).

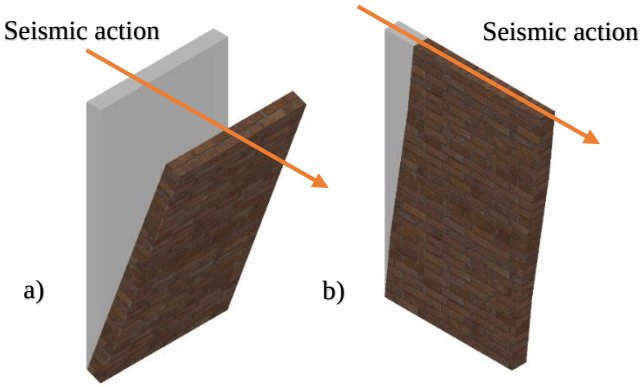

Figure 1.9: *a) Out-of-plane behaviour, b) in-plane behaviour of masonry wall.*

The seismic capacity of masonry buildings can be achieved when a local or global mechanism occurred *[Mendes et al. 2014]*.
The out-of-plane behaviour is promoted by lack of structural details (metallic ties, concrete ribs, etc.) and the seismic capacity depends on the local mechanism *[Akcay et al. 2016]*. This is a typical behaviour of poor buildings (ordinary buildings).
In this case, the seismic capacity is unaffected by the mechanical properties of materials *[Portioli 2016 & Dipasquale 2016]*. In fact, the load capacity depends on equilibrium conditions *[Walsh et al. 2015 & Furtado et al. 2015]*. Only for specific local mechanisms, the mechanical properties provide a non-negligible impact *[Milani et al. 2015a & Preciado 2015]*.

Generally, some masonry structures built on modelling base and capacity design criteria, showed a global behaviour *[Valente et al. 2016, Milani et al. 2015b & Akhaveissy et al. 2013]*. A global response depends on in-plane behaviour of masonry walls improving the seismic performance. The lateral load capacity of masonry structures is mainly due to in-plane shear strength of masonry elements *[Gattesco et al. 2015, Minaie et al 2014 & Mazzotti et al. 2014]*. In this case, seismic capacity of a masonry building is very sensitive to the mechanical properties of its constituents as well as masonry units and mortar *[Serhal et al. 2016]*.

1.3.1. In-plane behaviour assessment

When some structural details are incorporated in a building, the seismic capacity is not regulated by local mechanisms *[Darbhanzi et al. 2013, Foraboschi et al. 2013 & Ural et al. 2015]*. For this reason, the seismic assessment can be performed by means of a linear or non-linear global analysis, (with a static or dynamic approach).

The bending and shear forces, due to seismic action, cause vertical/horizontal and diagonal cracks *[Tomazevic et al. 2000]*, respectively. The first damage is due to flexural behaviour *[Esmaeeli et al 2013 & Almeida et al. 2015]*. While the second induces the typical shear damage.

In-plane damages alone, often cannot be sufficient to lead to structure collapse. Retrofit interventions performed on existing structures that lead to in–plane mechanisms improve the seismic capacity.

A global damage is due to strong connection among the masonry walls. The presence of rigid floors coupled to reinforced concrete ribs is able to transfer horizontal forces from floors to parallel walls. Therefore, a “box” behaviour of buildings under seismic actions is expected (figure 1.10).

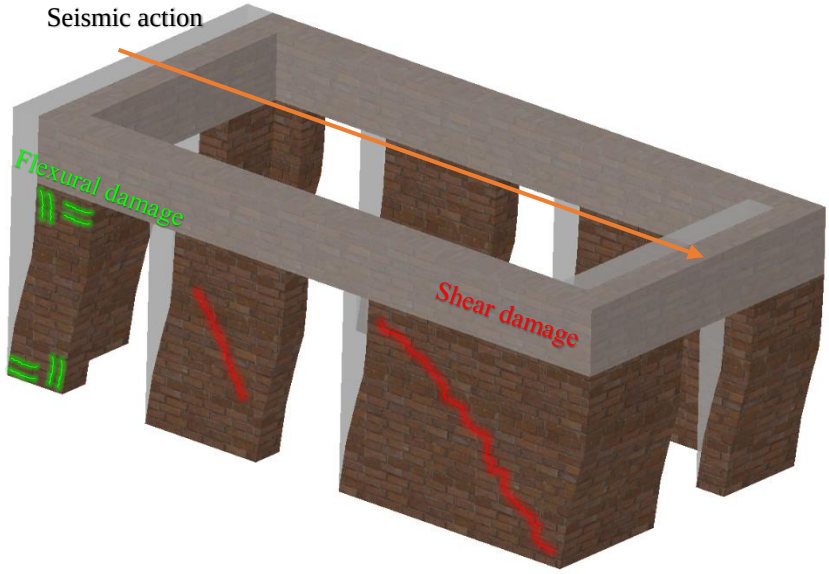

Figure 1.10: *Typical damage occurred due to in-plane behaviour of masonry walls.*

Unfortunately, the layout of ordinary buildings is not consistent with this background. Many of them show local mechanisms, given discontinues, change in time, lack of maintenance and other details, (figure 1.11).

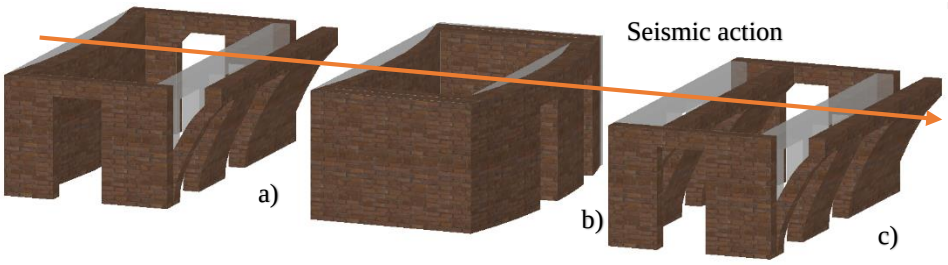

Figure 1.11: *Typical behaviour of masonry buildings: a) building with walls not tied together; b) building with deformable floors and tied walls and c) building with rigid floors and walls not tied together.*

Observation of seismic damages to masonry structure showed that masonry piers subjected to in-plane loading may have several types of behaviour

[Calderini et al. 2009] and different failure modes are associated: flexural behaviour and shear behaviour.

The flexural behaviour may involve two different mechanisms of failure. When the vertical load is extremely lower than compressive strength, a horizontal load increase produces tensile flexural cracking at the corners (figure 1.12 a).

The pier begins to behave as a nearly rigid body, rotating around toe (rocking mechanism *[Magenes et al. 1992]*).

The pier is characterized by a widespread damage pattern when no significant flexural cracking occurs *[Magenes et al. 1997]*. Then, a damage with sub-vertical cracks oriented toward the more compressed corners (crushing failure). In many cases, the ultimate condition is achieved by failure at the compressed corners (figure 1.12 a)).

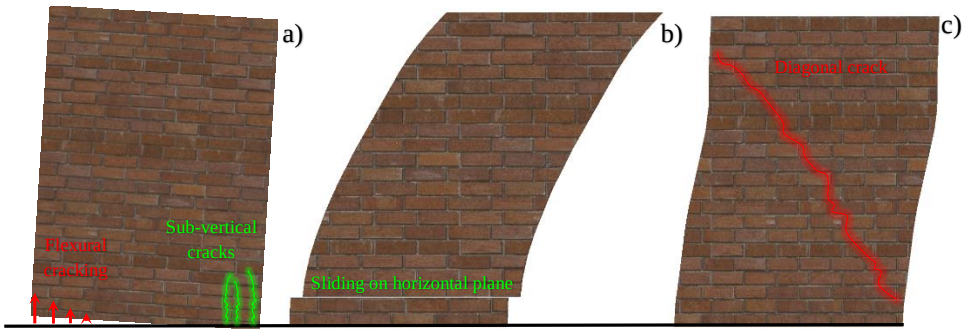

Figure 1.12: *Typical behaviour of masonry pier: a) rocking mechanism, b) sliding failure and c) diagonal cracking.*

A generic masonry wall under seismic action can show a shear behaviour. In particular, it produce two different failure modes. When the sliding shear failure occurs, the development of flexural cracking at the tense corners reduces the capacity of the section. The failure mode is attained with sliding on a horizontal joint plane. This plane of failure is generally located at one of the ends of the pier (figure 1.12 b).

Furthermore, if failure mode is obtained from the formation of a diagonal crack, it generally starts from the centre and then propagates towards the corners of the pier, (figure 1.12 c).

It is interesting to note that the crack may have occurred through mortar joints or also masonry units. The probability of occurrence of first or second propagation mode depends on the influence of the mortar-brick cohesion in the joints, (figure 1.13).

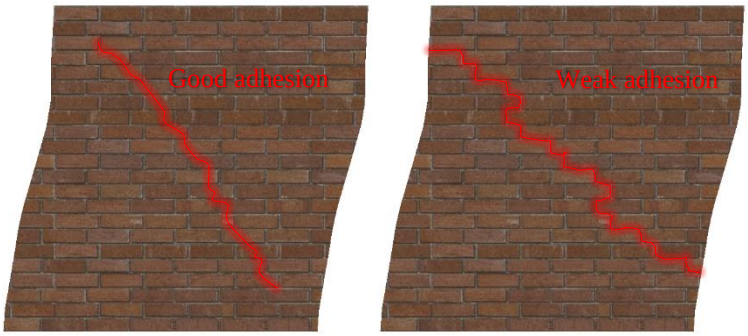

Figure 1.13: *Typical shear behaviour of masonry pier: Influence of the mortar-brick adhesion in the joints.*

The probability of occurrence of different failure modes depends on several geometrical and structural parameters:

- Geometry of the structural elements: block aspect ratio and characteristics of cross section;
- Load pattern: vertical and horizontal load;
- Boundary conditions;
- Mechanical characteristic of masonry constituents regarding to: mortar, blocks and interface.

In the past, several pseudo-static and dynamic tests have been carried out in order to analyse the effect of previous parameters on failure modes of masonry walls.

Rocking mechanism occurs mainly in slender piers and with low value of vertical loads, while the shear failure occurs in very thick piers.

For moderately slender piers, diagonal cracking tends to prevail over rocking and bed joint sliding at increasing vertical loads *[Lourenço et al. 2005]*.
The diagonal cracking propagates through masonry units more than through mortar joints for increasing vertical loads. Similar effects can be shown at increasing ratios between mortar and block strengths *[Bosiljkov et al. 2003]*.
The failure mode, changing from diagonal cracking through mortar joints to rocking, yields to an increase interlocking of blocks.
The same effects may induce a transition from diagonal cracking through mortar to cracking through masonry units or to bed joints sliding.
The crashing failure usually occurs for high levels of vertical loads *[Vasconcelos et al. 2006]*. However, several seismic assessments and tests showed that normal stresses are usually much lower than the compressive strength. For this reason, the crashing failure has an extremely low probability.

1.3.2. Out-of-plane behaviour assessment

Many approaches were developed to assess the seismic capacity by local mechanism *[D'Ayala et al. 2003]*.
Since the 17th in Europe, empirical approaches, on the estimation of vulnerability indexes, have been proposed *[Benedetti et al. 1984]*. These methodologies are mainly devoted to historical masonry buildings. Over time, they were improved to extend at different typologies of buildings *[Lagomarsino 1998a]*.
The studies based on in-situ surveys after seismic events allowed to create charts of the typical damages occurring in structural typologies. It has led a consequent systematization of the mechanical models able to describe their behaviour by means of kinematic models *[Lagomarsino 1998b]*.
Kinematic models provide a coefficient $\lambda_K=a/g$ calculated through the a ground acceleration over the g gravity acceleration ratio *[Bernardini et al*

1990]. It represents the seismic masses multiplier characterizing the ultimate equilibrium conditions for the structural element.
In simplified assessment procedures, the mechanism connected to the lowest value of λ_K is the weakest one and, consequently, the most probable to occur. The in-plane mechanisms are usually characterized by λ_K coefficients higher than the out-of-plane ones.
The mechanisms are related to the loss of equilibrium of structural portions rather than to states of stress exceeding the materials ultimate capacity.
The limit analysis approach depends on few geometrical and mechanical properties. Therefore, it does not require an extremely accurate survey and time-consuming computation *[Lagomarsino et al. 2004a]*.
Once the critical structural configuration is defined, the subsequent step is the identification of the most probable collapse mechanisms of each macro-element *[Lagomarsino et al. 2004b]*.
Several works on seismic vulnerability assessment of masonry buildings through limit analysis procedures have been proposed. The research was restricted to the estimation of the seismic activation multiplier, even if evaluated for complex mechanisms (typical of agglomerates of buildings).
This approach of limit analysis applied to existing masonry buildings in seismic areas is now provided by the recent Italian seismic code. These models take into account the high vulnerability of existing masonry buildings not satisfying assumptions commonly more suitable for new earthquake-resistant buildings.
In this field, another important document is represented by the Guidelines published by the Italian Ministry of Cultural Heritage for the evaluation and mitigation of seismic risk of the architectural heritage.
Nevertheless, the out-of-plane behaviour assessment of masonry walls is one of the most debated topics in the scientific community. This failure mode may often limit the seismic capacity of existing masonry buildings. In ordinary buildings there aren't specific measures and a global analysis is not always feasible, this means that because of the natural discontinuities of

ordinary masonry and interactions with the neighbouring buildings, the local mechanisms assessment becomes a critical aspect.
The external walls of buildings can be typically subjected to out-of-plane mechanisms (figure 1.14).

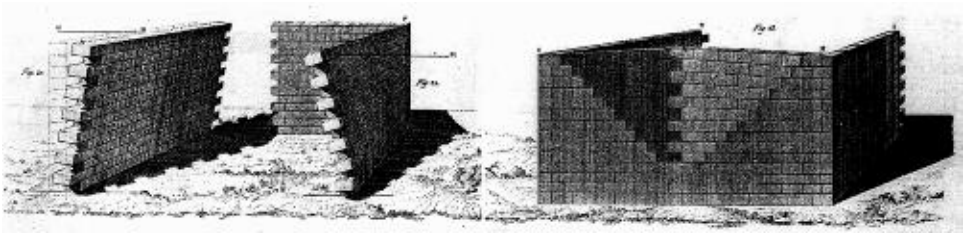

Figure 1.14: *Typical collapse mechanism of masonry walls by out-of-plane behaviour [Rondelet et al. 1834]*

Direct observation of damages detected after the last earthquakes, together with the scientific literature on the surveys of stone masonry buildings damage due to seismic events, showed that often the most recurrent failure mode is the overturning of walls.
However, this failure mode involves portions of walls and infrequently involves the full wall.
The way in which the local mechanism will activate depends on several structural details: quality and mechanical properties of masonry, connections between several structural elements, internal load-bearing, tie devices, type of floors and roofs, etc..
For unreinforced masonry, it is assumed that the only way to restrain the overturning mechanism carried out by other walls is regulated by the friction properties on the contact surfaces. These characteristics will give rise to different failure modes (figure 1.15).

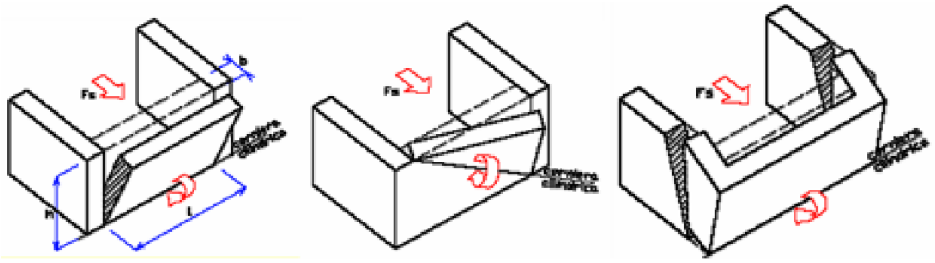

Figure 1.15: *Influence of the restraints effectiveness on overturning mechanisms [Borri et al. 2004]*

If the seismic capacity of buildings has been improved by means of additional devices like as ties or ring beams, the simple overturning is prevented. In this way, the failure mechanism is governed by the arch effect (figure 1.16).

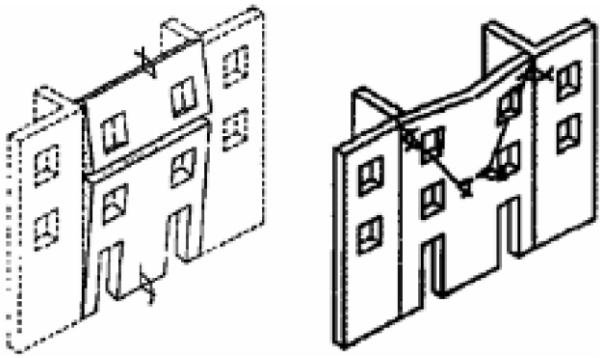

Figure 1.16: *Local mechanism based on the arch effect [D'Ayala et al. 2003].*

The framework becomes extremely critical for very complex buildings. In these cases the local behaviour can be analysed for a discrete number of structural portions.

For example, in agglomerates of buildings the local behaviour assessment can be particularly complicated (figure 1.17).

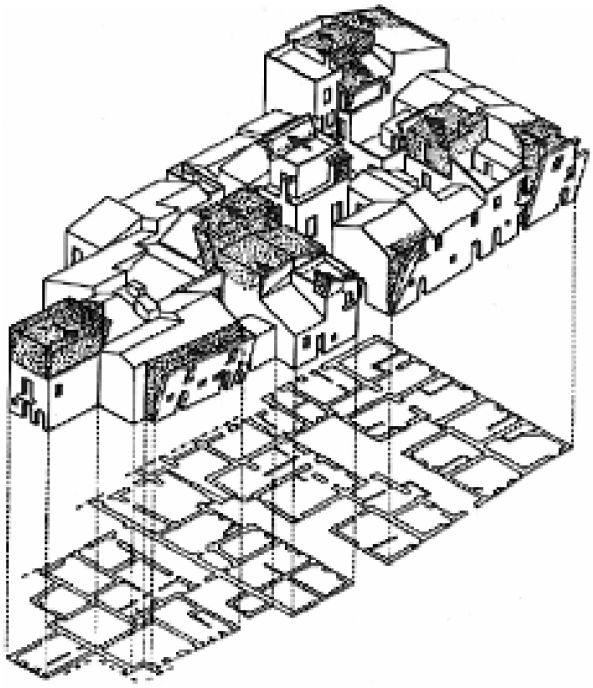

Figure 1.17: *Agglomerate of buildings typical of historical centres [Giuffrè, 1993].*

When the building becomes very complex, a first step is to recognize structural units (structural portions). Then, the seismic capacity can be estimated using a macro-element approach.

Therefore, a generic structural unit is made of several macro-elements (walls, floors and roofs).

A critical issue is that the units can be structurally recognizable with an autonomous behaviour compared to the entire building. In fact, only some interactions can be modelled to avoid a complex model.

In particular, the mutual bond between macro-elements can be modelled by potential damage pattern, contours of poor connection and statically equivalent forces.

The damage could involve different structural shapes which depend on the characteristics of the walls (masonry properties, internal constraints, etc.).

The visual surveys performed after last earthquakes showed that the failure modes are very different between different building typologies.
For heritage buildings, as churches, the seismic behaviour led to recurrent local damages of several architectonic components (i.e. nave, triumphal arch, apse, etc.) as shown in figure 1.18. These collapse mechanisms occur almost independently.

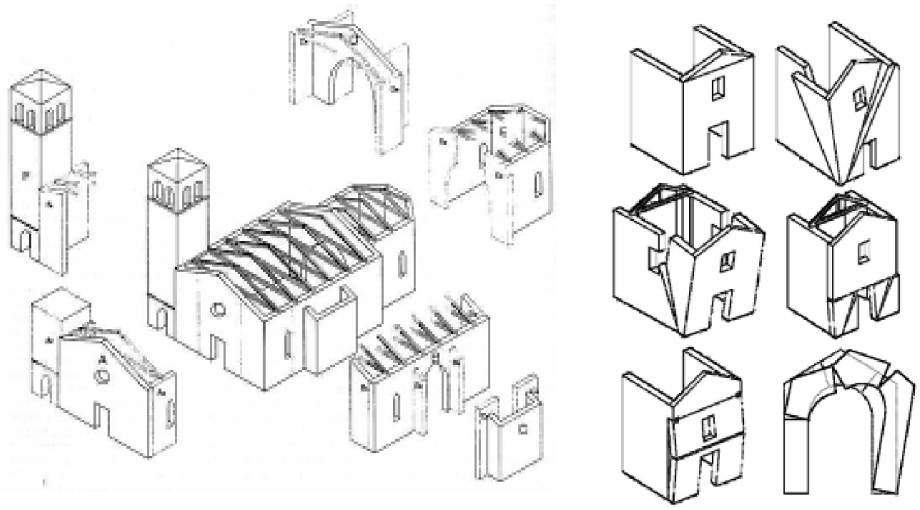

Figure 1.18: *Typical damage mechanisms of religious buildings [Doglioni et al. 1994 & Lagomarsino et al. 2004a].*

1.3.3. The ordinary and heritage buildings

An extensive typological classification is a hard task because the current buildings stock refers to a wide variety of constructions.
Into each urban area two macro-classes of buildings can be identified: ordinary buildings and heritage buildings.
The two typologies are characterized by both different masonries (quality, mechanical properties, etc.) and structural systems (regularity, connection, etc.). These characteristics change through historical periods and geographical areas.

Starting from the first constructions, without specific guidelines, the design of buildings was performed with empirical approaches.
Many of existing masonry structures have been designed exclusively by means of geometrical rules. These approaches were based on past experiences rather than on accurate structural analyses.
Only, for particular buildings (heritage buildings), some structural details were implemented during the construction phases. Therefore, many of the existing buildings, typically identified as ordinary buildings, are characterized by a low seismic performance.
Even so, the recent earthquakes (figure 1.19) showed the results of these design approaches.

Figure 1.19: *L'Aquila (Italy) and Emilia Romagna (Italy), damages after 2009 and 2012 Earthquake respectively.*

Many ordinary buildings are usually vulnerable because specific details were not adopted to prevent seismic damage. In particular, without specific details as: steel ties, buttresses, connection of floors to masonry walls, etc., the seismic capacity is limited by local mechanisms (out-of-plane behaviour) as shown figure 1.20.

Figure 1.20: *Local mechanism (out-of-plane behaviour) of an ordinary building, Emilia Romagna (Italy), damages after 2012 Earthquake.*

After the first damage observation, specific measures were adopted in order to withstand the earthquake. In addition to modify the classical construction systems, the structures began to be analysed on the basis of modelling and capacity design criteria.

The specific details mainly used in heritage buildings improve the dynamic behaviour. For these structures, the seismic capacity is regulated by global mechanism (in-plane behaviour). In fact, structural details promote a global response of the buildings while preventing local mechanisms (figure 1.21).

Figure 1.21: *Torrione degli Spagnoli, Emilia Romagna (Italy), damages after 2012 Earthquake.*

In fact, as the recent earthquakes show, the use of structural details prevents the activation of simple mechanisms, characterized by a low seismic capacity (i.e. global behaviour shows a higher activation multiplier).
Previous brief description is not intended to be a full picture about the history of masonry but provides the complex background that each professional engineering or architect must face.
A typological classification of buildings can be an useful approach in order to assess the main parameters which characterize the seismic response of masonry buildings. In the next section, a preliminary study based on a vulnerability assessment at regional level is synthetically discussed.

1.4. The vulnerability assessment at regional scale: an useful tool to estimate the main vulnerabilities.

A detailed study of each of these existing buildings is very complex so it can be interesting to analyse the vulnerability by means of simplified approaches.
The safeguard of existing buildings, with particular reference to prevention strategies and mitigation of seismic risk, is currently an issue of great interest for existing urban stock (especially for heritage masonry buildings).
For this goal, refined numerical models cannot be adopted due to the strong non-homogenous characteristics especially for existing buildings stock.
In fact, the analysis at regional level cannot be performed in order to assess the seismic capacity of a single building but it can provide an estimate of main parameters that characterized the seismic behaviour.
For this reason, a vulnerability assessment has been performed by means of study at regional level. The goal is to estimate the main parameters which characterize the vulnerability of existing masonry buildings.
Furthermore, it is interesting to identify the main causes of vulnerability into historical urban areas.
This first study, synthetically discussed below, is a preparatory work.

In particular, the results showed that the thrusting elements (as arches and vaults) can increase the vulnerability for existing masonry buildings.
The assessment of the actual susceptibility of existing masonry structures to be damaged by seismic actions (vulnerability) requires complex procedures. These buildings are, indeed characterized by a strong non-homogeneity of construction techniques and by a level of degradation typical of masonry structures.
Furthermore, these structures have been designed and built in periods characterized by no regulations, specific methodologies and calculation tools, favouring a design approach based more on the intuition and experience. For these reasons, masonry buildings are often characterized by a strong vulnerability.
This study is a first step towards the development of a seismic vulnerability evaluation procedure for the masonry buildings on large scale.
For this purpose fragility curves have been elaborated, not related to single structural unit, but to classes of buildings, characterized by similar behaviour under seismic actions.
In addition, to perform a vulnerability analysis at regional level *[Valluzzi et al. 2004]*, the objective is not to identify the behaviour of individual structures, but to define an "average" behaviour in some homogeneous building classes. Therefore, to this aim, the analyses are typically conducted on entire urban areas, or on a multitude of buildings *[Lagomarsino et al. 2004c]*.
The vulnerability assessment at the regional level, starting from a not detailed, quick, in situ data collection, should be able to return a reliable assessment of the seismic vulnerability degree, without the use of refined and complex models.
This allows an initial and quick classification of the structural types depending on some principal parameters; the identification of conditions of highest seismic risk and to provide preliminary support in post event operations.

1.4.1. Case study

The masonry buildings considered to create a database of structural typologies, for the seismic vulnerability assessment at a large scale level, are located in the historical centre of Benevento (figure 1.22).

Figure 1.22: *Historical centre of Benevento.*

With reference to masonry, three masonry classes (Mu_1=rubble stones masonry, Mu_2=tuff masonry and Mu_3=solid brick masonry) have been detected in the examined stock of building based on a visual inspection.
The main physical and mechanical properties of such masonry classes are reported in table 1.1.

Table 1.1: *Mechanical properties for masonry classes.*

Masonry classes	f_m [MPa]	τ_0 [MPa]	E [MPa]	G [MPa]	W [kN/m^3]
Mu_1	1.0	0.02	870	290	19
Mu_2	1.4	0.03	1,080	360	16
Mu_3	2.4	0.06	1,500	500	18

The ordinary buildings (residential buildings without a particular artistic value) represent a significant portion of the urban area.

The building stock in Benevento can be attributed mainly to two different periods: mid-17th century and early-19th century.

The differences in construction are partially due to two important seismic events (1688 and 1702) that were the reason of a partial or total reconstruction of most buildings.

Nevertheless, frequent characteristics, both structural (materials and techniques) and geometrical can be individuated in the masonry buildings of the historical centre. Most of the buildings are made of rubble stone masonry, while a lower percentage of tuff stones or clay bricks.

The on-site surveys represented the starting point to gain knowledge of the examined building stock. The knowledge level and details should be consistent with a quick on site operation.

In these preliminary studies, specific survey forms have been developed which have been used to screen over 220 buildings.

In particular there are shown: compressive strength f_m, shear strength τ_0, elastic modulus E, shear modulus G and specific weight W. These values has been chosen according to the typological identifications provided by the current Italian code *[IBC 2009]* and adopting the minimum strength values and the average elastic modulus values of the suggested ranges, according to a reduced knowledge level.

With respect to the first assignment based on the visual inspection, presence of degraded or non-homogeneous mortar joints leads to declass the masonry.

Table 1.2 describes the assignment matrix of the masonry classes to different masonry types found in Benevento. Where it is not possible to identify the masonry type, the class with worst mechanical characteristics (i.e. Mu_1) was assumed.

Table 1.2: *Masonry class identification.*

Masonry Type	Good state of conservation	Degraded mortar	Inhomogeneous texture
Rubble stones	Mu_1	Mu_1	Mu_1
Rounded blocks or stones	Mu_2	Mu_1	Mu_1
Tuff stones	Mu_2	Mu_1	Mu_1
Squared blocks	Mu_3	Mu_2	Mu_2
Solid bricks	Mu_3	Mu_2	Mu_2
Hollow bricks	Mu_2	Mu_1	Mu_2
Clay bricks	Mu_2	Mu_1	Mu_1

Furthermore, three types of floor (wooden, metallic and concrete slabs) have been identified in addition to the vaults frequently present at the first floor of the buildings. The presence of steel ties and concrete ring beams has been also detected.

The average interstorey height, referring to all floors, varies in two ranges: 2.7m - 3.0m and 3.0m - 3.4m. A height of 3.4m was assumed when vaults were found at the first floor.

The dimensions of the openings, which directly affect slenderness of the masonry panels, are catalogued in terms of approximate average sizes: 0.8m×1.2m to 1.2m×1.4m for windows and 0.8m×2.0m to 1.2m×2.5m for doors.

1.4.2. Structural modelling

The vulnerability assessment has been performed on the base of a mechanical approach.

For this reason, several structural analyses were carried out. Furthermore, several mechanical prototype models have been developed in order to assess the effects of main geometrical and mechanical parameters on seismic capacity.

The choice of parameters to define typological structural classes was based on parametric analyses aimed to identify representative mechanical models. This goal was obtained by examining the structural behaviour through non-linear static analyses in terms of "capacity curve" (load-displacement curve) varying significant geometrical and mechanical parameters of the buildings. The results allowed to identify mechanically representative models of different typologies of the building stock. For this purpose the (96) chosen structural prototype models are simple and representative (Figure 1.23).

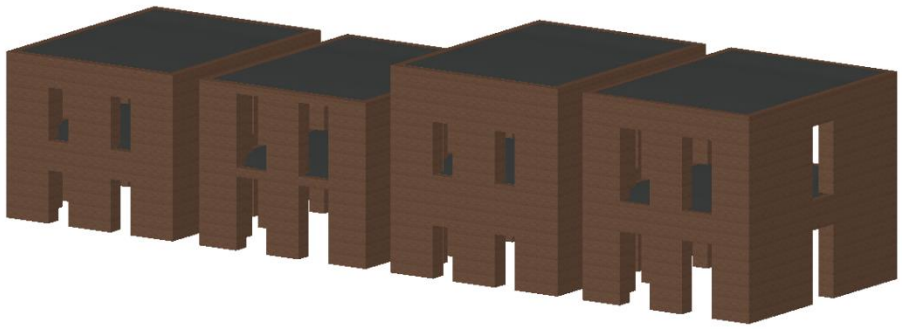

Figure 1.23: *Examples of the geometrical schemes of structural models.*

On these prototype models the effects on seismic capacity of several parameters were assessed. The figure 1.24 shows some of several variables used into prototype models. The simplified modelling allowed to identify the causes of vulnerability.

Figure 1.24: *Examples of parameters implemented into structural models, a) Steel ties, b) masonry barrel vaults, c) type of floor.*

The prototype models are the result of the essential simplifications for the development of the procedure and are described below.

1.4.2.1. Mechanical and geometrical characteristics

The three masonry classes indicated in table 1.1 have been used.
Regarding the geometry of the models, the plan is rectangular with average size 8.1m×6.1m; the masonry thickness varies depending on physical and mechanical properties and they have been designed based on static considerations (vertical load bearing capacity).
The distribution of the openings is intended to guarantee regularity of the walls in their plane.
The interstorey height is variable from 2.8 to 3.3 meters; in the case of vaults at the first floor, a higher height (4.0 m) has been considered. The number of floors ranges from 2 to 4.
The design of the floors was conducted according to vertical load capacity and deformability requirements (deflection limits).
For the design of the vaults, barrel vaults were considered having the minimum span.
The steel ties, when present, were positioned at all the levels and across all the walls.

1.4.2.2. Load direction and target node

Non-linear static analyses were carried out for each model in four main directions (±X and ±Y), neglecting the accidental eccentricity effect and considering a distribution of inertia forces proportional to the masses.
The control node has been chosen at the top level (figure 1.25).

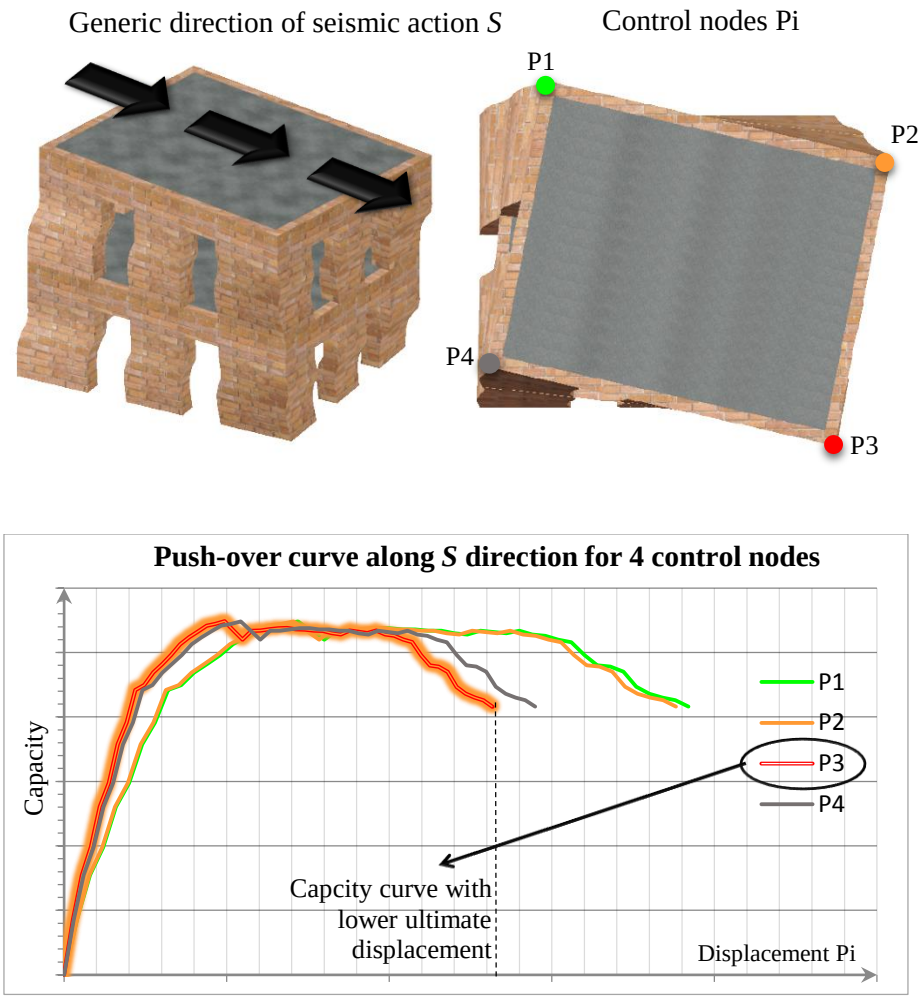

Figure 1.25: *Chosen of control node.*

The load direction corresponding to the push-over curve characterized by the least dissipation capacity was considered as representative of each prototype building (figure 1.26).

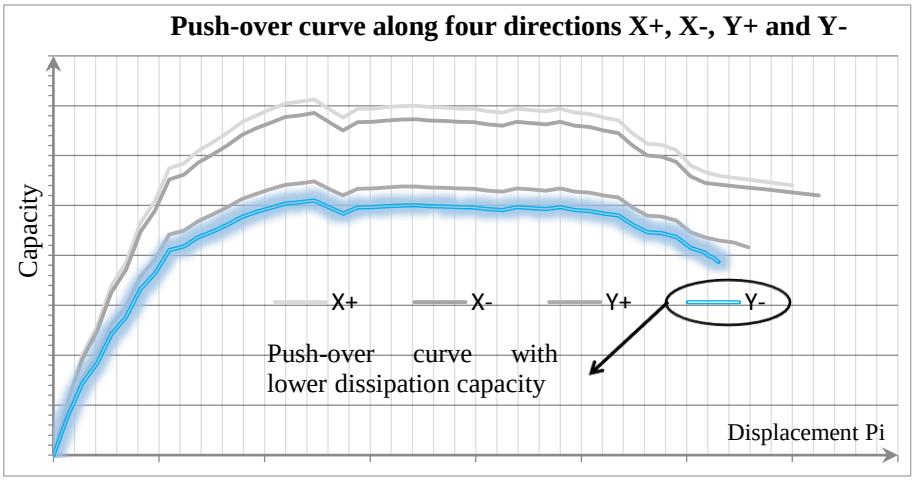

Figure 1.26: *Chosen of seismic direction.*

1.4.3. Capacity curves: analysis, comparison and classification

Based on the most conservative capacity curve for each model, different structural behaviours were compared. The structural responses were examined in terms of SDOF (equivalent simple oscillator) in the ADSR plane (ground acceleration-displacement).

All the 96 prototype models have been analysed according to this procedure in order to assign the structural classes.

The current tendency is to perform exclusively typological classifications as described by the European Macroseismic Scale (EMS98). This approach doesn't take into account the actual structural responses characterizing the typological behaviour and potentially could lead to unreliable damage assessments.

On the basis of the capacity curves reported in Figure 1.27, the prototypes were assigned to six structural classes as identified by different colours.

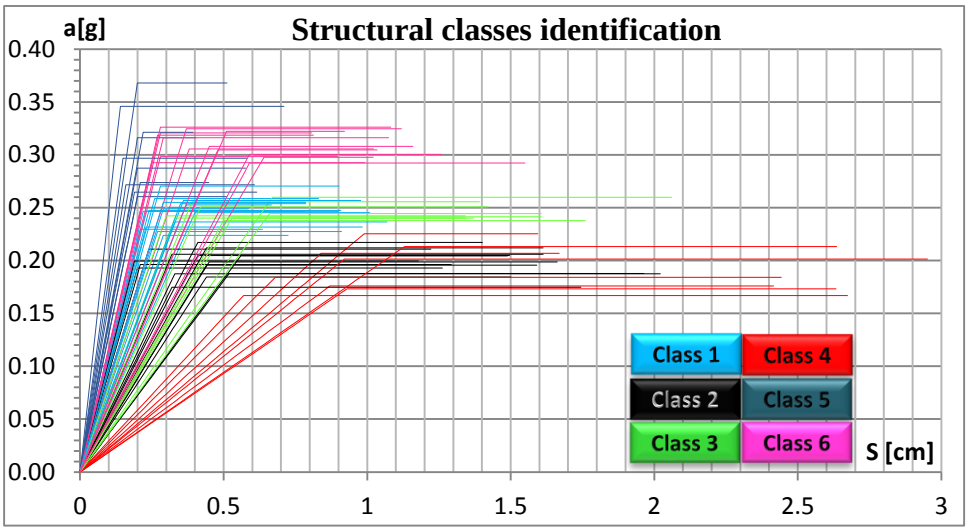

Figure 1.27: *Structural classes individuation: structural behaviour in term od SDOF in the ADSR plane.*

However, the classification was refined taking also into account the typological parameters. The definition of the structural classes was conducted on the basis of the following criteria and aims:

- to standardize the global structural behaviour of the class; to this aim each SDOF capacity curve was examined in terms of stiffness, strength threshold, yield displacement and ultimate displacement;
- the capacity curves were examined both with reference to the behaviour and typological properties;
- to achieve a significant number of structural classes to perform accurate assignations of the relieved buildings.

In table 1.3 the main parameters that identify each class are reported.

Table 1.3: Structural class identification.

Class	Description	Significant parameters
1	Medium-low strength threshold and low ductility	Mu_1, 2 floors, metal beams floors, stiff spandrel panels. Mu_2, 3 floors and concrete or metal beams floors, whit ties. Mu_3, 2 floors and vaults at the first level.
2	Low strength threshold and high ductility	Mu_1, 3 floors and stiff spandrel panels. Mu_3, 2/3 floors and vaults at the first level.
3	Medium strength threshold and high ductility	Mu_3, 3 floors and concrete or metal beams floors, whit vaults at the first level.
4	Partially rigid behaviour, low strength threshold and high ductility	Mu_1/Mu_2, 3 floors, metal beams floors, weak spandrel panels. Mu_3, 4 floors, metal beams floors, whit vaults at the first level.
5	Rigid behaviour, high strength threshold and low ductility	Mu_2/Mu_3, 2 floors, concrete or metal beams floors, whit ties.
6	Medium-low strength threshold and l medium-low ductility	Mu_3, 3/4 floors, concrete or metal beams floors, whit ties.

On the base of previous classification an identification of classes on the urban area has been performed. The figure 1.28, shows the several class (Class 1, Class 2, …, Class 6) assigned to the historical centre of Benevento.

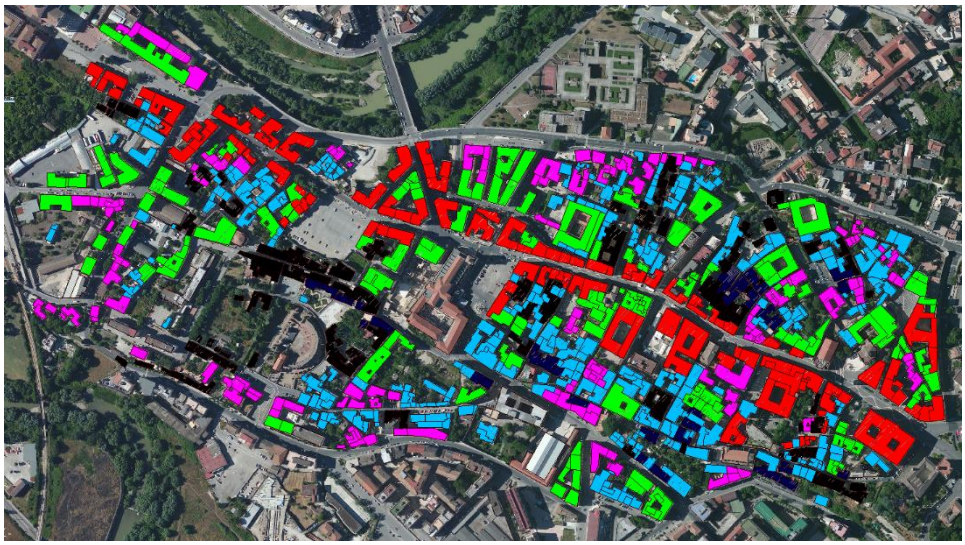

Figure 1.1: *Classes individuation for the historical centre of Benevento, Class 1(ciano), Class 2(black), Class 3(green), Class 4(red), Class 5(blue) and Class 6(magenta).*

1.4.4. Damage estimation: in-plane behaviour

Starting from the analyses of the capacity curves in terms of SDOF it is possible to identify the ranges of damage.

These ranges are dependent on the mechanical characteristics of each model. The relation between capacity and damage *[Calvi et al. 2004]* is processed directly on the bilinear curve through the identification of some displacement thresholds.

The typologies of damage taken into account are those covered by the European Macroseismic Scale EMS98. Then, the damage thresholds are evaluated as function of the yield, d_y, and ultimate, d_u, displacements (Figure 1.29).

A certain damage level is attained if the displacement demand exceeds the displacement threshold associated to that damage under a certain seismic event.

The distributions of damage found with this procedure are site-dependent, since the seismic event is, in general, site-dependent.

The calculation of the displacement demand is executed according to the N2 method *[Fajfar et al. 1996 & Fajfar 1999]*.

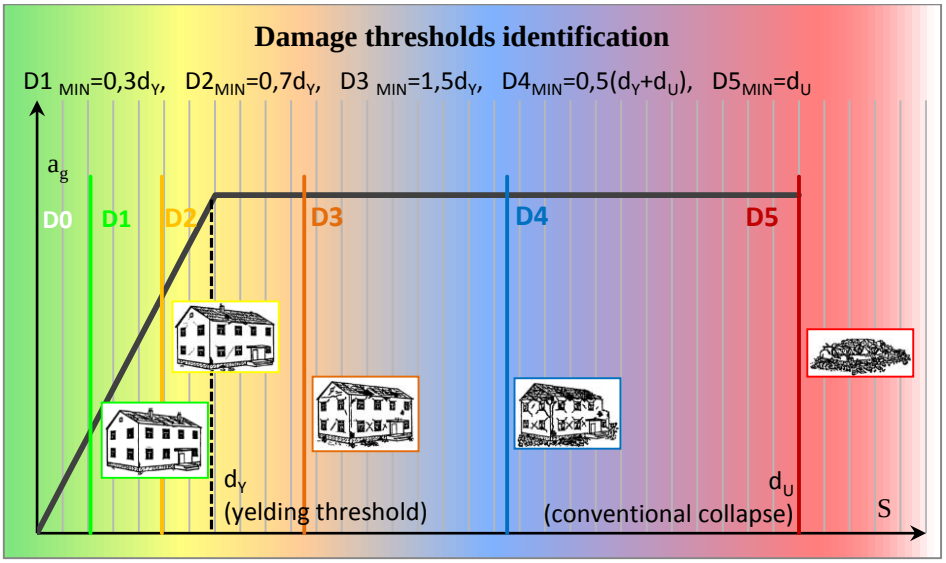

Figure 1.2: *Identification of the conventional damage thresholds.*

The distribution of a fixed damage level within each class for different seismic intensities is evaluated by computing how many buildings of that class attained the fixed damage level.

For each building a fixed damage level is attained when the capacity demand, evaluated for different seismic intensities, exceeds the displacement threshold (capacity) corresponding to that damage. The seismic intensities were expressed in terms of PGA assuming an unit increase of the return period Tr (1 year).

This procedure allows obtaining "fragility curves" that represent an useful tool to perform damage estimations within a certain class of homogeneous buildings.

It is worth to note that in the technical literature *[Polese et al. 2007]* the concept of 'fragility curve' has a probabilistic connotation and is often

associated to several meanings depending on aims and fields of application of such curves.

The fragility curves presented in this paper provide, for a fixed seismic event, individuated by the PGA value and the return period Tr, the percentage of buildings, p_k (s_{Tr} | s_{Dk}) that, within each class, have a damage level greater than or equal to an assigned damage D_k.

Thus, the curves are built for each class and for each damage level. The five damage levels individuated by EMS98 have been chosen. According to this approach the probability p_k (s_{Tr} | s_{Dk}) is given by:

$$p_k(s_{Tr}|s_{Dk}) = \frac{n(s_{Tr} \geq s_{Dk})}{n_j} \cdot 100 \qquad (1.1)$$

where $n(s_{Tr} \geq s_{Dk})$ represents the number of buildings with displacement demand, S_{Tr}, associated to that T_r, greater than the capacity displacement, S_{Dk}, associated to the D_k damage. The term n_j indicates the total number of prototype buildings of a structural class.

The results obtained through previous equation provide a discrete point of the fragility curve. The fragility curves can be regularized by means of the procedure discussed below.

In particular, starting from the conventional threshold as previously shown, the corresponding PGA_k value can be calculated. These values represent the acceleration thresholds calculated for each prototype model and for conventional damage D_k.

Given that a directly link between displacement and associated acceleration threshold cannot exist, the process is iterative. In fact, linking the displacement s_{Dk} to the acceleration threshold PGA_k the spectrum shape is altered.

Given the distribution of acceleration thresholds PGA_k, the fragility curves were obtained. In Figure 1.30 the fragility curves for the structural class 4 are illustrated for the five threshold damages of EMS98.

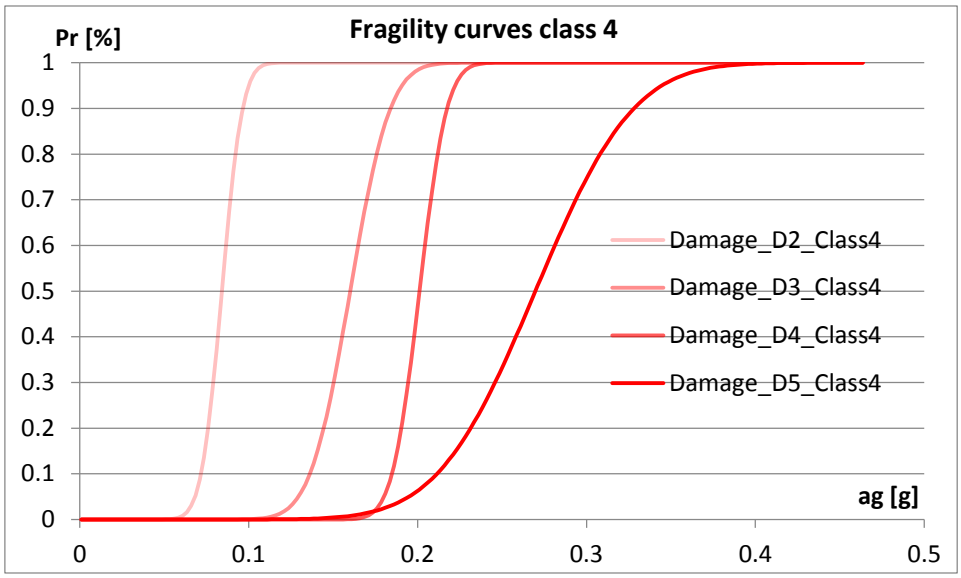

Figure 1.3: *Fragility curves for the structural class 4 for all damage thresholds.*

In Figure 1.31 and figure 1.32 the different fragility curves obtained for the damage threshold D3 and D5, respectively, for the six structural classes are plotted.

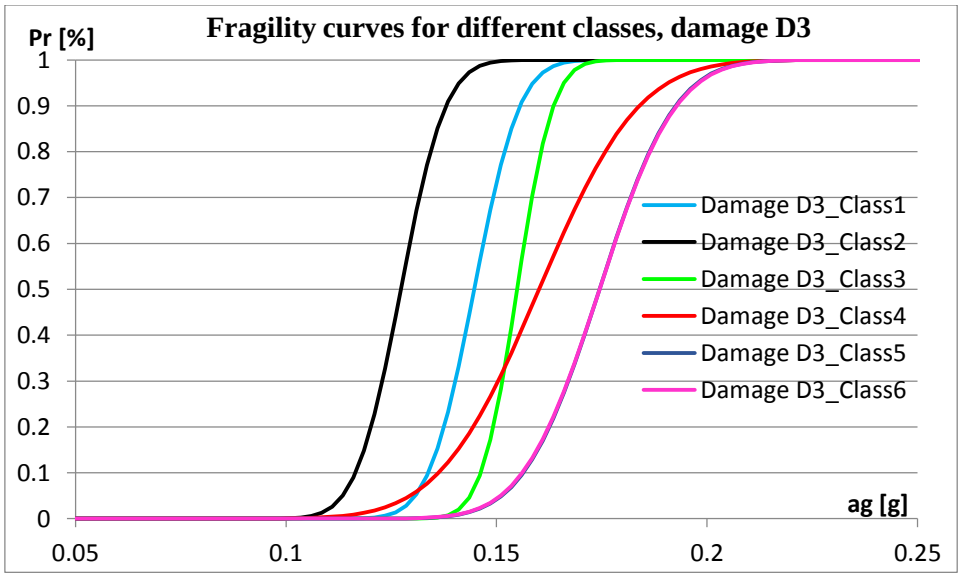

Figure 1.4: *Fragility curves comparison for all structural classes and D3 damage.*

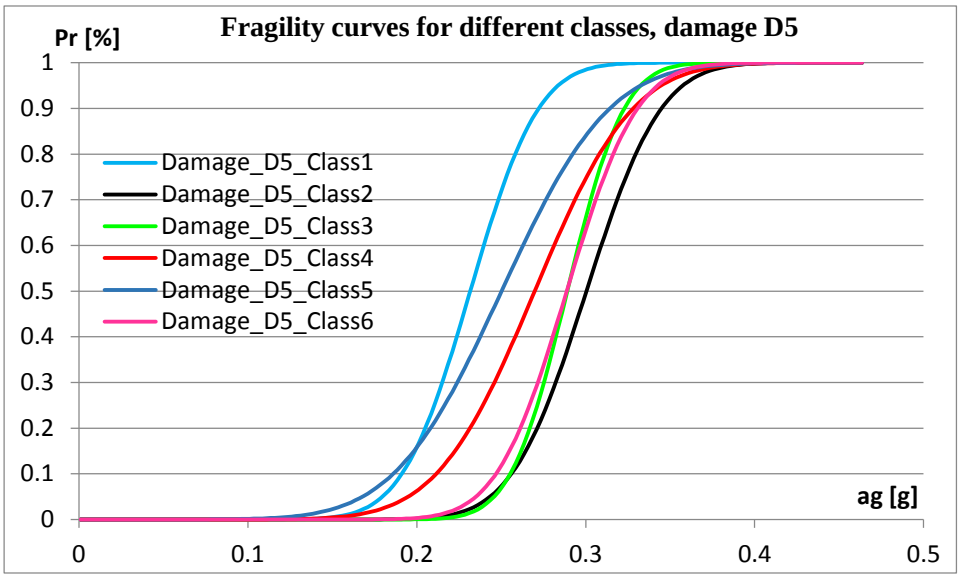

Figure 1.5: *Fragility curves comparison for all structural classes and D5 damage.*

1.4.5. Vulnerability maps for the case study: in-plane behaviour

The fragility curves obtained according to the procedure explained in the previous section were used as a tool to provide information on the spatial distribution of the different damages D_k in the historical centre of Benevento.

To this goal the relieved real buildings were assigned to the six typological classes defined according to the capacity curves of the 96 prototypes (figure 1.28).

Starting from figure 1.33 and figure 1.34, for demonstration purposes, the maps of distribution of damage D3 and D5 are plotted for the PGA values related to the return periods Tr=201 and 475 years, respectively.

Figure 1.6: *Vulnerability map for the historical centre of Benevento: D3, TR=201 years.*

Figure 1.7: *Vulnerability map for the historical centre of Benevento: D5, TR=475 years.*

Such damage levels were chosen in order to be significant for the fixed PGA values: it is, indeed, interesting to evaluate the distribution of a low-medium damage for seismic events corresponding to serviceability conditions, while for the higher PGA values (i.e. Tr=475) it is more significant evaluating the distribution of damage D_5.

In all cases the distribution of each damage was expressed in terms of percentage of buildings exceeding the fixed damage threshold, grouping into four percentage ranges: 0-25%, 25-50%, 50-75%, 75-100%. The coloured representation means that, referring for example to the buildings coloured in red, the 75-100% of these building is expected to attain the examined damage.

A more refined vulnerability map should take into account also the actual distribution of soil type in the examined area: in the presented maps, soil was assumed as type B, according to the large part of the historical centre of Benevento.

The maps show that for low intensity seismic events (Tr=201, figure 1.33) most of the relieved buildings did not attain the damage D_3, while as the seismic intensity grows, the percentage of buildings that exceeds higher damage thresholds (i.e. D_5) is lower (see figure 1.34).

1.4.5.1. Drawbacks of vulnerability analyses based on an in-plane behaviour

The methodology developed in this paper for evaluating the seismic vulnerability is not intended to analyse individual buildings, but is a valuable tool for large scale vulnerability assessments and to develop vulnerability maps aimed to identify areas of high seismic risk.

The reliability of the method is directly related to the representativeness of the prototype models and how the chosen geometrical and mechanical parameters influence the models behaviour.

The procedure developed has a general nature and can be easily implemented. The enrichment of the database is an interesting advancement step for the study and for the application of the method at a wider, even national, scale.

Continuous development of the database, constantly updated, could represent an essential support for seismic vulnerability analysis at national scale.
The automation of the methodology for the structural classification and the refinement of the procedure of assignment and classification, would improve those aspects, essential for the complete automation of the developed methodology.
However, the damage assessment has been performed by using a push-over analysis. The local behaviour of the structures cannot be take into account. For buildings where some structural details has been incorporated, the previous results provide some useful information about their vulnerability. For ordinary buildings, these results showed partially the effects of geometrical and mechanical parameters on the seismic response.
Therefore, mechanical-capacitive analyses that take into account also out-of-plane mechanisms are certainly valuable and they must be performed.
The implementation of the previous analysis with local mechanism is synthetically discussed below.

1.4.6. Vulnerability maps for the case study: out-of-plane behaviour

A vulnerability assessment on masonry buildings cannot preclude the possibility that a local behaviour occurs. In fact, often the local seismic capacity (out-of-plane behaviour) is lower than the global capacity (in-plane behaviour).
The failure mechanisms implemented for the vulnerability assessment, according to the Guidelines Reluis-DPC are the following:

- Overturning of full masonry wall (global overturning);
- Overturning of masonry wall located at top level;
- Overturning by horizontal flexure for unconfined masonry walls.

For masonry buildings with metallic ties or concrete ribs, the following failure modes were implemented:

- Overturning by vertical flexure of full masonry walls;
- Overturning by horizontal flexure for confined masonry walls.

According to visual surveys performed after seismic events, some failure modes may be neglected. The probability occurrence of an overturning mechanism depends on the geometrical and mechanical characteristics of buildings. For this reason, some failure mechanisms have been not implemented into the vulnerability assessment.

The structural analysis has been performed by means of a non-linear kinematic analysis, according to the Italian Building Code (IBC 2009).

The analysis of local mechanisms provides the collapse acceleration of each failure mode. Furthermore, using the kinematical model, the return period Tr has been estimated for each failure mode and for each prototype model provide.

For each structural model the mechanism with lower capacity has been chosen in order to develope the fragility curves.

In particular, for confined masonry walls (i.e. model with ties, ribs, etc.) the failure mechanisms by horizontal flexure exhibit a higher probability occurrence. Indeed, for unconfined masonry walls (i.e. model without structural details) the overturning and vertical flexure mechanisms show a higher probability occurrence.

For each prototype model the minimum seismic capacity was assessed. The assessment of the local mechanisms provide the return period Tr that activates the first failure mode (i.e. mechanism with the lower collapse's acceleration). Finally, the coupled seismic assessment provides the minimum return period Tr between the global behaviour (in-plane behaviour) and local behaviour (out-of-plane behaviour).

Starting from the minimum value Tr the acceleration threshold PGA_k was assesses.

This analysis has been performed only for the damage threshold D5, as this is the ultimate condition for the structures (conventional collapse).

In a coupled analysis (in-plane and out-of-plane behaviour) the first damage provides the fragility curve. It is interesting to note that the global (in-plane behaviour) or local (out-of-plane) analysis performed separately provides a damage threshold even greater than the one provided by a coupled analysis. In fact, the first damage which occurs with a coupled analysis provides a probability occurrence lower than an uncoupled analysis.

It is interesting to analyse the effect on the seismic capacity due the global and local behaviour.

The figure 1.35 shows the acceleration threshold PGA_5 for the conventional damage D5 estimated for different approaches. In particular, figure 1.35 shows the PGA threshold by using: the push-over approach on a global behaviour base (blue column), local analysis on local mechanisms base (red column) and coupled analysis approach (green column).

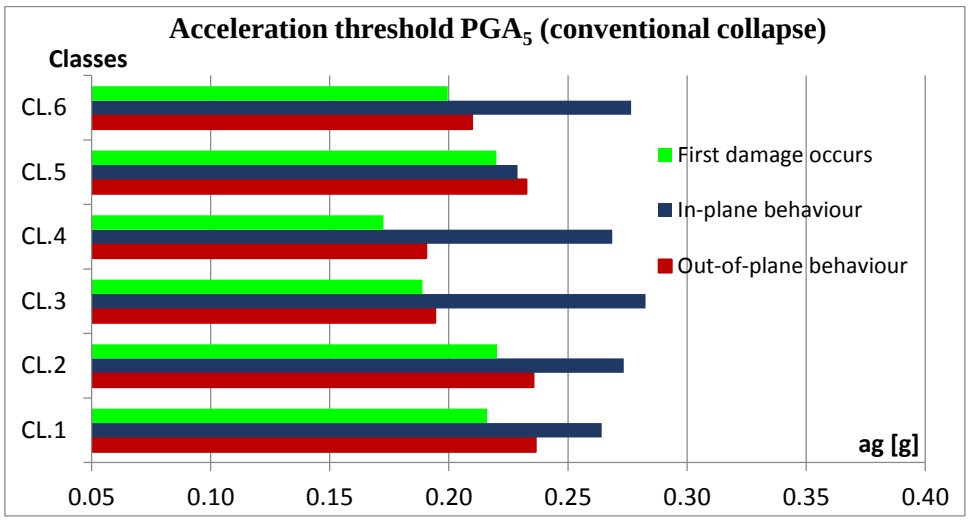

Figure 1.8: *Acceleration threshold PGA_5 according to a conventional collapse (damage D5).*

An analysis of the previous figure shows that the local mechanism limited the seismic capacity of all building classes. This is a critical issue especially for models where there are thrusting elements like as arches or vaults.
In Figure 1.36 the fragility curves obtained from previous analysis are plotted for the damage threshold D5 (unlimited state) and for the six structural classes.

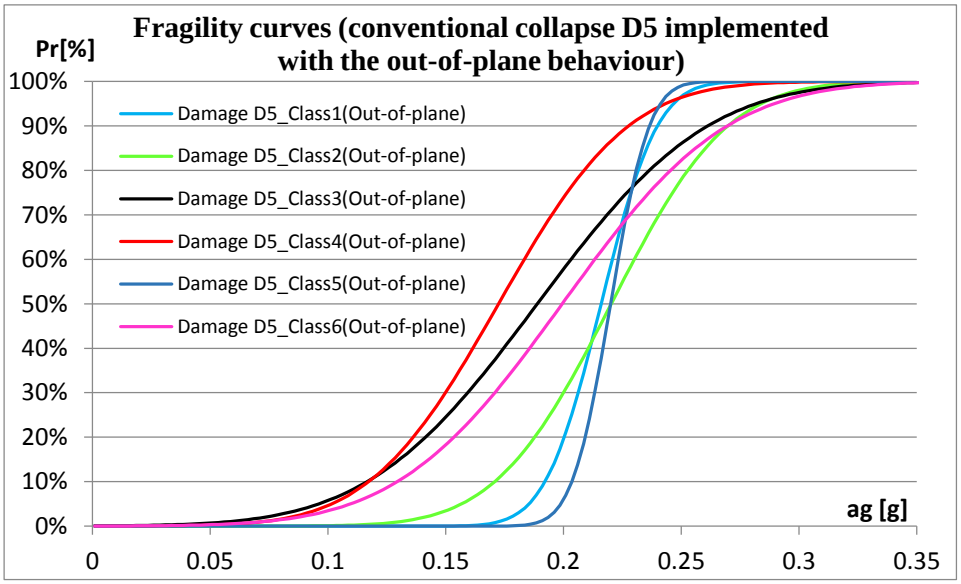

Figure 1.9: *Fragility curves comparison for all structural classes and D5 damage implemented with the out-of-plane behaviour.*

The effects of the thrusting element are shown especially for the structural class 4. In particular, when the fragility curve is calculated using the global analysis, the seismic capacity depends on in-plane response of the walls. In this case, the class 4 shows a higher capacity threshold (figure 1.23).
However, for this class 4 the effect of thrusting elements provides a strong reduction of the seismic capacity due to the local mechanism. These deleterious effects can be seen in previous figure 1.35.
In particular, when the local mechanism is considered, the class 4 shows a greater vulnerability.

This preliminary analysis provides important information about the impact of thrusting elements on the seismic capacity of existing masonry buildings. For this reason the thesis focuses on the behaviour assessment of thrusting elements like as arches and vaults.

Chapter 2

THE BARRELL MASONRY VAULTS

The masonry vaults represent a typical component of most existing historical buildings. These components influence the global behaviour both under vertical and horizontal loads. In particular, most damages and failures were observed after the recent earthquakes especially on masonry vaults.

Therefore, the Historical and Monumental buildings are often characterized by high seismic vulnerability. The lowest seismic performances are associated with the presence of thrusting elements like as arches and vaults.

In this background, the numerical analyses provide important information about the structural behaviour of such elements.

The present Section focuses on a particular typology of vaults generally used as roofs in religious buildings. These vaults typically do not include any backfill and are slender.

These typologies of masonry vaults cannot be analysed with classical approaches where no-tension is assumed. In fact, the tensile strength must be included in order to assess the seismic capacity of these masonry elements.

In next Chapter the classical theory in order to assess the behaviour of masonry vault is discussed.

After such analysis the novelties of the proposed method are introduced (Chapter 3) as improvements of the classical approaches, in particular accounting for the impact of tensile strength on seismic capacity of masonry vaults.

2.1. Overview on masonry vaults

Masonry structures represent a significant part of international architectural heritage. Although they are among the oldest structures, their knowledge is still limited and it is usually difficult to investigate their structural behaviour.

These difficulties are often due to the heterogeneity of the materials and of building techniques. Both the design and building techniques from age to age greatly evolved.

This design approach, in some cases, has led to robust structures. Indeed, many of these structures: historic buildings, churches, railway bridges, etc. were subject to several seismic events without serious damage.

However, this feature is typical of prestigious and strategic structures where same special structural measures were implemented.

Instead, the old design approaches applied on ordinary buildings have generated often poorly built structures and characterized by strong vulnerability.

Only in recent decades designers became aware of how to analyse masonry structures.

These structural elements, during the seismic event, often influence the behaviour of the entire building by means of the interactions with the adjacent structural components.

The recent Italian earthquakes (L'Aquila (Italy), 2009 and Emilia Romagna (Italy), 2012 earthquakes) showed how the vaulted structures are vulnerable. Figure 2.1 shows an example of the vaulted structure, as roofing, included in this study.

Figure 2.1: *Buonacompra church, Emilia Romagna (Italy), damages after 2012-Earthquake.*

Knowledge for ultimate seismic capacity of these structural elements and the collapse mechanism are key aspects both for the structural analysis and for the design of the strengthening interventions.

This Ph.D. thesis focuses on masonry vaults with significant slenderness ratio (span/thickness of the cross section ratio), typically used as roofs in the religious buildings.

For these vaulted roofs the use of classical approaches *[e.g. Heyman 1995]* to evaluate the seismic capacity cannot be applicable or would produce inaccurate results.

For particular geometrical values of span, rise and cross section, the tensile strength of the masonry cannot be neglected as it will be clarified in the following paragraphs.

In the next Section the critical issues of the classical analysis methods are discussed.

2.2. Design approach based on geometrical rules

An investigation of the main analytical models on masonry vaults has been conducted, along with design techniques used for many masonry arches previously designed.

A first purpose is to investigate the classical theoretical approaches which can be used to assess the seismic capacity of curved masonry elements and point out their limitations.

Structural analyses by using numerical models and prescriptions on technical codes have been applied to masonry buildings only recently. The first constructions were designed according to geometrical rules. The geometrical rules, in few cases (i.e. prestigious buildings), were coupled to other structural improvements like as steel ties, regular walls, elimination of horizontal thrusts, etc..

Such design rules were mainly based on past experiences, hence changed significantly during the years *[Katalin 2014, Oppenheim 1992 & Dimitri et al. 2011]*. Generally, for a curved element, given the span and radius of the arch, its thickness could be easily evaluated.

In this Ph.D. thesis the focus is on curved elements made of masonry as arches and barrel vaults, yet including simple arch elements up to the major civil works as arch bridges, viaducts, etc.. A deep awareness of their actual safety level is still lacking.

Many researchers have studied the impact of old design techniques on structural capacity of many existing structures. In particular, the empirical rules have been analysed according to modern structural criteria.

Many studies showed that, in the majority of real cases designed through empiric rules, the structural performances are satisfactory *[Brencich et al. 2007]*. In fact, many of existing structures are still in service although there are both a severe environmental degradation and inadequate maintenance.

Starting from the usual jack arches to the magnificent civil bridges (figure 2.2), in the world there are many samples of masonry arches.

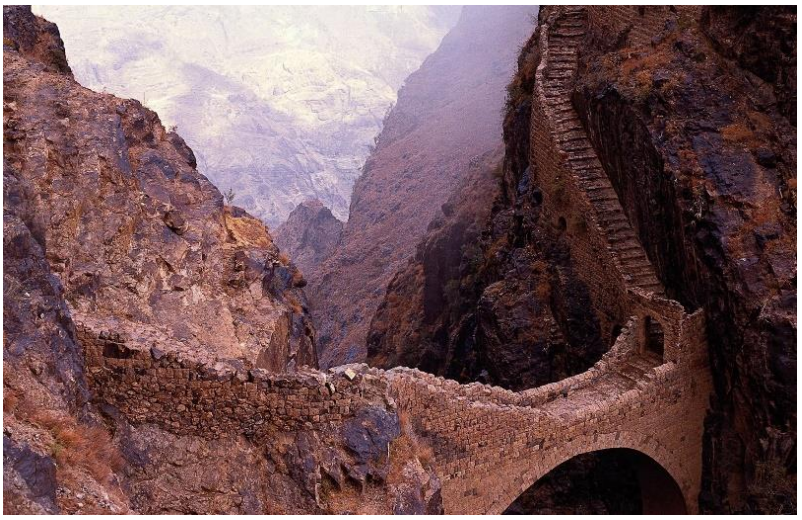

Figure 2.2: *Shaharah arch bridge made of regular natural bricks, Shaharah (Yemen).*

Also in Italian region there are many masonry arch bridges still in service (road and railway network). Many of them have been analysed in several studies under different point of views.

In some recent studies *[De Santis et al. 2012]* the bridges dating back to XIX and XX Centuries and differing both in terms of geographical position and of geometrical properties were chosen.

Surveying the geometrical characteristics of the historical bridges (referring to the vault thickness vs. span for deep arches and to pier top width vs. span and vault thickness for shallow arches), the majority of the existing scrutinised bridges were designed according to the empirical rules *[Brencich et al. 2007]*.

Many of these design approaches have led to robust structures, especially for strategic structures (as like, bridges, aqueduct bridges, viaducts, etc.).

It is interesting to note that these geometrical rules generally provide elements characterized by a large size. Therefore, these design approaches are not compatible with ordinary buildings.

2.3. The classical theory: basic assumptions

The basic assumptions refer to the material behaviour and the no-tension is the main assumption usually adopted in the engineering problems for masonry structures.

No-tension means that material has no tensile strength (or an extremely low value), hence even if tensile strains arise for strain compatibility, corresponding tensile stresses are always zero, masonry cracks and the effective cross-section reduces; this assumption is on safe side and justified by the low tensile strength of typical masonries.

Different behaviour for materials can be considered, namely linear-elastic, cracking and plastic.

For each behaviour, it is well known how to evaluate the failure surfaces *[Giamundo et al. 2014, Prota et al. 2006, Borri et al. 2009, Parisi et al. 2011, 2013 & Augenti et al. 2010]* and how they change accordingly.

In linear-elasticity, the limit surface is defined by a linear expression (solid green line shown in figure 2.3), in particular by two straight lines.

The axial force value at maximum bending moment is equal to 50% of the axial plastic force (centred compressive force).

The failure surface is governed by the most stressed fibre, whose stress level cannot be greater than the compressive strength, σ_0 or lower than zero, considering that the cross section never cracks.

The cracking behaviour takes into account that a portion of the cross section may not react in tension, while the reacting portion is always in compression (stress lower than the compressive strength).

The failure surface is described by means of a non-linear curve (solid ciano line shown in figure 2.3). The cracking curve ends at a compressive force equal to 50% of the pure axial strength; afterwards, the cracking condition cannot exist (cross section is fully compressed).

Finally, under perfect plasticity assumption in compression, the plastic failure surface can be calculated. This failure condition is defined by a quadratic function (solid red line shown in figure 2.3).

Introducing the normalized variables, axial force *p* and flexural moment *m*, for a section with unit depth:

$$p = \frac{P}{P_0} = \frac{P}{s \cdot \sigma_0} \tag{2.1}$$

and

$$m = \frac{6 \cdot M}{s \cdot P_0} = \frac{6 \cdot M}{s^2 \cdot \sigma_0} \tag{2.2}$$

where P and M are the normal force and bending moment, respectively, acting on the cross section, s is the thickness of barrel vault or better the height of rectangular cross section and P_0 is the compressive axial capacity (with a uniform stress equal to compressive strength σ_0 applied on the cross section).

The failure surface can be described and plotted in a normalized form *[Lignola et al. 2008]*, as shown in figure 2.3.

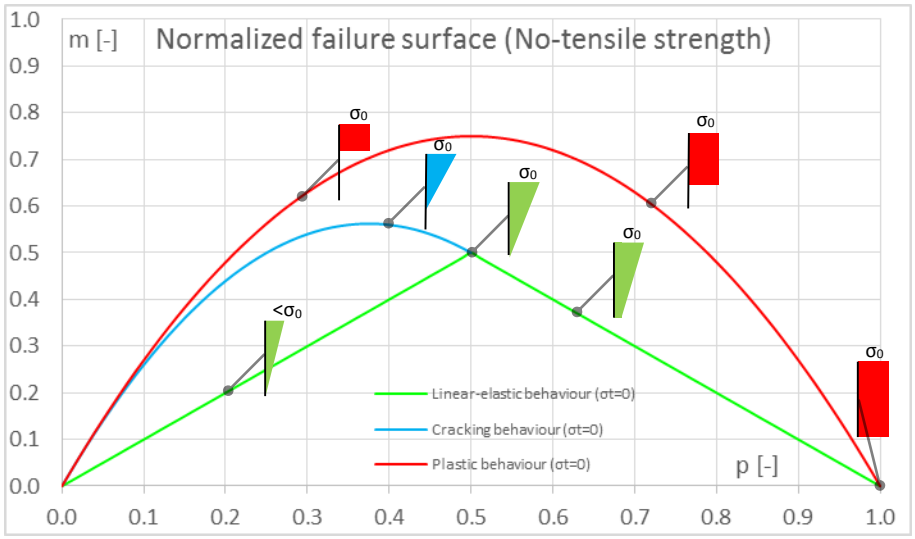

Figure 2.3: *Normalized interaction diagram M-P for rectangular cross section: no-tension assumption.*

The different failure surfaces, shown in figure 2.3, according to the no-tension assumption, start from the origin of axes. Indeed, a pure traction condition for the cross section, is not compatible whit the basic assumptions.
Finally, all the failure surface functions are symmetric to the *p* axis (hence not plotted here on the negative *m* side).

2.4. The Heyman's theory

About the totality of engineering applications on masonry are conducted under no-tension assumption, according to best knowledge of author.
The main effects of tensile strength on the performance of the masonry were studied in the course of time, e.g. *[Fanning et al. 2001a, 2001b]*.
Most of those studies have been performed by using detailed approaches as macro or micro-mechanical modelling. However, both numerical and analytical models accounting for tensile strength and based on a simplified approach, like the present one, are sporadic. In particular, for vaulted masonry structures the Heyman's theory *[Heyman 1995]* is commonly adopted.
The maximum compressive stresses σ_{max} are, on average, typically lower than the compressive strength σ_0 due to the significant dimensions of the cross sections usually associated to the geometric rules.
With reduced contact surfaces only (i.e. localized interaction between brick and mortar due to cracking effects), the normal stresses σ_{max} could achieve high values.
The analytical model for the design of masonry vaults loaded by a generic pattern is based on the following assumptions:

- No tensile strength of materials;
- Compressive strength is infinite;
- No sliding failure mode.

Under these assumptions the hinge mechanism is the only failure mode.
The first assumption is conservative and commonly assumed to assess the capacity of masonry structures.
Since the crushing load is usually higher than the load which activates the hinges especially for unreinforced masonry vaults, the crushing failure is rare *[Buhan et al. 1997 & Foraboschi 2004]*.
The sliding failure mode occurs when the shear stress, at the interfacial surface between mortar and brick, reaches the shear strength. In such conditions the sliding between two contacting surfaces is activated leading to the failure of the vaulted structure *[Drosopoulos et al. 2007]*.
This mechanism could be activated when the angle between the thrust line and the axis of the arch is larger than the friction angle. In each cross section the thrust line is defined by the envelope of resultants of the acting compressive stress distribution, also in cracked condition.
The thrust line should be inside the arch profile, hence its angle with the axis of the arch is usually small.
According to the limit analysis *[Fortunato et al. 2014, Angelillo et al. 2004, 2013 and 2014]*, for a generic load pattern, if the thrust line is contained entirely within the arch boundaries, all the blocks are able to carry the load through compressive stresses only (without $\sigma_{min}<0$).
However, there is not only one thrust line to guarantee stability of the curved element. Indeed, according to the lower bound theorem, any thrust line which is located within the arch boundaries, corresponds to an equilibrium configuration for the curved structure *[Moseley 1843 & Milankovitch 1907]*.
The structure is stable under a generic load if and only if a thrust line entirely contained in the boundaries of arch can be found.
Accounting for the no-tension assumption in cracked conditions the maximum eccentricity of the axial load is equal to *s/2* and reduces at increasing axial load.

Therefore, the thrust line must be always entirely contained in the geometry of the curved element (i.e. eccentricity of axial load contained in the range *–s/2*, *s/2*).

The collapse condition of the curved element is rigorously related to the thrust line's configuration. The collapse can be activated if the number of contact points between the thrust line and boundaries of curved element (thrust line becomes tangent to the arch boundaries) is enough to generate a hinge mechanism (figure 2.4).

Variations of the thrust line configuration can be induced by variations of the horizontal and/or vertical loads. The thrust line configuration, during the entire load history, depends both on load patterns (vertical and horizontal) and on restraint conditions of the curved element.

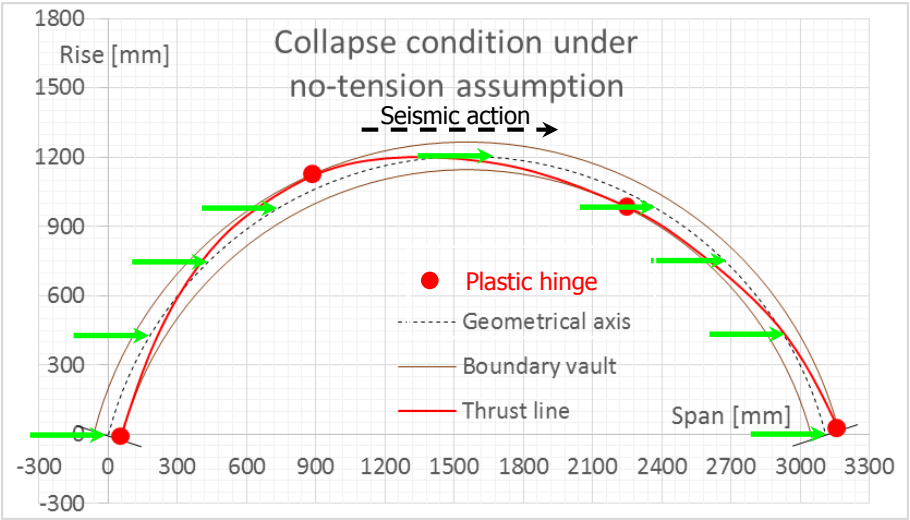

Figure 2.4: *Classic Heyman's theory applied to a masonry arch with fixed restraints (at collapse with fixed gravity load and variable horizontal load).*

2.4.1. Drawbacks of Heyman's theory

The validity of the Heyman's method is recognised in most of engineering applications. Nevertheless, in some cases it could provide inaccurate

solutions. Masonry vaults whit high *span/thickness* ratios cannot be analysed by the Heyman's method.

The reduced thickness of the curved element requires a minimum of tensile stresses already under a gravitational load. Figure 2.5 shows a masonry arch that, under the no-tensile assumption, even under gravity loads has a load multiplier lower than 1.

Therefore, already under gravity acceleration the plastic compatibility conditions cannot be respected. In particular, these effects can be shown by using a non-linear analysis along the gravity direction (i.e. incremental analysis).

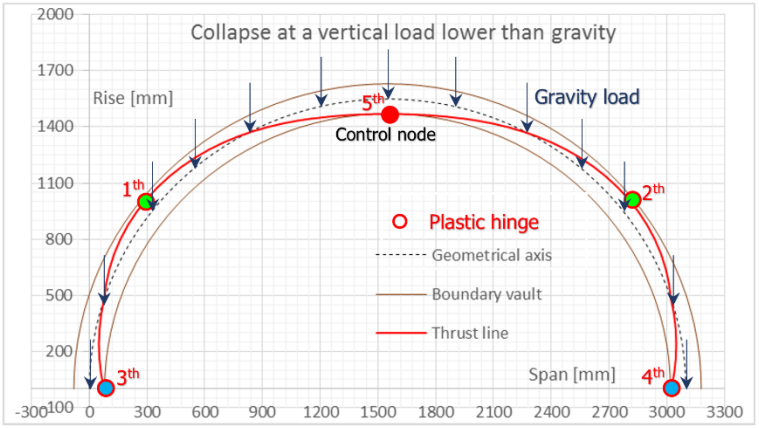

Figure 2.5: *Masonry arch where the no-tension assumption cannot be applied (gravity load only).*

Starting from an unload condition a vertical acceleration ranging from *0* to *g* (i.e. gravity load with an acceleration value of 9.81 m/s^2) can be considered as load pattern to perform an incremental analysis.

The relation between the vertical acceleration and the displacement of a control node shows that collapse occurs for a vertical acceleration lower than the gravity load (figure 2.6).

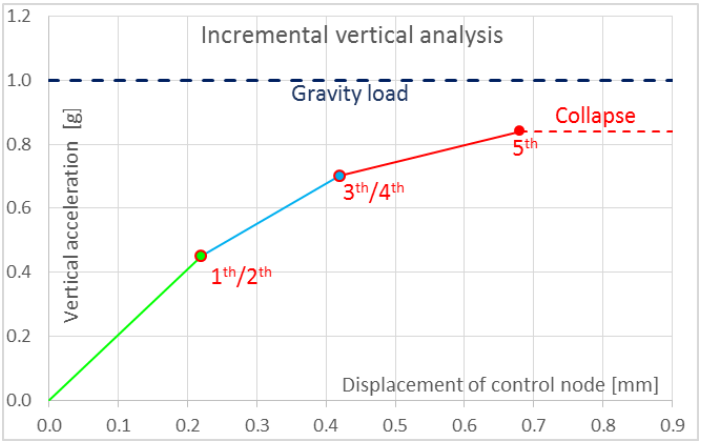

Figure 2.6: *Acceleration-Displacement curve where the no-tension assumption cannot be applied (gravity load only).*

Given both the geometrical and structural symmetry, the plastic hinges 1^{th}, 2^{th} and 3^{th}, 4^{th} occur simultaneously.

This example shows that, only for a vertical load lower than gravitational, a thrust line entirely contained into the boundary of the arch can exist.

Such an arch is supposed to theoretical collapse, even if in reality it stands up since many years and there is no evidence of any structural problem.

The failure condition is given when no thrust line is contained in the arch boundaries.

From a mechanical point of view, in terms of failure domain, if plastic compatibility conditions cannot be respected: some *P*-*M* stress points lie outside the failure surface (or in other words the eccentricity of compressive resultant *P* is higher than limit values given by M_{max}/P ratios on failure surface).

Therefore, for some structures a minimum tensile strength is crucial, especially for masonry vaults without backfill. For these structures the axial load is very small for gravity loads, hence the eccentricities and their fluctuations along the arch profile could be very large.

This feature is characteristic of the vaulted roofing adopted in religious buildings. The present Ph.D. thesis focuses on this critical aspect.

Chapter 3

PROPOSED ANALYTICAL MODEL

The structural behaviour of curved elements can be complex to simulate and to predict exclusively by numerical analyses. Furthermore, the use of refined numerical FEM models cannot be always adopted in practical structural problems.
In this background, the development of simplified analytical modelling approach, manageable and convenient for seismic capacity assessment is certainly valuable. Particular attention should be paid to some structural components, typically found in the monumental buildings and churches, like as arches and vaults.
Therefore, the application of simplified methods is interesting especially for ordinary engineering applications.
The proposed analytical model will be discussed in the next Section.

3.1. Characteristics of the analytical model

Many structural problems concerning masonry structures are usually analysed under no-tension assumptions. The structural analysis of masonry vaults through the Heyman's model can be performed, however this model cannot be applied on particularly slender vaults, like as roofing typically used in religious buildings.
These structures have both a high *span/thickness* ratio and backfill is not present over the vault. In these cases the classical theory cannot be adopted because the hinge mechanism can be activated already under gravity loads and the tensile strength should be included.
A simplified analytical model, which includes the tensile strength, was proposed.

The proposed method represents a useful modelling tool in order to design dynamic tests on masonry vaults and to assess their vulnerability.

3.2. Tensile strength effects on the failure surface

The tensile strength provides different effects on the failure surface.
As previously shown the no-tension assumption provides several failure surfaces according to the behaviour of masonry (linear-elastic, cracking and plastic behaviour based on stress block model).
The low axial force values in such masonry arches at collapse justify the approximated overlapping of the yielding surface and cracking surface. Under this assumption, *s/2* is the maximum eccentricity for the thrust line whatever the low axial load values.
The elastic failure surface is compatible with the brittle behaviour of the masonry material, but is close also to the ideal plastic behaviour.
In any case, the maximum eccentricity is independent on the axial force achieved during the load history, and this makes the Heyman's model easily implementable in a graphical approach.
Conversely, if the tensile strength is included, a dependency of the maximum eccentricity *e* of the thrust line to the axial force values *P* occurs. Nevertheless, as it will be explained in the following, the axial force is low and much lower than its ultimate value. Therefore, the maximum eccentricity can be assumed almost independent on axial load variations until the hinge mechanism is activated.
This assumption facilitates a graphical approach; however it is not essential in the proposed approach and can be avoided.
The tensile strength effect on the failure surface is generally an expansion of the boundaries. The maximum thrust line's eccentricity is dependent on axial force whatever the behaviour of materials.
Once the internal axial load is known, the maximum eccentricity value according to the *P-M* interaction diagram can be calculated as *M/P* ratio.

The model is proposed for the three different behaviours (linear-elastic, cracking and plastic based on the stress block model).
The math expressions of the maximum eccentricity values *e* are provided in closed form.
The no-tensile assumption (i.e. classical approach) can be considered as a particular case of the general proposed method where the tensile strength σ_t is zero.

3.2.1. Linear-elastic behaviour

The failure surface is evaluated in terms of *P-M* interaction domain assuming an unitary depth for cross section. With σ_t the tensile strength value and σ_0 the compressive strength, the relationship between bending moment and axial force is assessed according to equilibrium and stress compatibility equations (3.1), in terms of maximum and minimum stresses, σ_{max} and σ_{min}.

$$\begin{aligned} \sigma_{\max} &\le \sigma_0 \\ \sigma_{\min} &\ge -\sigma_t \end{aligned} \tag{3.1}$$

In linear-elastic assumption the limit condition is obtained by means of the compressive or tensile strength achievement in the most stressed fibre. In particular, the strength can be achieved only on the external fibres.
The figure 3.1 shows the internal stresses according to the elastic limit state for several points of the *P-M* interaction domain.

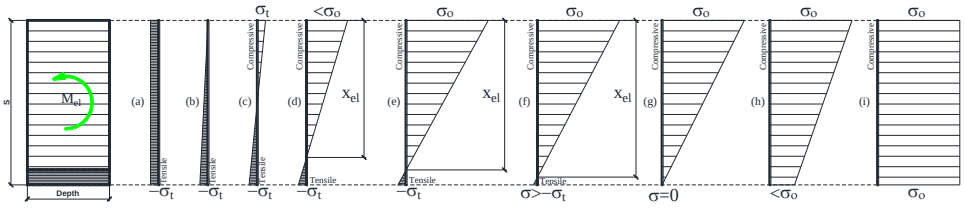

Figure 3.1: *Generic failure conditions for the cross section with linear-elastic behaviour.*

The point *(e)=(M_{bal}, P_{bal})* identifies the balanced condition for the cross section, where both the compressive strength σ_0 and the tensile strength σ_t are achieved.

The neutral axis x_{bal}, can be calculated using the similarity (equilibrium) equations between compressive and tensile diagrams, as follows:

$$\frac{\sigma_0}{x_{bal}} = \frac{\sigma_t}{s - x_{bal}} \tag{3.2}$$

Using the math position $\alpha=\sigma_t/\sigma_0$, the equation (3.2) can be rewritten, it is:

$$\frac{\sigma_0}{x_{bal}} = \frac{\alpha \cdot \sigma_0}{s - x_{bal}} \tag{3.3}$$

Manipulating previous equation (3.3), it provides the neutral axis x_{bal}:

$$x_{bal} = \frac{s}{\alpha + 1} \tag{3.4}$$

where *s* is the thickness of the cross section.

The maximum bending moment, $M_{el,max}$ (i.e. $M_{el,bal}$), increases corresponding to a lower balanced axial force P_{bal}. The math expression of P_{bal} and M_{bal}, can be obtained from an equilibrium equation on the cross section.

In particular, assigned a normal force value, the boundary of the *P-M* interaction domain must satisfy the following equilibrium equation:

$$C - T = P \tag{3.5}$$

where:

- *C* is the resultant compression force achieved into the cross section;
- *T* is the resultant tensile force achieved into the cross section;
- *P* is the axial force externally applied on the cross section.

When the balanced condition is satisfied, the equation (3.5) for a section with unitary depth, can be written as follows:

$$\frac{\sigma_0 \cdot x_{bal}}{2} - \frac{\sigma_t \cdot \left(s - x_{bal}\right)}{2} = P_{bal} \tag{3.6}$$

Using equation (3.4), the previous expression (3.6) can be rewritten, it is:

$$\frac{\sigma_0 \cdot \left(\frac{s}{\alpha+1}\right)}{2} - \frac{\sigma_0 \cdot \alpha \cdot \left(s - \left(\frac{s}{\alpha+1}\right)\right)}{2} = P \tag{3.7}$$

Manipulating the previous equation (3.7), it becomes:

$$P_{bal} = \frac{(1-\alpha) \cdot \sigma_0 \cdot s}{2} \tag{3.8}$$

When the parameter α is equal to zero, the P_{bal} is equal to $P_0/2$ (i.e. Heyman's Theory).

Using the math positions provided by the (2.1), the equation (3.8) can be rewritten in normalized form p_{bal}, it is:

$$p_{bal} = \frac{(1-\alpha)}{2} \tag{3.9}$$

The bending moment $M_{bal}>0$ (using the Navier equations for a section with unitary depth can be calculated, as follows:

$$\begin{aligned} \sigma_0 &= \frac{P_{bal}}{s} + \frac{6 \cdot M_{\text{bal}}}{s^2} \\ -\sigma_t &= \frac{P_{bal}}{s} - \frac{6 \cdot M_{\text{bal}}}{s^2} \end{aligned} \tag{3.10}$$

Replacing the P_{bal} expression into the first equation of the (3.10), it is:

$$\sigma_0 = \frac{(1-\alpha) \cdot \sigma_0}{2} + \frac{6 \cdot M_{\text{bal}}}{s^2} \tag{3.11}$$

Manipulating previous equation (3.11), the maximum bending moment M_{bal} can be calculated as follows:

$$M_{\text{bal}} = \left(\sigma_0 - \frac{(1-\alpha) \cdot \sigma_0}{2}\right) \cdot \frac{s^2}{6} \tag{3.12}$$

$$M_{\text{bal}} = \frac{\sigma_0 \cdot s^2}{12}(1+\alpha) \tag{3.13}$$

Using the math assumption provided in the (2.2) the equation (3.13) can be rewritten, in normalized form m_{bal}, it results:

$$m_{\text{bal}} = \frac{\sigma_0 \cdot s^2}{12}(1+\alpha)\cdot\left(\frac{6}{s^2 \cdot \sigma_0}\right) \tag{3.14}$$

Simplifying the previous equation (3.14) can be rewritten as follows:

$$m_{bal} = \frac{(1+\alpha)}{2} \tag{3.15}$$

Similarly, the relation between bending moment M_{el} and axial force P which provides the failure surface for $P \leq P_{bal}$ (i.e. $p \leq p_{bal}$) and $P \geq P_{bal}$ (i.e. $p \geq p_{bal}$) can be calculated.

According to the compatibility equation (3.1) the failure condition occurs when the σ_{max} or σ_{min} achieve the limit values (σ_0 and $-\sigma_t$ respectively).

For a P value lower than P_{bal} the failure condition depends on tensile strength value σ_t (increasing solid green line shown in figure 3.2). Therefore, the maximum bending moment can be calculated, for a section with unitary depth, by the following equation (i.e. Navier equation):

$$-\sigma_t = \frac{P}{s} - \frac{6 \cdot M_{el,1}}{s^2} \tag{3.16}$$

Manipulating previous equation (3.16), it is:

$$M_{el,1} = \left(\alpha \cdot \sigma_0 + \frac{P}{s}\right)\left(\frac{s^2}{6}\right) \quad \text{for} \quad P \leq P_{bal} \tag{3.17}$$

It provides the bending moment $M_{e,1}$ at varying axial force P.

Using the math assumption provided in the (2.1) and (2.2), the equation (3.17) can be rewritten in normalized form $m_{el,1}$, it results:

$$m_{el,1} = \left(\alpha \cdot \sigma_0 + \frac{P}{s}\right)\left(\frac{s^2}{6}\right)\left(\frac{6}{\sigma_0 \cdot s^2}\right) \tag{3.18}$$

Manipulating previous equation (3.18), its normalized form $m_{el,1}(p)$ can be obtained as follows:

$$m_{el,1} = \alpha + p \quad \text{for} \quad p \leq p_{bal} \tag{3.19}$$

Instead, for a p value higher than p_{bal} the failure condition depends on compressive strength value σ_o (decreasing solid green line shown in figure 3.2).

Therefore, the maximum bending moment $M_{el,2}$ can be calculated by the Navier equation where most stressed fibre has achieved the compressive strength:

$$\sigma_0 = \frac{P}{s} + \frac{6 \cdot M_{el,2}}{s^2} \tag{3.20}$$

Manipulating previous equation (3.20), it is:

$$M_{el,2} = \left(\sigma_0 - \frac{P}{s} \right) \left(\frac{s^2}{6} \right) \quad \text{for} \quad p > p_{bal} \tag{3.21}$$

It provides the bending moment $M_{el,2}$ at varying axial force P.

Using the math position provided in the (2.1) and (2.2), the equation (3.21) can be rewritten in normalized form $m_{el,1}$ as follows:

$$m_{el,2} = \left(\sigma_0 + \frac{P}{s} \right) \left(\frac{s^2}{6} \right) \left(\frac{6}{\sigma_0 \cdot s^2} \right) \tag{3.22}$$

Manipulating previous equation (3.22), it is:

$$m_{el,2} = 1 - p \quad \text{for} \quad p > p_{bal} \tag{3.23}$$

It is interesting to note that the no-tension assumption is simply given by $\alpha=0$.

Therefore, this approach shows a general application falling into the classical theory when no-tensile strength is assumed (i.e. Heyman's Theory).

The maximum bending moment $M_{el}(P)$ depends on the axial force P. The axial force values vary from the pure traction condition P_t to the pure compressive state P_0.

These terms, assuming an unitary depth for the cross section, are expressed as $P_t=\sigma_t \cdot s$ and $P_0=\sigma_0 \cdot s$, respectively.

The envelope of each stress point $M_{el}(P)$ provides the interaction surface. According to previous equations (3.19) and (3.23) the failure surface can be provided in a normalized form (figure 3.2).

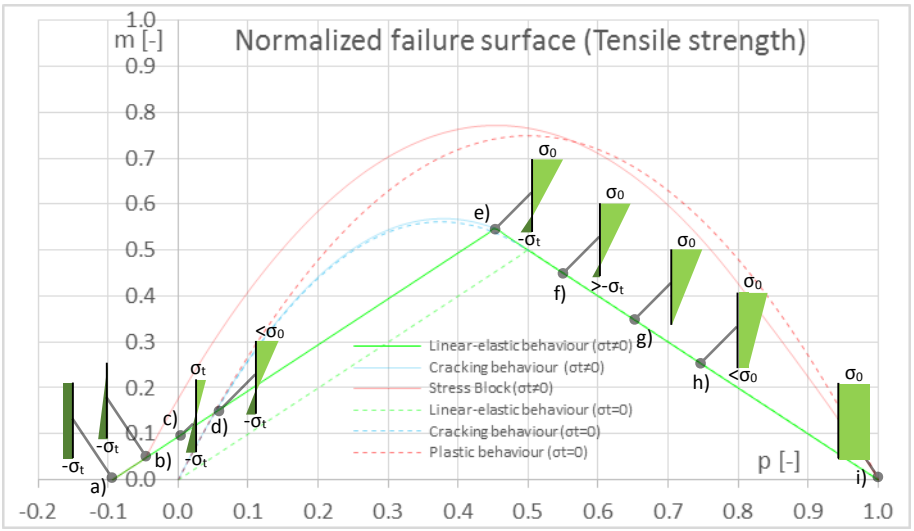

Figure 3.2: *P-M interaction surface with linear-elastic behaviour.*

The failure surface shifts to the left (i.e. traction side).

The analysis of the *p-m* (or *P-M*) interaction domain shows that the maximum value of eccentricity $e_{el}(P)$ of the thrust line depends on normalized axial force P (figure 3.2).

In particular, the eccentricity $e_{el,1}(P)$ can be expressed as follows:

$$e_{el,1} = \frac{M_{el,1}}{P} \quad \text{for} \quad P \le P_{bal} \tag{3.24}$$

Using the math position provided in the (3.1) and (3.2), the previous equation (3.24) can be rewritten using the normalized parameters $m_{el,1}$ and p, it becomes:

$$e_{el,1} = \frac{s \cdot m_{el,1}}{6 \cdot p} \quad \text{for} \quad p \le p_{bal} \tag{3.25}$$

Replacing the expression (3.19) into the previous equation (3.25), it is:

$$e_{el,1} = \frac{s}{6}\left(\frac{\alpha}{p} + 1\right) \quad \text{for} \quad p \le p_{bal} \tag{3.26}$$

Similarly, the maximum eccentricity $e_{el,2}(P)$ can be provided through the following equation:

$$e_{el,2} = \frac{M_{el,2}}{P} \quad \text{for} \quad P > P_{bal} \tag{3.27}$$

Using the math position provided in the (3.1) and (3.2), the previous equation (3.27) can be rewritten using the normalized parameters $m_{el,2}$ and p, as follows:

$$e_{el,2} = \frac{s \cdot m_{el,2}}{6 \cdot p} \quad \text{for} \quad p > p_{bal} \tag{3.28}$$

Replacing the expression (3.23) into the previous equation (3.28), it results:

$$e_{el,2} = \frac{s}{6}\left(\frac{1}{p} - 1\right) \quad \text{for} \quad p > p_{bal} \tag{3.29}$$

It is observed that for $\alpha=0$ (i.e. classical equation without tensile strength) eccentricity is independent on axial load value.

For $\alpha > 0$ and $0 < p < p_{bal}$ the eccentricity of the thrust line is always greater than $s/6$ (maximum value with no-tension and linear-elastic assumption).

3.2.2. Cracking behaviour

According to the proposed model the tensile strength σ_t can be achieved but not exceeded (while in classical assumption, tensile stresses are not accepted).

In a brittle condition, where stresses are virtually higher than tensile strength, that area is excluded from calculations, hence it is assumed to crack. Therefore, two different parts can be identified in the cross section:

- first part of the cross section where the tensile strength has been exceeded causing the cracking of material. The portion which is

under the fibre at σ_t value doesn't provide any contribution to carrying capacity;

- second portion where the stress is lower than the tensile strength or in compression (but lower than compressive strength), hence providing a contribution to capacity.

In cracking assumption the limit condition is obtained by means of the simultaneous achievement of compressive and tensile strengths on a section with reduced thickness $s' < s$.

The structural issue can be solved by using an approach similar to the linear-elastic behaviour, but conducted on a reduced cross section with height equal to $s' < s$.

When the strength values σ_0 and σ_t on the outermost fibres of the reduced section are achieved, the failure condition is triggered. The figure 3.3 shows the internal stress state according to the proposed cracking's model where a tensile strength is included.

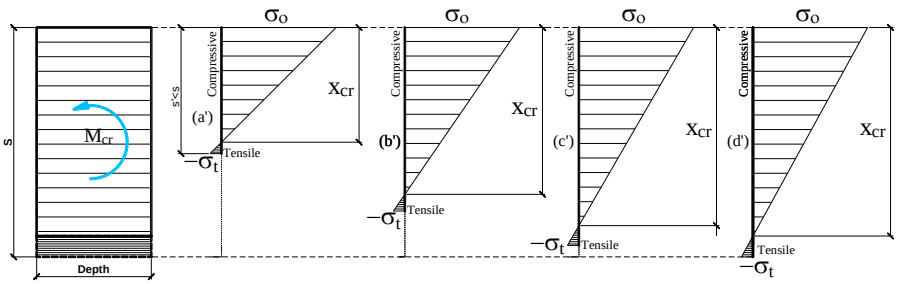

Figure 3.3: *Generic failure conditions for the cross section with cracking behaviour.*

The linear elastic behaviour is always found, but in a reduced cross section. The s' height value can be obtained as a balanced failure condition of reduced cross section, hence including the cracking behaviour.

In particular, using the equilibrium equation (3.5) for the internal stresses shown in figure 3.3, it is:

$$\frac{\sigma_0 \cdot x_{cr}}{2} - \frac{\sigma_t \cdot (s' - x_{cr})}{2} = P \tag{3.30}$$

Given the balanced condition achieved into the cross section, due to the linear behaviour of material, the neutral axis is expressed revising equation (3.4):

$$x_{cr} = \frac{s'}{\alpha + 1} \tag{3.31}$$

Replacing it into the equation (3.30), it is:

$$\frac{\sigma_0 \cdot \left(\frac{s'}{\alpha+1} \right)}{2} - \frac{\alpha \cdot \sigma_0 \cdot \left(s' - \frac{s'}{\alpha+1} \right)}{2} = P \tag{3.32}$$

Manipulating previous equation (3.32), it results:

$$\frac{\sigma_0 \cdot s'}{2}(1-\alpha) = P \tag{3.33}$$

Therefore, manipulating the previous equilibrium equation (3.33) the reduced thickness *s'* can be calculated as follows:

$$s' = \frac{2 \cdot P}{\sigma_0 \cdot (1-\alpha)} \quad \text{for} \quad 0 \le \alpha < 1 \quad \text{and} \quad P \le P_{bal} \tag{3.34}$$

Using the math position (2.1), the equation (3.34) can be expressed, using the normalized parameter *p*, as follows:

$$s' = s \frac{2 \cdot p}{1-\alpha} \quad \text{for} \quad 0 \le \alpha < 1 \quad \text{and} \quad p \le p_{bal} \tag{3.35}$$

The maximum bending moment value $M_{cr}(P)$ depends on axial force. The axial forces can vary from zero to P_{bal} value according to the cracking model.

Indeed, it can be demonstrated that for $P<0$ the balanced failure cannot be achieved if $\sigma_t < \sigma_0$ as supposed. In fact, a net traction cannot be achieved if tensile strength is lower than compressive strength (and both must be reached).

Furthermore, with $P<0$ even assuming a cracking condition, without a balanced failure (i.e. stress in compression is lower than compressive strength) the associated bending moment M_{cr} is lower than $M_{el,1}$. However,

it is noted that this is not conforming to the given assumptions on cracking failure condition.

The relation between bending moment M_{cr} and axial force P, which provides the cracking failure surface, can be expressed thought an equilibrium equation.

In particular, the bending moment M_{cr} can be calculated by using the expression (3.13) because the reduced section (i.e. thickness $s'<s$) behaves according to a balanced equilibrium condition. This term must be added to bending moment due to the eccentricity of axial force P (effect of the thickness reduction).

Therefore, the bending moment M_{cr} can be expressed revising the equation (3.13):

$$M_{cr} = \frac{\sigma_0 \cdot s'^2}{12}(1+\alpha) + P\left(\frac{s}{2} - \frac{s'}{2}\right) \tag{3.36}$$

Using the equation (3.34) the bending moment M_{cr} can be rewritten as follows:

$$M_{cr} = \frac{\sigma_0 \cdot \left(\frac{2 \cdot P}{\sigma_0 \cdot (1-\alpha)}\right)^2}{12}(1+\alpha) + P\left(\frac{s}{2} - \frac{\left(\frac{2 \cdot P}{\sigma_0 \cdot (1-\alpha)}\right)}{2}\right) \tag{3.37}$$

Manipulating the previous equation (3.37), it becomes:

$$M_{cr} = \frac{\sigma_0 \cdot (1+\alpha)}{3} \cdot \left(\frac{P^2}{\sigma_0{}^2 \cdot (1-\alpha)^2}\right) + P\left(\frac{s}{2} - \frac{P}{\sigma_0 \cdot (1-\alpha)}\right) \tag{3.38}$$

$$M_{cr} = \frac{(1+\alpha) \cdot P^2}{3 \cdot \sigma_0 \cdot (1-\alpha)^2} + \frac{P \cdot s}{2} - \frac{P^2}{\sigma_0 \cdot (1-\alpha)} \tag{3.39}$$

$$M_{cr} = \frac{(1+\alpha) \cdot P^2 - 3 \cdot P^2 \cdot (1-\alpha)}{3 \cdot \sigma_0 \cdot (1-\alpha)^2} + \frac{P \cdot s}{2} \tag{3.40}$$

$$M_{cr} = \frac{P \cdot s}{2} + \frac{P^2}{\sigma_0 \cdot (\alpha - 1)} \left(\frac{(\alpha + 1)}{3(\alpha - 1)} + 1 \right) \quad \text{for} \quad 0 \le \alpha < 1 \quad \text{and} \quad P \le P_{bal}$$

(3.41)

Then, using the math position provided in the (2.1) and (2.2), the equation (3.41) can be rewritten in normalized form m_{cr}, as follows:

$$m_{cr} = \left(\frac{P \cdot s}{2} + \frac{P^2}{\sigma_0 \cdot (\alpha - 1)} \left(\frac{(\alpha + 1)}{3(\alpha - 1)} + 1 \right) \right) \cdot \left(\frac{6}{\sigma_0 \cdot s^2} \right) \tag{3.42}$$

Manipulating previous equation (3.42), it results:

$$m_{cr} = \frac{3 \cdot P}{\sigma_0 \cdot s} + \frac{6 \cdot P^2}{\sigma_0{}^2 \cdot s^2 \cdot (\alpha - 1)} \left(\frac{(\alpha + 1)}{3(\alpha - 1)} + 1 \right) \tag{3.43}$$

$$m_{cr} = 3 \cdot p + \frac{6 \cdot p^2}{\alpha - 1} \left(\frac{\alpha + 1}{3(\alpha - 1)} + 1 \right) \quad \text{for} \quad 0 \le \alpha < 1 \quad \text{and} \quad p \le p_{bal} \tag{3.44}$$

The envelope of each $M_{cr}(P)$ provides the interaction surface with a cracking behaviour. Figure 3.4 shows the failure domain according to a normalized form $m_{cr}(p)$.

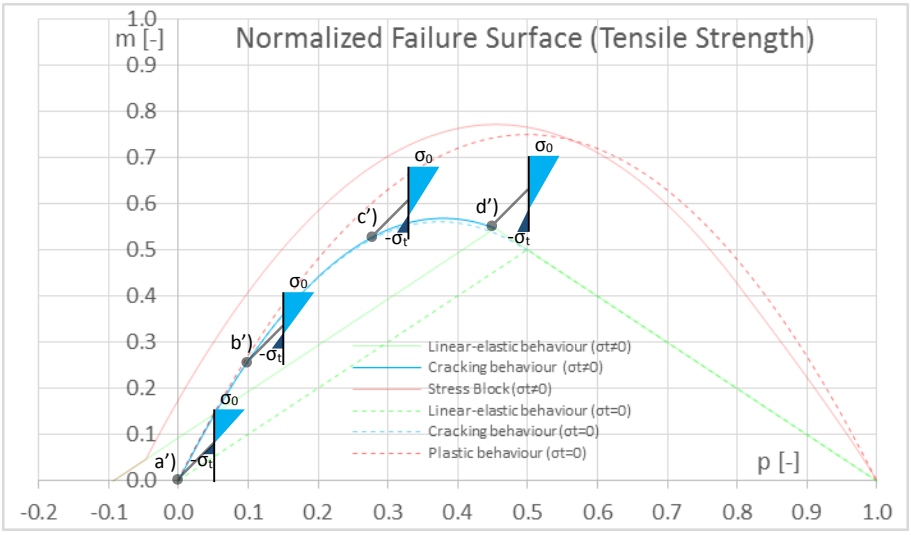

Figure 3.4: *P-M interaction surface with cracking behaviour.*

Even if stress distribution is linear, due to cracking, the curve is a quadratic function of axial force P and bending M_{cr} value is dependent on both the axial force and α parameter.

The maximum eccentricity value $e_{cr}(P)$ of the thrust line depends on the axial force P.

In particular, the eccentricity $e_{cr}(P)$ can be expressed as follows:

$$e_{cr} = \frac{M_{cr}}{P} \quad \text{for} \quad 0 \le \alpha < 1 \quad \text{and} \quad P \le P_{bal} \tag{3.45}$$

Using the math position provided in the (3.2), the previous equation (3.45) can be rewritten as function on normalized parameters m_{cr} and p:

$$e_{cr} = \frac{s \cdot m_{cr}}{6 \cdot p} \quad \text{for} \quad 0 \le \alpha < 1 \quad \text{and} \quad p \le p_{bal} \tag{3.46}$$

Replacing the expression (3.44) into the previous equation (3.46), the equation of the eccentricity e_{cr} becomes:

$$e_{cr} = \frac{s}{2} + \frac{s \cdot p}{\alpha - 1}\left(\frac{\alpha + 1}{3(\alpha - 1)} + 1\right) \quad \text{for} \quad 0 \le \alpha < 1 \quad \text{and} \quad p \le p_{bal} \tag{3.47}$$

It is observed that for $\alpha=0$, the previous equations fall into the classical equation where no-tension is assumed, and eccentricity is $s/2$ exactly in pure bending (i.e. $p=0$) and approximately at low axial load values.

The figure 3.4 shows the main effects of tensile strength assumption in cracking conditions.

Between the linear elastic and cracking failure surfaces, depending on the α value, an intersection point can exist.

In particular, if cracking state occurs or not, it depends on α and, by comparing equations (3.44) and (3.19), the limit values for α can be assessed.

For $\alpha \ge 1/3$ the cracking failure surface is totally below the elastic failure surface, while for $\alpha < 1/3$ the surface is partially above the elastic failure surface (totally above in the case of $\alpha=0$).

3.2.3. Plastic behaviour (stress-block model)

A perfect plastic behaviour can be used for the compressive stress under the no-tensile assumption. But when the tensile strength is assumed, a perfect plastic behaviour cannot be adopted for the tensile stress too.

Therefore, a stress-block based model *[Whitney 1937]* was adopted in order to assess the post-elastic behaviour of the masonry. The stress-block model was adopted both for the compressive and tensile behaviour (the height of the plastic zones in tension is multiplied by 0.5).

The failure surface is very close to the yielding surface obtained under the no-tensile assumption. In fact, the tensile strength has an extremely low value for the masonry material. On average, the tensile strength σ_t is approximately equal to 1/10 of the compressive strength σ_0.

Interaction between bending moment and normal force depends on internal stresses as shown in figure 3.5.

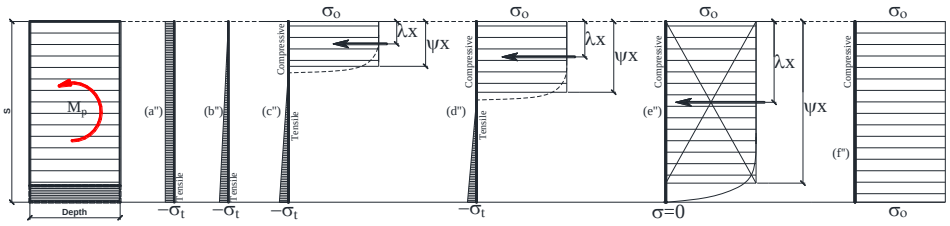

Figure 3.5: *Generic failure conditions for the cross section by using stress-block model.*

In particular, the entire boundary of the *P-M* interaction domain is obtained through different equations.

In normalized form, when p ranges from $-\alpha$ to $-\alpha/2$ (i.e. points a'' and b'' respectively), the behaviour does not differ from the linear elastic one (i.e. there is no compression, the behaviour is governed by the tensile strength). In this range the *P-M* interaction domain is provided by the previous equation (3.19).

When $p \geq 0.5$ some fibres are compressed and according to the stress-block

model the height of the plastic zones is the neutral axis, x_p, multiplied by ψ (usually assumed equal to 0.8), hence it is $\psi \cdot x_p$ and the distance of application point of resultant force from neutral axis is $\lambda \cdot x_p$ (usually assuming λ equal to 0.4).

The neutral axis with plastic behaviour is provided by an equilibrium equation. For p ranging from $-\alpha/2$ to ψ the equilibrium equation (3.5) on the cross section with unitary depth can be rewritten as follows:

$$\sigma_0 \cdot \psi \cdot x_{p,1} - \frac{\sigma_t \cdot \left(s - x_{p,1}\right)}{2} = P \tag{3.48}$$

Manipulating previous equilibrium equation (3.48), the neutral axis $x_{p,1}$ can be calculated, it results:

$$\sigma_0 \cdot \psi \cdot x_{p,1} - \frac{\alpha \cdot \sigma_0 \cdot \left(s - x_{p,1}\right)}{2} = P \tag{3.49}$$

$$\sigma_0 \cdot \psi \cdot x_{p,1} - \frac{\alpha \cdot \sigma_0 \cdot s}{2} + \frac{\alpha \cdot \sigma_0 \cdot x_{p,1}}{2} = P \tag{3.50}$$

$$x_{p,1}\left(\sigma_0 \cdot \psi + \frac{\alpha \cdot \sigma_0}{2}\right) - \frac{\alpha \cdot \sigma_0 \cdot s}{2} = P \tag{3.51}$$

$$x_{p,1} = \frac{2 \cdot P + \alpha \cdot \sigma_0 \cdot s}{\sigma_0 \cdot \left(\psi + 2 \cdot \alpha\right)} \quad \text{for} \quad 0 \le \alpha < 1 \quad \text{and} \quad -\frac{\alpha}{2} \cdot P_t \le P \le \psi \cdot P_0 \tag{3.52}$$

Using the math position provided in the (3.1), the neutral axis $x_{p,1}$ can be expressed through the normalized parameter p:

$$x_{p,1} = \left(\frac{2 \cdot p + \alpha}{\alpha + 2 \cdot \psi}\right) s \quad \text{for} \quad 0 \le \alpha < 1 \quad \text{and} \quad -\frac{\alpha}{2} \le p \le \psi \tag{3.53}$$

The previous equation (3.53) provides the neutral axis up to the limit condition when the cross section is totally compressed (i.e. point e'' shown in figure 3.5). This condition is reached when the neutral axis is $\psi \cdot s$.

The axial force values range from a traction of $-0.5 \cdot P_t$ to a compression value of $\psi \cdot P_0$.

The bending moment $M_{p,1}(P)$ can expressed through the following equilibrium equation:

$$C\cdot\left(\frac{s}{2}-\lambda\cdot x_{p,1}\right)+T\cdot\left(\frac{s}{2}-\left(\frac{s-x_{p,1}}{3}\right)\right)=M_{p,1} \tag{3.54}$$

Replacing the resultant compression C and resultant traction T acting on the cross section, the equation (3.54) can be rewritten as follows:

$$\sigma_0\cdot\psi\cdot x_{p,1}\cdot\left(\frac{s}{2}-\lambda\cdot x_{p,1}\right)+\frac{\alpha\cdot\sigma_0\cdot x_{p,1}}{2}\cdot\left(\frac{s}{2}-\left(\frac{s-x_{p,1}}{3}\right)\right)=M_{p,1} \tag{3.55}$$

$$\frac{1}{12}\sigma_0\left(s^2\cdot\alpha+s\cdot x_{p,1}\left(\alpha+6\cdot\psi\right)-2\cdot {x_{p,1}}^2\cdot\left(\alpha+6\cdot\psi\cdot\lambda\right)\right)=M_{p,1} \tag{3.56}$$

Given the neutral axis $x_{p,1}$ provided in the (3.52), previous equation (3.56) becomes:

$$\begin{aligned}M_{p,1}=&\frac{1}{12}\sigma_0\left(s^2\cdot\alpha+s\cdot\left(\frac{2\cdot P+\alpha\cdot\sigma_0\cdot s}{\sigma_0\cdot\left(\psi+2\cdot\alpha\right)}\right)\left(\alpha+6\cdot\psi\right)\right)+\\&-\frac{1}{6}\sigma_0\left(\left(\frac{2\cdot P+\alpha\cdot\sigma_0\cdot s}{\sigma_0\cdot\left(\psi+2\cdot\alpha\right)}\right)^2\cdot\left(\alpha+6\cdot\psi\cdot\lambda\right)\right)\end{aligned} \tag{3.57}$$

Manipulating the previous expression (3.57), it results:

$$\begin{aligned}M_{p,1}=&\frac{1}{12}\sigma_0\left(s^2\cdot\alpha+\frac{s\left(2\cdot P+\alpha\cdot\sigma_0\cdot s\right)\left(\alpha+6\cdot\psi\right)}{\sigma_0\cdot\left(\alpha+2\cdot\psi\right)}\right)+\\&-\frac{1}{6}\sigma_0\left(\frac{\left(2\cdot P+\alpha\cdot\sigma_0\cdot s\right)^2\cdot\left(\alpha+6\cdot\psi\cdot\lambda\right)}{{\sigma_0}^2\cdot\left(\alpha+2\cdot\psi\right)^2}\right)\end{aligned} \tag{3.58}$$

$$M_{p,1}=\frac{1}{12}\left(s^2\cdot\alpha+\frac{s\left(2\cdot P+\alpha\cdot\sigma_0\cdot s\right)\left(\alpha+6\cdot\psi\right)}{\left(\alpha+2\cdot\psi\right)}\right)-\frac{1}{6}\left(\frac{\left(2\cdot P+\alpha\cdot\sigma_0\cdot s\right)^2\cdot\left(\alpha+6\cdot\psi\cdot\lambda\right)}{\sigma_0\cdot\left(\alpha+2\cdot\psi\right)^2}\right)$$

for $\quad 0\le\alpha<1 \quad$ and $\quad -\frac{\alpha}{2}\cdot P_t\le P\le\psi\cdot P_0$ (3.59)

The bending moment $M_{p,1}$ provided by the equation (3.59) can be rewritten, in normalized form $m_{p,1}$, using the math position (2.1) and (2.2). In particular, the relation between bending moment $m_{p,1}$ and axial force p in normalized form is:

$$m_{p,1} = 6 \cdot \left(\frac{\alpha}{12} - \frac{\alpha\left(2p+\alpha\right)^2}{6\left(\alpha+2\psi\right)^2} - \frac{\lambda \cdot \psi\left(2p+\alpha\right)^2}{\left(\alpha+2\psi\right)^2} + \frac{\alpha\left(2p+\alpha\right)}{12\left(\alpha+2\psi\right)} + \frac{\psi\left(2p+\alpha\right)}{2\left(\alpha+2\psi\right)} \right)$$

$$\text{for} \quad 0 \le \alpha < 1 \quad \text{and} \quad -\frac{\alpha}{2} \le p \le \psi \tag{3.60}$$

The previous equation (3.60) can be applied for p values up to $p=\Psi$.

The maximum eccentricity $e_{p,1}(P)$ can be calculated as follows:

$$e_{p,1} = \frac{M_{p,1}}{P} \tag{3.61}$$

Replacing the equation provided in the (3.59), the previous expression (3.61) becomes:

$$e_{p,1} = \frac{1}{12 \cdot P}\left(s^2 \cdot \alpha + \frac{s\left(2 \cdot P + \alpha \cdot \sigma_0 \cdot s\right)\left(\alpha + 6 \cdot \psi\right)}{\left(\alpha + 2 \cdot \psi\right)} \right) - \frac{1}{6 \cdot P}\left(\frac{\left(2 \cdot P + \alpha \cdot \sigma_0 \cdot s\right)^2 \cdot \left(\alpha + 6 \cdot \psi \cdot \lambda\right)}{\sigma_0 \cdot \left(\alpha + 2 \cdot \psi\right)^2} \right)$$

$$\text{for} \quad 0 \le \alpha < 1 \quad \text{and} \quad -\frac{\alpha}{2} \cdot P_t \le P \le \psi \cdot P_0 \tag{3.62}$$

Using the math position expressed in the (3.1), the eccentricity $e_{p,1}(P)$ of the thrust line can be rewritten in normalized form, it is:

$$e_{p,1} = \frac{s}{p}\left(\frac{\alpha}{12} - \frac{\alpha\left(2p+\alpha\right)^2}{6\left(\alpha+2\psi\right)^2} - \frac{\lambda \cdot \psi\left(2p+\alpha\right)^2}{\left(\alpha+2\psi\right)^2} + \frac{\alpha\left(2p+\alpha\right)}{12\left(\alpha+2\psi\right)} + \frac{\psi\left(2p+\alpha\right)}{2\left(\alpha+2\psi\right)} \right)$$

$$\text{for} \quad 0 \le \alpha < 1 \quad \text{and} \quad -\frac{\alpha}{2} \le p \le \psi \tag{3.63}$$

For $p \ge \Psi$ the failure surface falls into the classical region with no-tensile assumption.

In fact, starting from a section totally compressed, the eventual tensile strength does not impact on the failure surface.

The maximum bending moment $M_{p,2}$ is independent from the neutral axis (external to the cross section). The axial force values range from a compression of $\Psi \cdot P_0$ up to a pure compression value of P_0.

The relationship between bending moment $M_{p,2}$ and axial force P can be calculated from an equilibrium equation, as follows:

$$C = P \tag{3.64}$$

Replacing the resultant compression C, it becomes:

$$\sigma_0 \cdot \psi \cdot x_{p,2} = P \tag{3.65}$$

Manipulating previous equilibrium equation (3.65) the neutral axis $x_{p,2}$ can be calculated through the following equation:

$$x_{p,2} = \frac{P}{\sigma_0 \cdot \psi} \quad \text{for} \quad \psi \cdot P_0 < P \le P_0 \tag{3.66}$$

Using the math position provided in (2.1), the neutral axis $x_{p,2}$ can be expressed through the normalized parameter p, as follows:

$$x_{p,2} = \frac{s \cdot p}{\psi} \quad \text{for} \quad \psi < p \le 1 \tag{3.67}$$

The axial force values range from a compression of $\psi \cdot P_0$ to a maximum compression strength value of P_0.

The bending moment $M_{p,2}(P)$ can be expressed through following equilibrium equation:

$$M_{p,2} = C \cdot \left(\frac{s}{2} - \lambda \cdot x_{p,2} \right) \tag{3.68}$$

Replacing the resultant compression C according to the internal stresses, the equation (3.68) can be rewritten, it is:

$$M_{p,2} = \sigma_0 \cdot \psi \cdot x_{p,2} \cdot \left(\frac{s}{2} - \lambda \cdot x_{p,2} \right) \tag{3.69}$$

$$M_{p,2} = \sigma_0 \cdot \psi \cdot \left(\frac{P}{\sigma_0 \cdot \psi} \right) \cdot \left(\frac{s}{2} - \lambda \cdot \left(\frac{P}{\sigma_0 \cdot \psi} \right) \right) \tag{3.70}$$

Given the neutral axis $x_{p,2}$ provided in (3.66), the previous equation (3.70) becomes:

$$M_{p,2} = \sigma_0 \cdot \psi \cdot \left(\frac{P}{\sigma_0 \cdot \psi} \right) \cdot \left(\frac{s}{2} - \lambda \cdot \left(\frac{P}{\sigma_0 \cdot \psi} \right) \right) \tag{3.71}$$

Manipulating the previous equation, it results:

$$M_{p,2} = P \cdot \left(\frac{s}{2} - \frac{P \cdot \lambda}{\sigma_0 \cdot \psi} \right) \quad \text{for} \quad \psi \le P \le \psi \cdot P_0 \tag{3.72}$$

The bending moment $M_{p,2}$ provided by equation (3.72) can be rewritten, in normalized form, using the math position (2.1) and (2.2). The relationship between bending moment $m_{p,2}$ and axial force p in normalized form is:

$$m_{p,2} = 6p \left(\frac{1}{2} - p \frac{\lambda}{\psi} \right) \quad \text{for} \quad \psi \le p \le 1 \tag{3.73}$$

The previous equation can be applied for a p value higher than $p=\Psi$ up to $p=1$.

The maximum value of eccentricity $e_{p,2}(P)$ of the thrust line depends on normalized axial force P. It can be calculated as follows:

$$e_{p,2} = \frac{M_{p,2}}{P} \tag{3.74}$$

Replacing the equation provided in (3.72), the previous expression (3.74) can be rewritten as follows:

$$e_{p,2} = \left(\frac{s}{2} - \frac{P \cdot \lambda}{\sigma_0 \cdot \psi} \right) \tag{3.75}$$

Using the math position expressed in (3.1), the eccentricity $e_{p,2}(P)$ of the thrust line can be rewritten in normalized form, it results:

$$e_{p,2} = s \left(\frac{1}{2} - p \frac{\lambda}{\psi} \right) \quad \text{for} \quad \psi \le p \le 1 \tag{3.76}$$

The envelope of each $M_p(P)$ value is provided by a quadratic function. In figure 3.6 the *P-M* interaction domain is shown in a normalized form $m_p(p)$.

The maximum of the bending moment $M_p(P)$ is obtained at the balanced axial load p_{bal}.

The failure surface is always outside the interaction surfaces with linear-elastic and cracking behaviour.

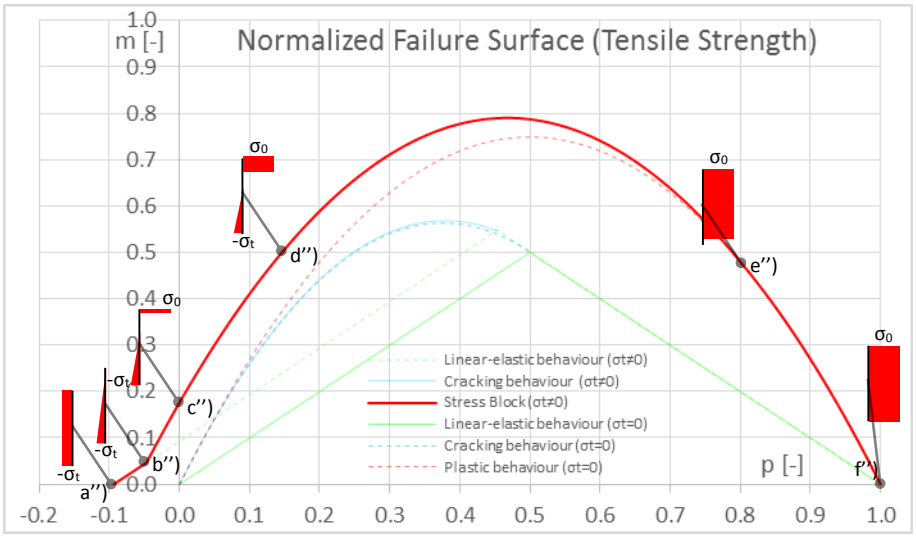

Figure 3.6: *P-M interaction surface with plastic behaviour (stress-block model).*

The equations (3.15), (3.23), (3.44), (3.60) and (3.73) provide the stress compatibility equations that, starting from the gravity load up to collapse condition, must be satisfied.

If the tensile strength is included, even for low axial force values, the eccentricity of the thrust line is not constant with axial load force.

The plastic behaviour represents the most adequate assumption in order to perform a limit analysis.

The proposed model showed that, including tensile strength, the maximum eccentricity of the thrust line can be greater compared to the classical approach (no-tension assumption).

Indeed, the thrust line can be external to the geometrical boundaries of the curved element. These maximum eccentricities are provided in closed form by the equations (3.26), (3.29), (3.47), (3.63) and (3.76).

3.3. Graphical interpretation: fictitious thickness

For a generic load pattern (vertical and/or horizontal load), the masonry arch is in safe condition if the hinge mechanism has not been activated (most likely mechanism).

The collapse condition is activated when the thrust line reaches the maximum eccentricity in a sufficient number of points. However, the maximum eccentricity depends on the material's behaviour and axial load value *P*.

The previous equations (3.15), (3.23), (3.44), (3.60) and (3.73) provide the maximum eccentricities $e_{el,1}$, $e_{el,2}$, e_{cr}, $e_{p,1}$ and $e_{p,2}$ of the thrust line according to the linear, cracking and plastic behaviour, respectively.

The fictitious thickness, which depends on the axial force value achieved during the load history, can be assessed using these equations.

Fixed a generic load step, the axial force value is known (figure 3.7) and the maximum eccentricity value can be calculated for any section (figure 3.8). The fictitious geometry of the masonry arch evolves with the axial loads.

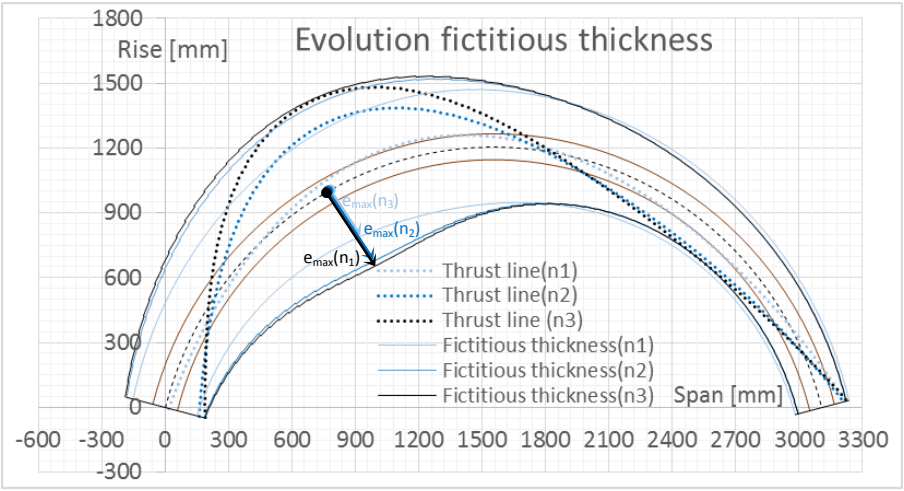

Figure 3.7: *The evolution of the fictitious geometry varying the normal stress values.*

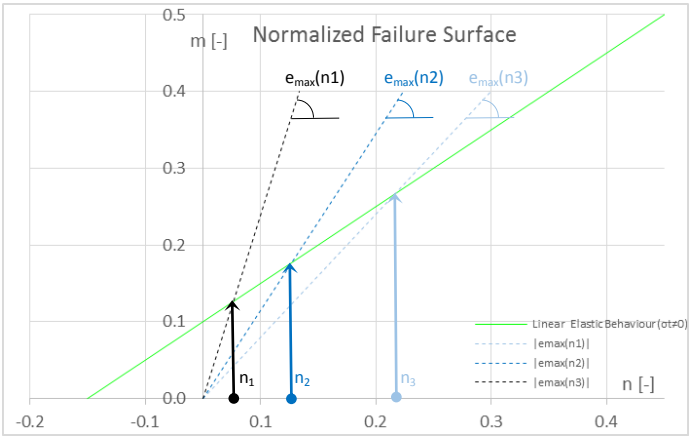

Figure 3.8: *The evolution of the maximum eccentricity e(P) varying the normal stress values P.*

3.3.1. Simplified approach aimed at the graphical method application

For each load step, the thrust line must be contained in boundaries that are altered during the entire load history until the collapse condition.

This aspect determines some limits to the applicability as a graphical method. However, the fictitious geometry could be assumed as fixed, assuming a negligible variation of the axial forces.

With this additional simplification an approach similar to Heyman's method can be performed (collapse multiplier and failure mode). However, it is noted that increasing the axial load, the fictitious thickness reduces. For this reason, the expected increments of axial load should be carefully noted and estimated.

On safe side, the maximum expected axial load value in each section could be considered to evaluate the linked eccentricity. The maximum expected axial load value could be related to the axial load values under gravity conditions.

Therefore, the graphical method can be applied on a curved masonry element where the actual thickness *s* is increased to a fictitious value equal

to twice the eccentricities $e_{el,1}$, $e_{el,2}$, e_{cr}, $e_{p,1}$ and $e_{p,2}$, point wise evaluated according to previous equations.

3.4. Solving algorithm for an arch element

In order to apply the proposed analytical model, a solver algorithm is provided by using a synthetic form.

A masonry arch loaded by a generic load pattern can be analysed by means of a discrete approach. The vertical and horizontal load patterns can be independent and the goal is to assess the maximum load leading to a collapse mechanism. This load value can be easily linked to a lateral acceleration.

Usually, the vertical load is assumed constant throughout the entire load history. The collapse condition can be achieved by using an increasing horizontal load pattern. The horizontal load's shape can be chosen proportional to the masses or to the first natural mode (as classical pushover analyses require).

For some curved elements, the horizontal shaking motion yields to additional not negligible vertical accelerations *[De Santis et al. 2014]*.

In figure 3.9 a masonry vault loaded by a generic vertical and horizontal load pattern is shown.

Starting from the gravitational load, a thrust line variation is evaluated due to horizontal loads. The thrust line can be tangent to the boundary of fictitious geometry of the masonry arch during the loading history. The maximum number of tangent points depends on the restraint conditions. The collapse condition is achieved by means of the hinge mechanism (i.e. sufficient number of tangent points or hinge formations).

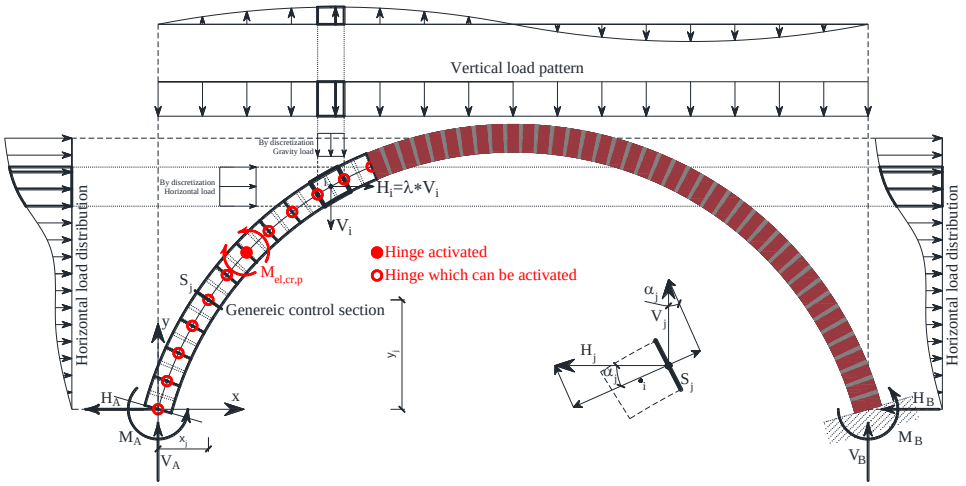

Figure 3.9: *Discrete model of a masonry arch under a generic load pattern.*

The solving equations are based on a discrete approach.

The curved element can be modelled by means of a finite number of elements (finite number of beams n_d and nodes n_{d+1}).

In a generic control section S_i, according to the assumed material behaviour, the plastic hinge can be activated if the maximum bending moment is exceeded.

The restraint devices can be replaced by their reactions. Assuming a fixed arch, defining with ***A*** and ***B*** the two sections at the imposts, for each of them three reactions occurs. H_A, H_B and V_A, V_B are the horizontal thrusts and vertical reactions at the impost sections respectively, whereas M_A and M_B are the bending moments acting in the *X*, *Y* plane. On each discretized element there is a discretized external load V_i and H_i where $i = 1,2,\ldots,n_d$ is the generic element of the arch.

In a Cartesian system *x*, *y* and *z* are defined in the barycentre of the generic arch's element. The reaction values H_B, V_B and M_B at the arch's impost ***B*** can be written based on the H_A, V_A and M_A counterparts as follows:

$$V_B = -V_A + \sum_0^{n_d} V_i$$

$$H_B = -H_A + \sum_0^{n_d} H_i \tag{3.77}$$

$$M_B = -M_A + V_A \cdot l - \sum_0^{n_d} V_i \cdot (l - x_i) + \sum_0^{n_d} H_i \cdot (y_i)$$

Where l is the arch's span, x_i and y_i identify the generic element's location in the local coordinate system.

Similarly the internal forces within the generic element j of the arch, according to figure 3.8, can be expressed as follows:

$$V_j = -V_A + \sum_0^{j} V_i$$

$$H_j = -H_A + \sum_0^{j} H_i \tag{3.78}$$

$$M_j = -M_A + V_A \cdot x_j + H_A \cdot y_j - \sum_0^{j} V_i \cdot (x_j - x_i) - \sum_0^{j} H_i \cdot (y_j - y_i)$$

Where the index i identifies all the elements starting from the impost's section $\boldsymbol{A}$ to the control section s_j.

The internal axial and shear stresses, P_i and T_i, can be calculated as:

$$P_j = H_j \cdot \cos\alpha_j - V_j \cdot \sin\alpha_j$$

$$T_j = -\left(H_j \cdot \sin\alpha_j + V_j \cdot \cos\alpha_j\right) \tag{3.79}$$

where α_j is the angle of the axis normal to the control section s_j with respect to the horizontal axis x (local tangent at the curved element).

The bending moment can be calculated by using the third equation of the system (3.78).

On each element, a horizontal force is applied, expressed as $H_i = \lambda \cdot V_i$, where the natural number λ is the multiplier of the horizontal load, for a generic load step. The λ factor can be assumed also as a function (e.g. modal shape)

of a further parameter increasing up to the collapse condition (hinge mechanism), hence related to the collapse's acceleration.

The internal forces M_j, P_j ratio provides the eccentricity of the thrust line at any load step. Denoting with $M_0(P_j)$ the maximum bending moment according to the behaviour assumed for the masonry material (i.e. linear-elastic, cracking or plastic), at each section the additional compatibility condition, written as follows, must be satisfied.

$$\frac{M_j}{P_j} \le \frac{M_0\left(P_j\right)}{P_j} \quad \text{that is} \quad e_j \le e_{j,0}\left(P_j\right) \tag{3.80}$$

Where $e_{j,0}$ is the maximum eccentricity previously discussed. In all control sections the plastic hinges can be activated.

In order to apply an incremental analysis aimed at the collapse activation, in the generic load step where the hinge is activated, the structure must be updated. If j' is the cross section where the hinge is activated, it is $M_{j'} \le M_0(P_j)$.

Indeed, the compatibility equations for any step after the first hinge activation must be satisfied. The structure is updated during the loading history up to the ultimate collapse mechanism.

The incremental analysis provides both the collapse's acceleration and the evolution of the hinge mechanism.

If the assessment of the collapse acceleration is the goal, the solution is even easier by using the Limit Analysis Theorems.

According to the framework of the lower bound theorem, each possible thrust line lying within the fictitious arch boundaries, corresponds to an equilibrium configuration of the curved element where the tensile strength is assumed. The solver algorithm can be implemented as schematically discussed below:

- The structure must be transformed into its equivalent isostatic structure by the elimination of restraint devices;

- They must be replaced by the related unknown reactions X_k with $k=1,2,...,k$ and k is the number of statically indeterminate reactions;
- The internal force diagrams are evaluated (bending moment and axial force) on the equivalent isostatic structure due to the external gravity loads V_i (M_{Vj} and P_{Vj}), the horizontal loads $H_i=\lambda \cdot V_i$ (M_{Hj} and P_{Hj}) and the statically indeterminate reactions (M_{Xk} and P_{Xk});
- The global internal forces include the different effects as shown:

$$\begin{aligned} P_j &= P_{V_j} + P_{H_j} + X_K \cdot P_{X_K} \\ M_j &= M_{V_j} + M_{H_j} + X_K \cdot M_{X_K} \end{aligned} \tag{3.81}$$

- Finally the compatibility equations (3.80) must be imposed;
- In order to determine the static multiplier λ, a numerical procedure can be conducted that transforms the structural problem into a linear programming problem optimizing the system of equations given by (3.81).

Chapter 4

ANALYTICAL MODEL VALIDATION

The computing capacity of tools now available allows the development of complex numerical models that can be used to evaluate many structural aspects. The heterogeneity of the masonry often makes these numerical models very complex and unreliable when applied to structures different from those originally used to develop them. For these structures and their components (individual walls, vaults, etc.) the experimental support is necessary both to assess the mechanical behaviour and to validate models by means of numerical and experimental comparisons.

In this background, the experimental tests can provide an efficient contribution to the calibration and interpretation of simplified numerical and analytical models.

A simplified analytical model, which includes the tensile strength, was proposed (Chapter 3). Validation of the analytical model is provided by comparing predictions of the load capacity and the failure mode with those obtained from previous shaking table test series on a full scale masonry vaults.

The experimental results have been obtained from dynamic tests conducted in the laboratory of Department of Structures for Engineering and Architecture of the University of Naples, Federico II.

Then, the calibrated numerical model was used to design the dynamic tests on another more complex real scale masonry specimen.

4.1. Analytical model validation by means of experimental dynamic investigation

The proposed method has been validated by means of past experimental shaking table tests discussed in detail in *Giamundo et al. (2015)*. Several experimental tests on one full scale masonry vault were performed at the Department of Structures for Engineering and Architecture, University of Naples Federico II.

The goal was to assess the seismic capacity of masonry vaults and the strengthening effects after damage. Indeed, the tests have been carried out in two parts: in a first part the tests have been performed on the unreinforced specimens; in a second step the dynamic tests have been performed again on the specimen strengthening by means of a TRM (Textile Reinforced Mortar) system and repaired by means of mortar joint repointing and grout injections.

In next section, the proposed model was validated by comparison with the experimental results shown for the unreinforced specimen only.

4.2. Specimen characteristics

Several experimental tests on shaking table have been conducted. The masonry specimen was made of solid facing clay bricks with size $(25 \cdot 5.5 \cdot 12)$ cm^3 and pozzolana-based mortar joints (10 mm thick).

The vaults have been built on a rigid steel beams system, which is part of the test setup (figure 4.1).

This system provides a rigid constraint between the shaking table and vault's imposts. Furthermore, the steel frame guarantees an adequate level of safety during the experimental tests.

Figure 4.1: *Specimen tested in order to validate the proposed analytical model.*

The geometry of the specimen and its structural characteristics are representative of the vaulted roofs commonly adopted in the historical religious buildings, yet respecting some lab constraints.

In-plane geometry of the curved element is characterized by a segmental arch profile which is less than a semicircle.

The span, rise and depth values of the vault are 298 cm, 114 cm and 220 cm, respectively. Further details about the geometry of the first specimen are provided in figure 4.2, where the two principal views have been shown.

The backfill, usually acting on traditional vaults, provides a beneficial effect on the structure *[Melbourne et al. 1995, Callaway et al. 2012 & Gago et al. 2011]*. However, this effect is not present in vaulted roofing of churches.

Therefore, in this experimental work, in order to simulate such vault typology, the specimen has been tested without any backfill.

The specimen was constrained on the shaking table and such boundary conditions simulate the action of the ties frequently adopted in the retrofit of historical vaulted structures.

In a multiscale approach, perfect fixing of the imposts represents the first step to focus on the vault itself, while different boundary conditions would

have added further variables to the system resulting in a more complex problem interpretation.

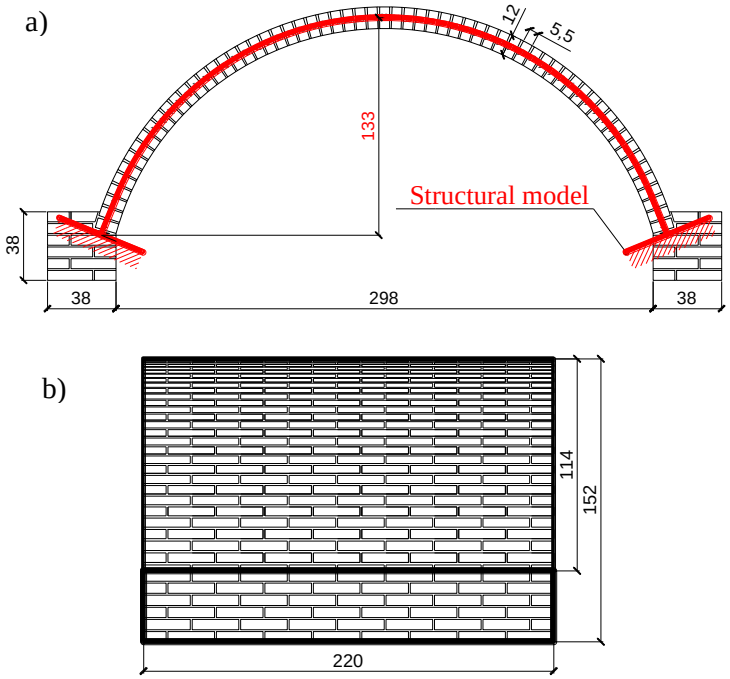

Figure 4.2: *Specimen geometry and structural model adopted: a) front view, b) lateral view, respectively.*

Rationale and limits of previous shaking table tests are discussed elsewhere, while the focus of present thesis is the simplified modelling, hence the validation by comparison with available experimental tests and configurations.

More complex tests have been done and are foreseen for the future and the proposed model will be able to assist in the design of the future tests accounting for more slender walls or different structural geometries.

The unreinforced specimen has been tested by using several signals (i.e. replicas of natural and artificial accelerograms, with a frequency content

compatible with the tested specimen) repeated increasing the peak accelerations, as commonly done in shaking test programs.
The effect of replicas is expected to yield to strength decay and, to account for tensile strength uncertainty, parametric analyses can be performed on a range of possible strength values.
At the end of each test, visual surveys on the specimen have been conducted.

4.3. Experimental results

The unreinforced specimen has been tested by means of seven artificial signals with increasing intensity.
Until to the fifth test no substantial damages have been detected. After the last signal, in several locations, crack openings at the interfaces between mortar and brick have been detected.
The crack openings denote the hinges activation and have been observed both at the intrados and the extrados of the masonry vault. Cracking at the intrados occurred along almost the entire depth of the joint at about 1/6 of the span length.
At the extrados the cracking has involved a larger number of joints. The formation of all the described cracks occurred at the interfaces only by means of a mechanism of “crack opening and closing”.
The cracks occurred at almost symmetrical locations at the inversion of the shaking direction. In order to highlight such mechanism, in figure 4.3 a still image taken from a video record of the tests shows the crack tips highlighted by a red circle (lateral loads acting from left to right).
The experimental results confirm the hinge mechanism to be the limiting failure mode in masonry vaults compared to sliding or crushing failure.
The crack opening remarks the triggering of a hinge mechanism in the vault. The vault's collapse was prevented by stopping the test.

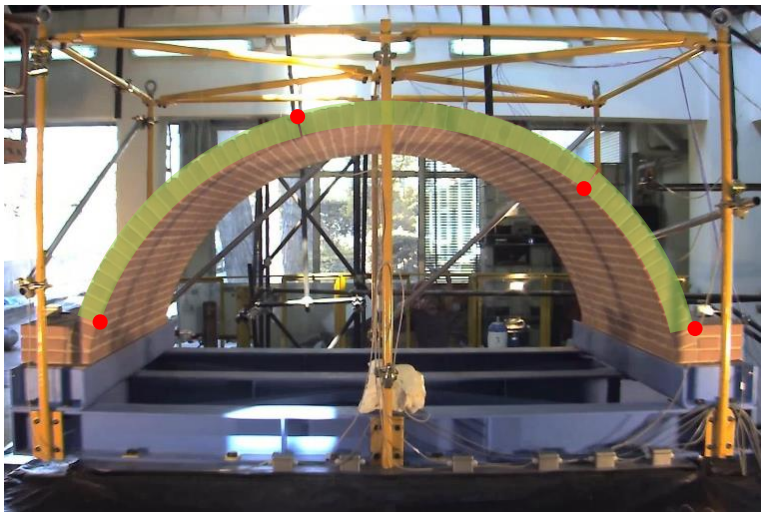

Figure 4.3: *Last signal for the first unreinforced specimen (hinge mechanism activated without collapse).*

However, the specimen went very close to the hinge mechanism (i.e. four hinges activated). The fourth hinge activated at an acceleration close to 0.48g.

The tests have been carried out in two phases on an unreinforced and strengthened specimen. The analysis focuses on unreinforced vault.

4.3.1. Tensile strength estimation

An additional static vertical load test has been performed in order to estimate the tensile strength of masonry vaults (best fitting of tensile strength to simulate the test, see *Giamundo et al. 2015*). Furthermore, through this test the residual vertical load capacity of the vault has been estimated also.

The static vertical load test has been performed after the last shaking table test.

During the test the vault has been monitored by means of a linear variable displacement transducer (LVDT). The LVDT device has been placed at the keystone location.

The masonry specimen was uniformly loaded by a vertical distributed load applied at the keystone zone. In particular, the load was applied on a length of 40 cm along the whole depth of the vault. It was quasi-statically applied to the vault at increasing step.
The load-displacement curve experimental estimated has been compared with the curve obtained numerically by a non-linear numerical FEM model. This comparison has been performed in order to estimate the tensile strength of the masonry material.
Through this test a tensile strength σ_t = 0.16 MPa has been estimated. This value was considered for the validation of the proposed analytical model.

4.4. Analytical modelling and experimental comparison

The specimen experimentally tested has been analysed by using the proposed simplified model.
The gravity condition has been modelled by a fixed vertical load during the entire load history. Therefore, the collapse condition occurs by means of a monotonically increasing horizontal acceleration. The internal force variations are due to horizontal load increase only, by means of a monotonically increasing horizontal acceleration. The horizontal load pattern is proportional to the masses of the structure, while vertical load is gravity. The increase of the seismic load was modelled by using a load pattern proportional to the masses.
The masonry material (mortar and brick) was modelled by using a homogeneous material.
The vault was modelled using a discrete approach. In particular, the curved element has been discretized in elements.
The plastic failure surface has been chosen for the masonry material. According to this assumption the interaction *P-M* surface is provided by equations (3.19), (3.60) and (3.73).

Furthermore, the maximum eccentricity values for the thrust line are provided by equations (3.26), (3.63) and (3.76).

In this phase, the structural analyses do not take into account full variability of the mechanical properties because the goal is validate the proposed analytical model.

Starting from mechanical parameters estimated by experimental tests, a reasonable range of mechanical characteristics has been provided in the paragraph 4.5 in order to evaluate the collapse accelerations for the unreinforced specimens.

The expected acceleration according to the estimated tensile strength is shown in table 4.1. The collapse acceleration has been calculated for the unreinforced specimen.

As it will be clarified in the next section, the tensile strength has an important effect on the seismic capacity and its value must be accurately estimated.

The collapse multiplier λ has been calculated by means of the lower bound theorem. The analytical model takes into account for the axial load variations. This last aspect produces a continuous update of the fictitious geometry within which the thrust line must be contained.

With the knowledge of λ, the PGA values can be assessed at the collapse condition for the specimen. In table 5.1 the results are shown in terms of PGA values at collapse condition for the masonry specimen.

Table 4.1: *PGA values at mechanism activation.*

PGA Specimen	Collapse acceleration [g]
Experimental threshold	0.48
Numerically estimated (σ_t = 0.16)	0.54

The vault was discretised into 60 elements and a specific weight of 18 kN/m^3 was assumed for the masonry. Hence, in the structural model there are 61 control sections in which plastic hinges can be activated.

The maximum horizontal load multiplier was evaluated having the thrust line inside the fictitious boundaries of the arch. A sensitivity analysis was conducted on the number of elements for the discretization and its impact is less significant than the tensile strength.

The present choice represents a compromise between accuracy and efforts, where the most relevant parameter in such slender walls without backfill is the tensile strength.

In figure 4.4 the thrust line configuration is shown for this specimen at the theoretical collapse condition (i.e. λ=0.54g). The internal forces M_j and P_j are shown as hollow signs inside the interaction *P-M* surface, in solid line in figure 4.5.

Furthermore, an incremental analysis has been performed in order to evaluate the progression of the plastic hinges up to theoretical collapse (see figure 4.4 and figure 4.5).

M_j and P_j points clearly reach the plastic surface in four locations representing the hinges formation (figure 4.4).

It is interesting to note that, the hinge location corresponds to the section where the internal forces M_j and P_j intersect the interaction surface or, similarly, corresponds to the tangent point of the thrust line to the fictitious boundaries of the arch (figure 4.5).

It is worth noting that experimental test was stopped at 0.48g to prevent collapse, however the formation of the fourth hinge almost occurred experimentally (figure 4.3).

These numerical results have been shown for the estimated tensile strength and they are in satisfactory agreement with hinge location (a comparison of experimental results is in figure 4.3 and theoretical outcome is in figure 4.4) and corresponding experimental load.

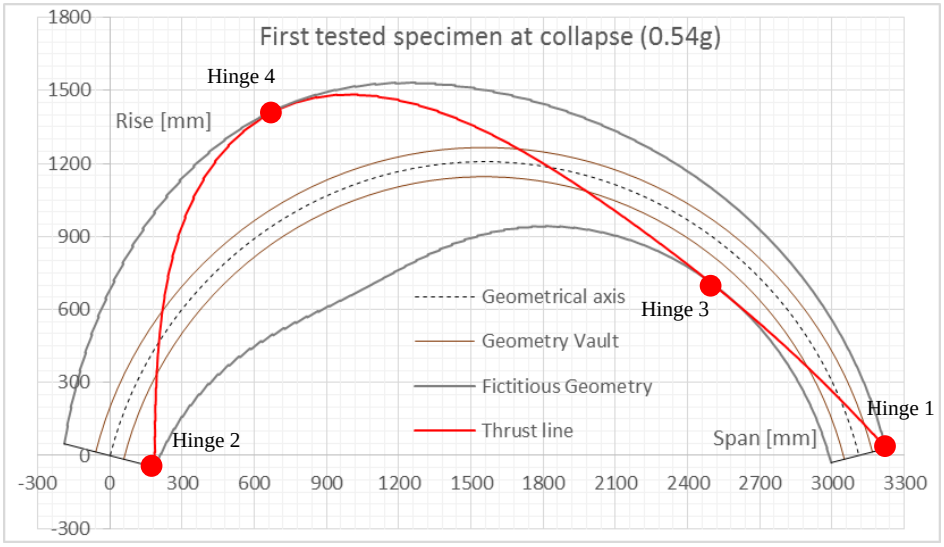

Figure 4.1: *Theoretical thrust line configuration for the specimen (hinge mechanism activated).*

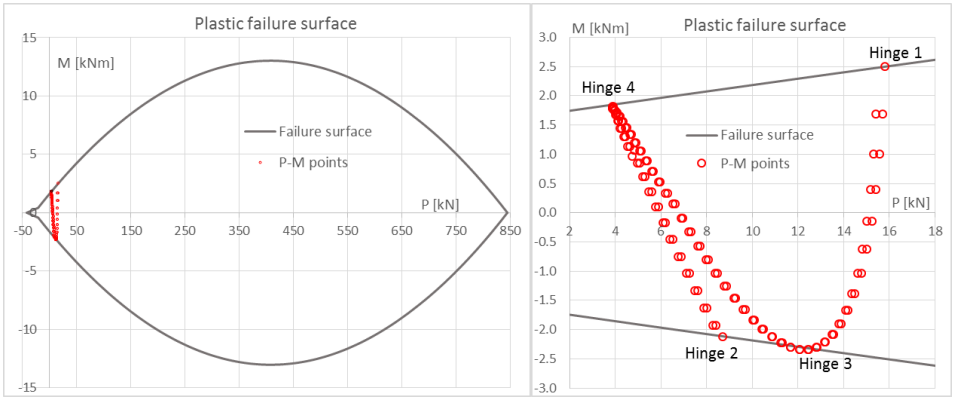

Figure 4.2: *P-M points in the plastic failure surface.*

The collapse multiplier λ was evaluated by using the lower bound theorem. The numerical result provides a λ value equal to 0.54 g. The theoretical PGA value at collapse is very close to experimental PGA value achieved during the last signal. It is recalled that the specimen showed no clear collapse due to a timely ending of the dynamic sequence. For this reason the collapse multiplier numerically estimated (λ=0.54) is higher at the experimental value (λ=0.48).

For the ultimate step, the stresses: N_i, T_i and M_i, can be calculated for each control section providing the internal stresses at collapse.
The agreement in terms of both activation multiplier and failure mode (i.e. hinge mechanism pattern, comparing experimental locations in figure 4.3 and theoretical outcomes in figures 4.4) is very satisfactory.

4.5. Sensitivity analysis

The tensile strength must be included to assess the seismic capacity of slender barrel vaults. A simplified analytical model, in the framework of limit analysis, was proposed which includes the tensile strength.
Tensile strength in these analyses is affected not only by the strength of basic materials, but also by the bond at the unit-to-joint interfaces, which could be rather difficult to assess reliably.
Sensitivity of the predictions to variations of tensile strength is discussed. Validation of the analytical model has been discussed by comparing predictions of load capacity and failure mode with those obtained previously from shaking table tests on a full scale masonry barrel vault (see Section 4.4).
These analyses show the effects of the tensile strength combined with different geometrical and mechanical parameters on the seismic response of the vaults.
Starting from the geometry of the masonry vault experimentally tested (figure 4.2) a sensitivity analysis has been performed by using the validated model.

4.5.1. Parameters of the sensitivity analysis

Starting from the geometry shown in figure 4.2, several analyses have been performed varying both the geometrical and mechanical parameters.

With regard to the geometry, each parameter has been normalized to the span *l* of the tested specimen (*l=3.1 m*).
In this way, both the rise of the vault *f* and the thickness of the cross section *s* are functions of the span value.
In particular, the ratios between rise and span of the arch *f/l* range from 0.15 to 0.5.
Conversely, the ratios between thickness of the cross section and span of the vault *s/l* range from 0.025 to 0.25.
The previous geometrical values, increased by discrete steps, allow assessing structural cases which are usually found in the engineering practice.
The mechanical properties were considered variable in terms both of specific weight and tensile strength.
In order to assess the structural capacity of masonry commonly found in practice, three values of the specific weight have been chosen according to the typological existing masonry buildings described into the Italian Building Code (IBC 2009).
In particular, values equal to 11 kN/m^3, 16 kN/m^3 and 20 kN/m^3 have been used for a masonry made of hollow clay brick, tuff stone and solid clay brick, respectively.
Finally, the influence of the tensile strength on the structural behaviour has been assessed.
The parametric analyses have been performed by using initially the no-tensile strength assumption (Heyman's Theory), up to a maximum value of 0.3 MPa. Starting from a zero value of the tensile strength, five discrete values of 0, 0.08, 0.16, 0.24 and 0.3 MPa, have been used.
The compressive strength has been fixed as 3.2 MPa having practically no effect on the structural behaviour of the vault.
In fact, the normal stress values are extremely low at collapse condition. This means that the *P-M* points lie on the left side of the failure domain (i.e. low *P*).

The ultimate conditions, on the left side of the failure surface, are mainly governed by the tensile strength. Therefore, as long as the normal stresses are low, the compressive strength has no impact on the structural capacity of masonry vault.
In order to perform a sensitivity analysis, the previous parameters were combined.
The plastic failure surface has been chosen for the masonry material (equations (3.19), (3.60) and (3.73))

4.5.2. Results of the sensitivity analysis

In the following paragraph some results of the sensitivity analysis are shown by using several graphs.
The figure 4.6 shows the development of the λ factor varying the *s/l* ratio for different discrete values of the *f/l*. These curves were calculated by using the proposed model under a no-tensile strength assumption. In order to assess the effect of the specific weight on ultimate condition, when zero tensile strength is assumed, the numerical results are shown for the two extreme values: γ_m=11 kN/m^3 (shades of green) and γ_m=22 kN/m^3 (shades of red).
The previous figure shows a negligible influence of the specific weight on the collapse multiplier under no-tensile strength assumption. This effect is very evident for slender masonry barrel vaults (with low s/l ratio) and for round arches with *f/l* tending to 0.5 value.
It is interesting to note that for several cases to no-tensile strength assumption corresponds a zero value of the λ parameter. This means that they are in a critical static condition already under gravity load.
This is a crucial aspect for the slender vaults where a minimum of tensile strength should be considered. Increasing the tensile strength, the influence of the specific weight on the structural capacity is more evident.

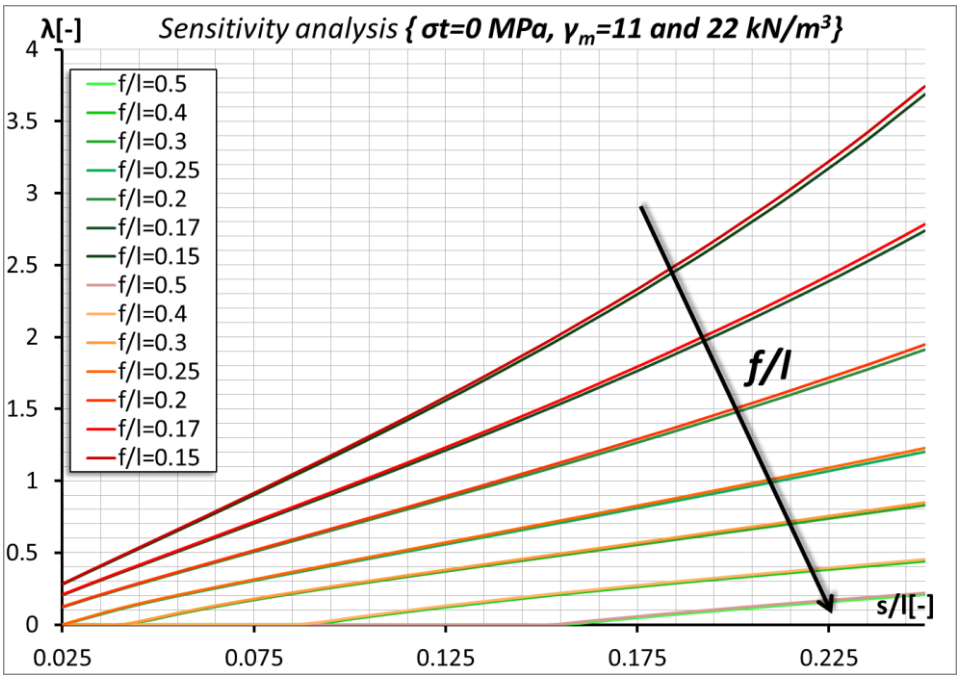

Figure 4.3: *Results of the sensitivity analysis: development of λ value with σ_t=0, γ_m=11 kN/m³ (shades of green) and γ_m=22 kN/m³ (shades of red).*

The figure 4.7 shows the development of the λ values varying the *s/l* ratio for different discrete values of *f/l*. These curves are provided accounting for a tensile strength of *0.16* MPa.

In the following, the numerical results are shown for the two extreme values of the specific weight: γ_m=11 kN/m^3 (shades of green) and γ_m=22 kN/m^3 (shades of red).

When a tensile strength is assumed, the slope and values of the curves obviously increase.

Furthermore, several curves suffer an expansion for different values of specific weight. For low *s/l* ratios (i.e. slender vaults) the estimation of the tensile strength represents a critical issue.

Increasing the *s/l* ratio (i.e. thick vaults), an increase of the collapse's acceleration is shown.

It is important to remember that, for thick vaults, the collapse condition can be achieved due to shear. For this reason, the proposed model must be applied in a consistent manner. In particular, when the curved elements are thick, the simplified model based on hinge mechanism, could provide unsafe results.

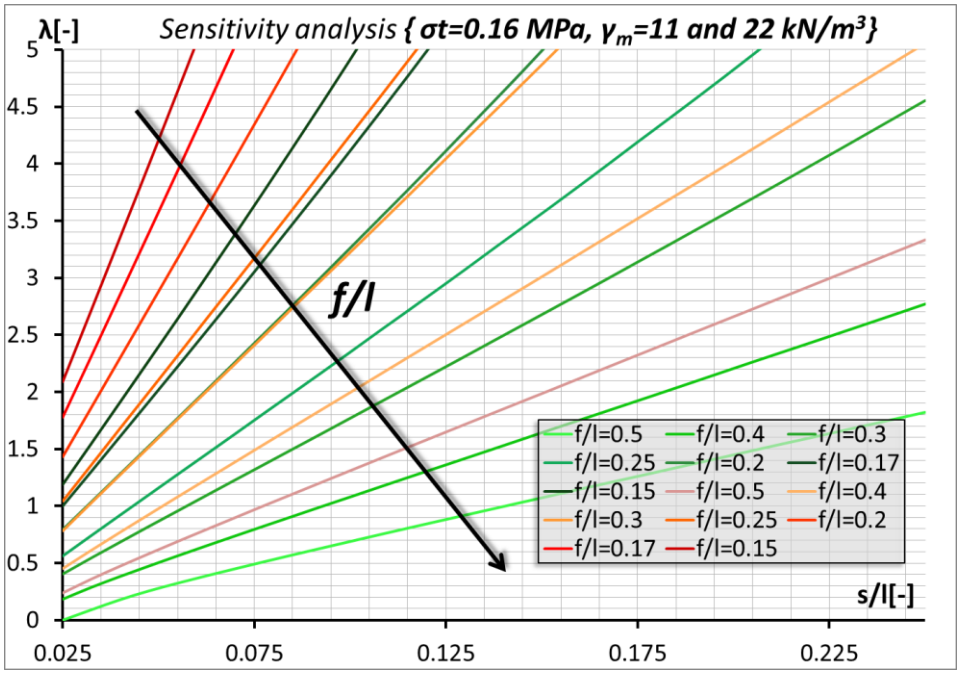

Figure 4.4: *Results of the sensitivity analysis: development of λ value with σ_t=0.16 MPa, γ_m=11 kN/m³ (shades of green) and γ_m=22 kN/m³ (shades of red).*

However, the model proposed is based on a hinge mechanism. In this case the specific weight shows an important effect on the structural capacity, which is not negligible.

Moreover, it is interesting to analyse figure 4.8 providing the development of the same collapse multipliers *λ*, while changing the *f/l* ratio and for discrete values of *s/l* ratios.

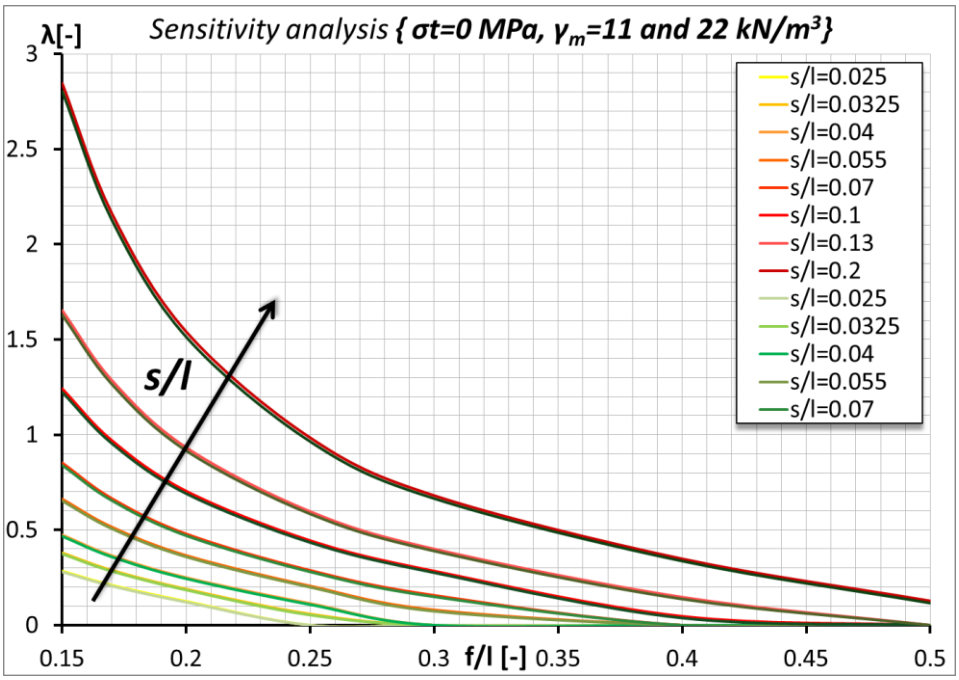

Figure 4.5: *Results of the sensitivity analysis: development of λ value with σ_t=0 kN/m^2, γ_m=11 kN/m^3 (shades of green) and γ_m=22 kN/m^3 (shades of red).*

The numerical results are shown for the extreme values of specific weight (11 and 22 kN/m^3, respectively) and under no-tensile strength assumption. The previous figure 4.8 shows again that the specific weight does not affect the structural capacity when no-tension is assumed.

Similarly, the previous graph is repeated in figure 4.9 for a tensile strength value of 0.16 MPa. As indicated above, a moderate value of tensile strength makes the numerical results highly sensitive.

The present section discussed the main aspects related to the analysis of slender masonry vaults (high ratios between span and thickness) and without any backfill.

The structural assessment according to the Heyman's Theory cannot be performed. In fact, when no-tensile strength is assumed, the collapse could be achieved already under gravity loads.

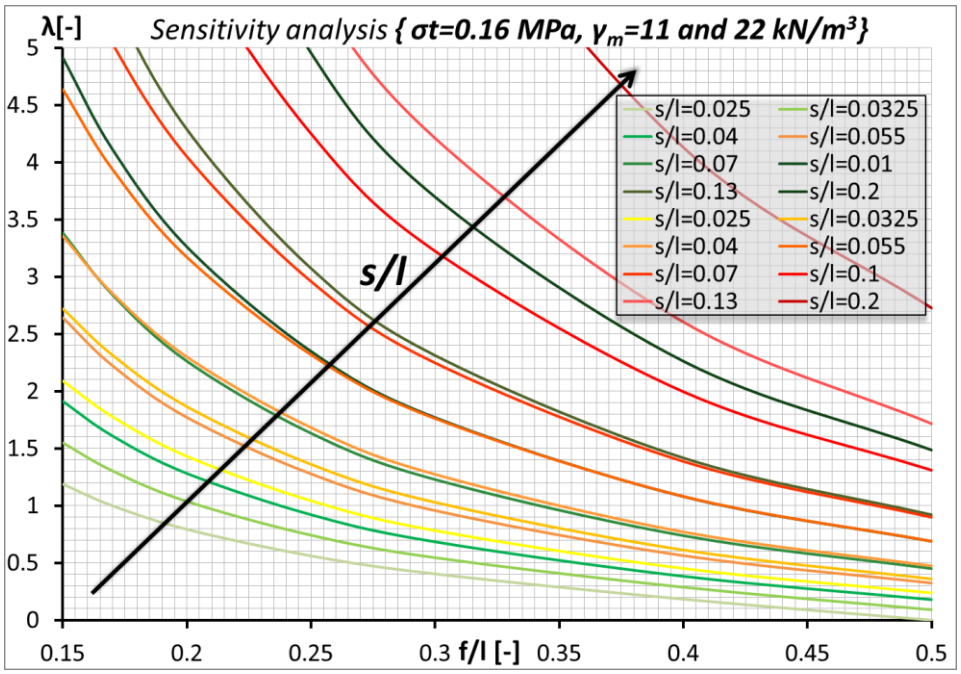

Figure 4.6: *Results of the sensitivity analysis: development of λ value with σ_t=0.16 MPa, γ_m=11 kN/m^3 (shades of green) and γ_m=22 kN/m^3 (shades of red).*

This is only a result of the theoretical modelling because real structures show no evidence of any structural problem. Theoretically, for these structures a tensile strength value should be assumed.

The results of the sensitivity analysis provide the impact of several parameters both geometrical and mechanical on the structural capacity.

In particular, under no-tension assumption, the influence of the typologies of masonry can be neglected.

Indeed, the model is sensitive to tensile strength of masonry and its impact on the seismic capacity was estimated for a large number of cases.

The results showed that a reliable estimation of the tensile strength is essential.

The number of elements used for the discretization has a reduced impact on the capacity assessment.

Therefore, the proposed method is valuable to estimate the ultimate capacity of the masonry vaults, by using a simplified approach.
The analytical method can also take into account different assumptions both geometrical (shape of the curved element and restraints) and mechanical (non-linear behaviour of the material like as cracking or plastic).
Finally, the proposed method represents a useful modelling tool in order to design dynamic tests on masonry vaults and to assess their vulnerability.

Chapter 5

DESIGN AND PLANNING OF A FULL-SCALE SHAKING TABLE TEST

Many of the masonry buildings are characterized by a complex architecture like as the religious buildings. Their structural behaviour is crucial, especially in high seismic risk areas. Historical and monumental buildings often showed low seismic performance, especially if they incorporate thrusting elements like as arches and vaults. In this field, numerical analyses and experimental tests provide important information about the structural behaviour of thrusting elements.

The structural behaviour can be complex to simulate and to predict exclusively by means of numerical analyses but experimental tests must be supported by numerical modelling.

The use of complex numerical models can be useless in the preliminary phase of an experimental program. Especially during the planning and design phases of the experimental tests the use of simplified models is valuable.

A masonry vault in solid facing clay bricks was tested by means of uniaxial dynamic tests on the shaking table. The vault characteristics are typical of churches built in Italy region. The vaults were tested by using several increasing signals in order to obtain an increasing damage level. After the damage occurred, the vault was strengthened and tested again.

In order to plan a dynamic test by means of a shaking table system, the signals and their intensities should be selected by using preliminary calculations.

The present Chapter focuses on the numerical simulations to design the dynamic tests.

5.1. State of art: experimental test of unreinforced and strengthened masonry vaults

Several experimental tests investigated the structural behaviour of masonry curved elements (vaults or arches). In some of them, also the structural performances of innovative building materials systems on masonry elements have been investigated.

Experimental tests on seven semi-circular brick arches which underwent strengthening by FRCM (Fibre Reinforced Cementitious Matrix) system have been shown in *Jasienko et al. (2009)*. The experimental results showed that in all the arches the use of FRCM strengthening significantly increases the load carrying capacity of the brick arches. The inorganic matrix ensured a good capacity for distribution of stresses on the masonry substrate.

Girardello et al. (2013) provided a further contribution on the study of FRCM strengthening applied to masonry arches. In such work the experimental tests were performed on a masonry curved element subjected to both monotonic and cyclic vertical asymmetric loads. The load was applied by means of hydraulic jacks at 1/4 of their span. The experimental results showed that this strengthening system increases the load capacity and the ductility of the masonry arch. Furthermore, the dynamic identification performed on the specimen showed the decay of the natural frequencies with achieved damage.

Briccoli Bati et al. (2007) conducted a comparison between the experimental performances of FRP (Fibre Reinforced Polymers) strips and FRCM system applied on two masonry arches. The specimens were strengthened by two different technologies. The first specimen has been strengthened with CFRP (Carbon Fibre Reinforced Polymers). The second specimen has been strengthened with FRCM system by means of glass fibres. The experimental results showed that, under cyclic loads, the specimen strengthened with the FRCM system performed better. Furthermore, the use of FRCM strengthening does not radically change the

structural behaviour in collapse condition (the failure mechanism is similar to the unreinforced specimen).

Calderini et al. (2014) reported an experimental study on the seismic behaviour of arch-pier system strengthened with tie-rods. An innovative tie-rod characterized by a stiffness lower than traditional ones has been developed. The experimental test was performed by adopting the inclined plane static test on a scaled model. The experimental results showed that larger tie-rod deformability yields to larger displacement capacity at collapse.

In these papers the masonry curved elements were usually subjected to monotonically or cyclic pseudo-static load. Such testing methods, nowadays widely adopted could not be always able to realistically simulate the seismic behaviour of the specimen.

Furthermore, the pseudo-static forces are usually applied by means of hydraulic jacks which often generate a sliding failure at the locations where the load devices are applied *[Garmendia et al. 2011]*.

While the concentred loads are applied, the loading devices could restrain the strengthening system on the substrate, jeopardizing the results. Furthermore, the same pointwise load could prematurely damage the strengthening system. Such critical aspects could lead to an inaccurate interpretation of the seismic behaviour of the strengthened structure. Indeed, it is well known that masonry curved elements are usually prone to the flexural failure by means of the hinge mechanism activation and the sliding failure is often neglected in the majority of cases *[Heyman 1995]*.

In this background, shaking table tests are able to simulate realistically the seismic effects on many structures. These dynamic tests allow an actual assessment of the seismic performances of different strengthening systems. Nevertheless, dynamic tests both on unreinforced and strengthened masonry vaults by means of shaking table system are lacking in the scientific literature.

Giamundo et al. (2015) conducted a study aimed to the assessment of the structural performances of inorganic matrix grid applied on a masonry vault. Several shaking table tests, before and after the TRM (Textile Reinforced Mortar) strengthening system, have been performed. The experimental results showed that this strengthening technique greatly increased the seismic capacity and the ductility of the repaired masonry vault.

In the present Section, several dynamic tests on masonry vaults with abutments typical of roofs in religious buildings have been designed.

The present study is aimed to the assessment of the structural performances of TRM (Textile Reinforced Mortar) strengthening combined with other traditional strengthening systems (masonry rib and unidirectional steel tie). The structural assessment of strengthening system has been conducted by means of comparison between the performance detected on the unreinforced and strengthened specimens. The experimental results have been supported by preliminary calculations. Numerical models based on FEM approaches and on simplified analytical modelling have been considered *[Bertolesi et al. 2016, Portioli et al. 2015, Tabbakhha et al. 2016, Parisi et al. 2016 & Noor-E-Khuda 2016b]*.

5.1.1. Efficiency and compatibility of innovative building materials on masonry buildings

Over the years, innovative materials and technologies have been developed to limit the effect of earthquakes on the structures. The use of composite materials has shown to be effective for these structures.

Most of the European cultural heritage buildings are made of masonry. Furthermore, in almost all heritage buildings there are masonry vaults which represent a critical structural part in regard to the assessment of the seismic behaviour. In particular, vaulted structures incorrectly designed could promote a deleterious behaviour of the entire buildings.

The increase of stress level provided by the thrusting elements during the seismic events, could not be compatible with the performances of material, in traction in particular.

This is a critical issue especially for masonry vaults without any backfill. Such load condition is typically present in vaulted roofs adopted in the historical religious buildings.

Therefore, improving the knowledge both on masonry vaults and on strengthening systems, meets the need to safeguard the existing masonry buildings against the earthquake effects.

In this background, the experimental tests can provide an efficient contribution to the interpretation of the strengthening effects.

The use of innovative materials, aimed to the strengthening of masonry elements, has shown to be efficient *[Valluzzi et al. 2001, 2002, Roca et al. 2010, D'Ambrisi et al. 2013a, Angelillo et al. 2014, Giamundo et al. 2015 & Wang et al. 2016]*.

However, some specific innovative materials are often not compatible with the heterogeneity of the masonry and building techniques. Indeed, the use of FRP laminates or fabric, has shown some crucial aspects as well as disadvantages *[Lignola et al. 2012]*.

The key issue of the strengthening system based on organic matrix (i.e. FRP), is the deficiency of bond and compatibility between organic resin matrix and masonry substrates. Additionally, the organic matrix has both low vapour permeability and insufficient performances at high temperature (flammable material).

Furthermore, the interventions by FRP systems are quite irreversible and could be in some cases architecturally invasive.

The previous issues can be overcome by using strengthening systems based on inorganic matrices also indicated by FRCM acronym. This strengthening technique is made by embedding several reinforced fibres (strips or grids) in an inorganic matrix.

In this way, comparing to the traditional FRP technique, the mortar matrix replaces the epoxy resin matrix (organic). The advantages which involve the use of inorganic matrix are well known in the scientific literature *[Prota et al. 2006, Papanicolaou et al. 2007, 2008, Lignola et al. 2009, Parisi et al. 2011, D'Ambrisi et al. 2013b, 2014, Carozzi et al. 2014 & Giamundo et al. 2015]*.

The physical and chemical compatibility of the matrix material with the masonry substrate provides an improvement of the bond between the strengthening system and masonry substrate. Additionally, the FRCM system is simple to install on curved surfaces also and it is fully reversible. It can be easily removed like as a plaster from the structural elements without causing damage.

Furthermore, the premature debonding failure is prevented by using the spread grid element compared to the traditional unidirectional fibres in localized strips.

The structural assessment of masonry vaults strengthened by inorganic matrix technique is a fundamental topic. The experimental results presented in this Ph.D. thesis provide a contribution to the knowledge on innovative techniques, aimed to the strengthening of the masonry curved elements with abutments.

5.2. Experimental test of a full-scale masonry vault

Several dynamic tests with a shaking tables system were performed on a full scale clay brick masonry vault with abutments.

The experimental program was carried out in two parts in order to assess the performances of the strengthening system.

The dynamic tests were performed before on the unreinforced specimen up to failure and after on the specimen partially rebuilt and strengthened by means of the TRM strengthening combined to mortar joint repointing and

grout injections and other additional strengthening interventions. A detailed description of the specimen is provided in the following subsections.

5.2.1. Description of the unreinforced specimen

The entire masonry structure was made of solid facing clay bricks (25×5.5×12) cm^3. The joints were made of pozzolana-based mortar with a thickness equal to 1 cm.

The geometry of the vault is characterized by a segmental arch profile with span and rise equal to 298 cm and 114 cm, respectively.

The specimen has a different depth for the base (constraint on the shaking table setup) and curved elements which are 220cm and 116cm, respectively.

The segmental arch profile replicates the vault tested by *Giamundo et al. (2015)* and is less than a semicircle, but its imposts are located over two abutments 103 cm in height (figure 5.1, maximum allowable height according to laboratory constraints).

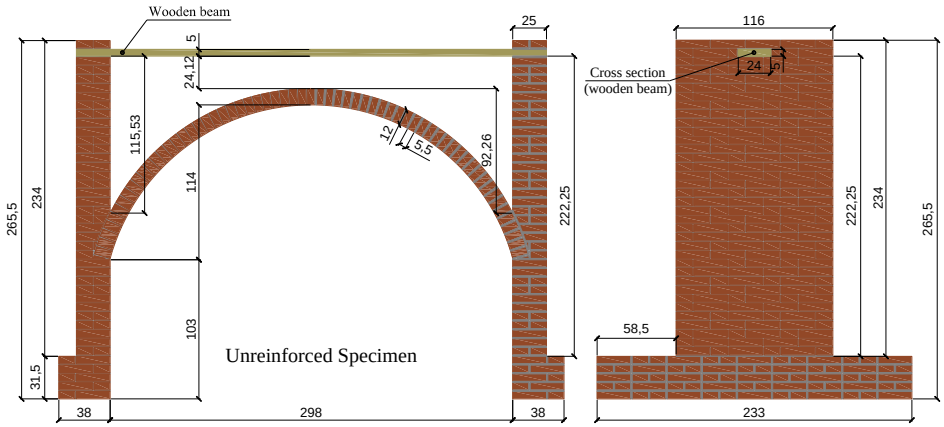

Figure 5.1: *Unreinforced specimen geometry*

According to typical historical buildings, the lateral masonry abutments have been raised over the imposts up to 234cm, also due to laboratory constraints.

In some traditional masonry vaults the backfill is present, and it provides multiple effects on the seismic performance of the vaults. On one hand it causes an increase of the horizontal thrust; on the other hand it distributes the external loads and produces an increase of the normal stresses. The first aspect can induce a deleterious effect on seismic performance of the vault. However, this issue can be solved by means of structural measures (i.e. steel ties). In this way, the negative effects of using a backfill can be eliminated and the second beneficial aspect is certainly emphasized. However, the backfill is not present generally in the roofs of churches (figure 5.2).

Figure 5.2: *San Biagio D'Amiterno Church, L'Aquila (Italy), damages after 2009-Earthquake.*

This work focused on this vault typology. For that reason the specimens (strengthened and unreinforced vault) have been tested without any backfill. The material characterization was performed for the mortar and bricks. Both the compressive and tensile strengths were assessed according to the technical codes *[UNI EN 998-2, 2010 & UNI EN 1015-11, 2007]*. The mechanical characterization was performed on twelve masonry specimens with a dimension of (40×40×160) mm^3. The specimens were tested at an

age of 28 days, after the hydration process. Instead, the Young's modulus was assessed according to *UNI 6556 (1979).*

The mechanical properties of clay bricks were assessed by means of several tests according to *UNI 11128 (2004), EN 772-1 (2002) and UNI 8942-3 (1986)*. In particular, compression and splitting tensile strength tests have been conducted. Finally, several three points bending tests have been performed. The measured properties of materials are shown in table 5.1.

Table 5.1: *Mechanical characterization results.*

Property	Brick	Mortar
Compressive strength [MPa]	19.8	10.1
Flexural strength [MPa]	3.7	-
Splitting tensile strength [MPa]	2.5	-
Tensile strength [MPa]	-	2.4
Young's modulus [Mpa]	5756	1452
Specific weight [kN/m^3]	16	18

5.2.2. Description of the strengthened specimen

The masonry curved element and the masonry abutments have the same geometry for both specimens. Because it partially collapsed after the first dynamic tests, the vault has been partially rebuilt. Indeed, the collapse condition was achieved by means of the hinge mechanism. In addition, other interventions, by using different strengthening systems, have been performed.

Interventions by means of repointing of the cracked joints and grout injections were performed in the abutments. It is assumed that this strengthening technique has restored the masonry to the undamaged condition. It has been performed both at the bases of the structure where the activation of the plastic hinges occurred (figure 5.3) and on the entire abutments (figure 5.4).

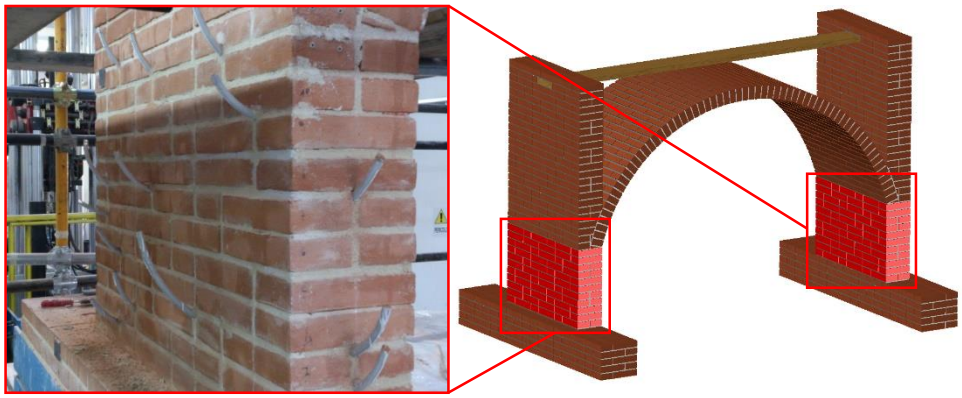

Figure 5.3: *Repointing of the cracked joints and grout injections system on the abutments (lower portion).*

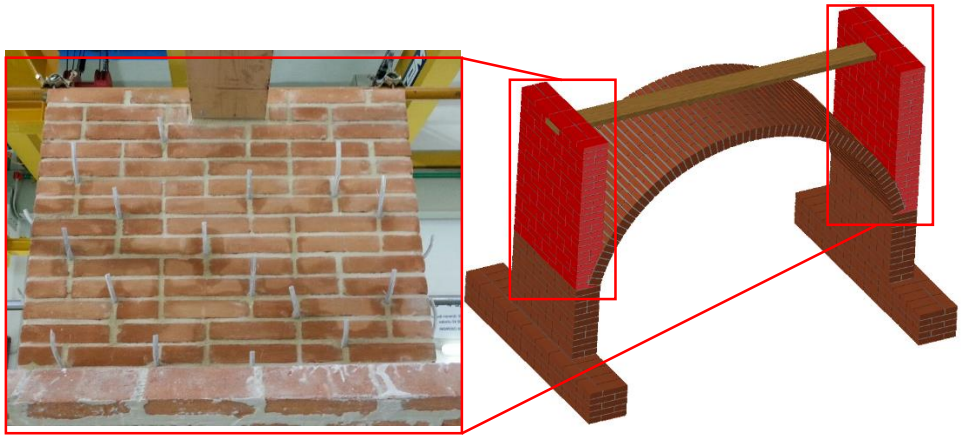

Figure 5.4: *Repointing of the cracked joints and grout injections system on the abutments (higher portion).*

The former interventions have been performed by means of a repair mortar, commercially available. The grout injections system has been performed by means of several suitably spaced holes. The grout injection is a critical aspect, since no wide cracks are present. For that reason a mixture based on cement-free fluid hydraulic binder has been used for the injections.

The TRM application aimed to improve the seismic performance of the masonry curved elements.

Indeed, this strengthening system has been applied at the extrados of the curved element. It was made by a first mortar layer 0.5 cm thick applied to the masonry substrate (extrados of the curved element).
Over the mortar layer an alkali-resistant primed fibre grid has been placed. The grid is made of basalt fibres with weight of 250g/m^3. The grid layers were overlapped to cover the entire depth of the arch profile. Finally, a second mortar layer, entirely covering the basalt grid was built (figure 5.5).

Figure 5.5: *TRM strengthening applied on the extrados of the masonry curved element.*

For both the mortar layers a bi-component premixed mortar has been used. This mixture is made of natural hydraulic lime (NHL), several special additives, natural sand and synthetic polymers. The entire mixture is worked in aqueous dispersion according to the manufacturer.
At the extrados, close to vault's imposts only, two backfills have been made by means of structural mortar (previously used) mixed with expanded clay aggregates (15% in volume).
The entire depth of the masonry vault (116 cm) was involved, raising up to 41cm in height. In addition, a masonry rib was built over the extrados, in the middle of the curved element. In particular, the masonry was made of

clay hollow bricks (25×25×25) cm^3 and pozzolana-based mortar joints with a thickness of 1 cm.

The masonry rib was built by using a single row of bricks and has been raised up to 55cm in height over the backfill, reaching the crown of the vault (figure 5.6).

Figure 5.6: *Masonry rib made of single row of bricks.*

Finally, an innovative steel tie was built over the masonry rib. This last strengthening system was made of unidirectional steel fibres usually characterized by very low prestress, given without a specific device. In fact, a prestress manually provided is already sufficient. It was demonstrated that prestress of tie systems barely influences the seismic performance *[Calderini et al. 2014]*.

The steel tie is located at a height approximately corresponding to the crown of the masonry vault (figure 5.7).

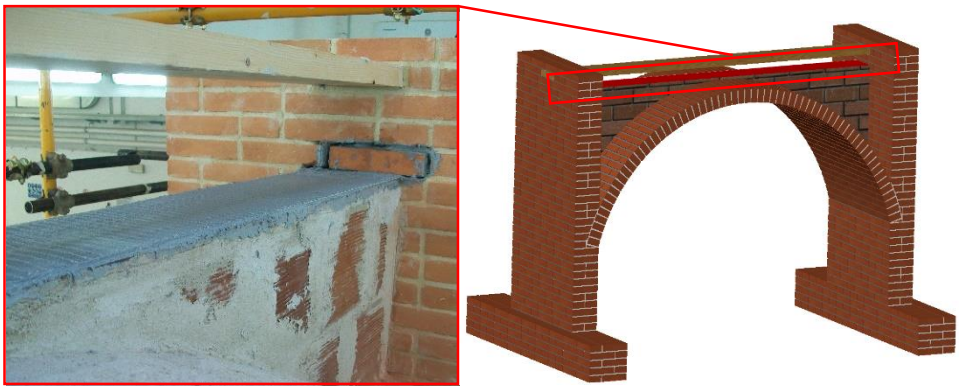

Figure 5.7: *Innovative steel tie built over the masonry rib.*

The steel tie was perfectly bonded to the lateral masonry abutments by means of two steel devices (figure 5.8a). This system was made of steel elements with an appropriate L shape.

Each end of the tie element was constrained by using two coupled steel angles. The tie element was applied inside the steel devices by means of a mortar layers. The mortar mixture used in order to cover the tie element has been the same used in the strengthening intervention (NHL-based).

In conclusion, an epoxy grout injection (figure 5.8b) was performed on several contact surfaces (steel and masonry).

Figure 5.8: *b) steel angles and c) epoxy grout injection.*

In order to avoid a debonding failure between the masonry rib and the extrados of the vault, an additional basalt fibre grid has been applied (figure 5.9a).

In this way the connection between masonry rib and substrate is guaranteed by an additional TRM system. The entire surface (masonry rib and additional TRM strengthening) was covered by two mortar layers of about 1 cm total thickness (figure 5.9b). The mixture used is the same (NHL-based).

Figure 5.9: *b) Additional TRM strengthening and b) its covering.*

Further details about the geometrical characteristics of the strengthened specimen are provided in figure 5.10.

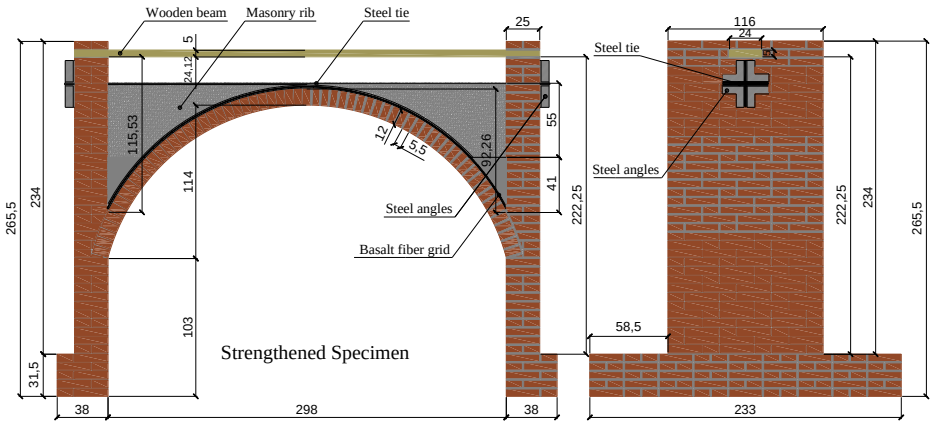

Figure 5.10: *Strengthened specimen geometry.*

Preliminary mechanical characterisation tests have not been performed for the materials used in strengthening systems. In particular, the mechanical parameters were provided by manufacturer (technical data-sheets).
The physical and mechanical properties of strengthening materials are reported in table 5.2.

Table 5.2: *Materials properties of strengthening systems.*

Property	Grid	Mortar	Hallow brick	Steel tie	Epoxy grout
Compressive strength [MPa]	-	≥15	>5	-	>70
Tensile strength [kN/m; N/mm^{2*}]	≥60	-	-	>2.845*	-
Shear strength [MPa]	-	≥0.15	-	-	>10
Young's modulus [Mpa]	89000	10000	-	210000	6000
Specific weight [kN/m^3; kN/m^{2*}]	2.45*	-	6.23	0.077	16.68

Both the specimens were built on a stiff steel beams system. It ensures that the interaction between specimen and steel beam system is negligible. The masonry specimens were constrained on the shaking table by means of the steel structure. Indeed, allowing pier differential displacements could lead to premature damages of the vault due to pier failure.

5.3. Preliminary calculation: seismic capacity assessment and dynamic behaviour investigation

The success of any experimental test depends on its preliminary design. For dynamic tests the selection both of signals (i.e. frequency content and time history) and their intensity (i.e. maximum acceleration value) represents a critical aspect.

Analytical and numerical models in order to predict the structural behaviour certainly represent valid tools in order to design an experimental test using the shaking table system.

However, according to a preliminary design of the experimental program, when for instance there is still uncertainty on mechanical properties, amongst others, the use of complex numerical models may be problematic and ineffective.

Nearly the totality of engineering applications, aimed at assessing the seismic capacity of masonry structures, is conducted under no-tension assumption. For masonry arches the Heyman's approach *[Heyman 1995]* is commonly adopted. No-tensile strength and infinite compressive strength are the main assumptions used in Heyman's theory, along with no sliding. At collapse, the compressive stresses are typically lower than the compressive strength. The normal stresses could achieve high values only in localized section (localized portions between brick and mortar due to cracking effects).

In predictive models the hinge mechanism is the only considered failure mode, as supported by experimental evidence. Indeed, other failure modes

(sliding failure and crushing failure) are uncommon.

According to the Heyman's theory (i.e. limit analysis), for a generic load pattern, the resultant's envelope of the acting compressive stress distribution (thrust line) must be contained entirely within the boundaries of structure *[Lignola et al. 2008, Angelillo et al. 2013 & Fortunato et al. 2014]*.

Each element is able to carry the load by means of compressive stress exclusively. According to the lower bound theorem, any thrust line which is placed within the vault's boundaries, corresponds to an equilibrium configuration of the curved element *[Angelillo et al. 2004]*.

The equilibrium of the masonry vault is satisfied under a generic load (vertical and horizontal), if a thrust line entirely contained in the vault's boundaries can be found.

With a rectangular cross section, assuming s the thickness and P the normal force acting on the cross section, the maximum eccentricity $e(P)$ of the thrust line according to no-tension assumption in cracked condition is equal to $s/2$ and $-s/2$ for a zero axial load.

The eccentricity value is reduced at increasing axial load P. The collapse of the masonry vault can be achieved, if there are a sufficient contact points between the thrust line and arch boundaries to generate a hinge mechanism. In fact, each contact point represents the formation of a hinge (with the opening on the side opposite to the contact point).

The previous analytical model for particular cases could provide inaccurate solutions (see paragraph 2.4.1).

Masonry vaults characterised by both a high span/thickness ratios (slender vaults) and without any backfill, cannot be analysed with the Heyman's model.

For these structures without a minimum of tensile strength, even under a gravity self-weight load, the plastic compatibility condition may be violated. It's an issue due to the very low axial stress values and consequently, the eccentricities due to permanent gravity loads could not be

properly counteracted. Therefore, in order to assess the structural behaviour of the masonry vaults, a minimum value of tensile strength is necessary in the analysis.

5.3.1. Seismic capacity assessment of the unreinforced vault

For the unreinforced specimen an analytical model taking into account a tensile strength has been used *[Ramaglia et al. 2016]*.
The collapse is achieved when the thrust line reaches the maximum eccentricity in an adequate number of points. The maximum eccentricity *e(P)* depends both on behaviour of material (elastic, cracking or plastic) and on the achieved axial load *P*.
Furthermore, according to the tensile strength assumption, the maximum eccentricity of the thrust line is certainly greater compared to the classical approach, where no-tension is assumed. The boundaries containing the thrust line have an evolution with the load history *[Ramaglia et al. 2015]*.
The unreinforced specimen has been analysed by means of the proposed analytical model (see Chapter 3).
Several non-linear analyses (fixed gravity load and variable monotonically increasing horizontal loads) have been performed in order to provide both a reliable PGA (Peak Ground Acceleration) value and the hinge locations at collapse (evolution of the failure mode).
In figure 5.11 the mechanical model used for the structural analyses is shown, where the curved element is discretized into a composition of beam elements. The abutments have been supposed fixed at their bases.
During the entire analysis, a fixed vertical load pattern (gravity load) has been considered. The internal stress variation is due to the increasing of the horizontal load pattern, by means of a monotonically increasing acceleration.

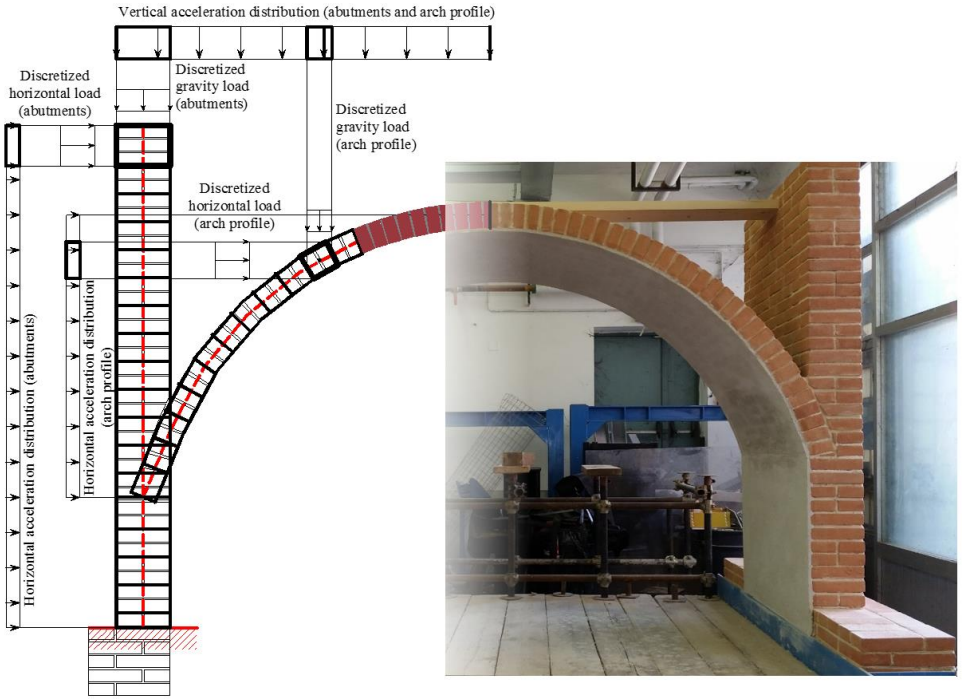

Figure 5.11: *Mechanical model of the unreinforced vault under a vertical and horizontal load pattern.*

The horizontal load increase is proportional to the masses of the masonry vault. Both the vertical and horizontal loads have been modelled by means of a discrete approach.

The masonry material has been modelled using a homogeneous material with tensile strength. In table 5.3 the average mechanical properties of the homogeneous material (masonry), used in the preliminary analysis, are shown.

Table 5.3: *Mechanical characterization results.*

Mechanical Parameter	Value		
Young's modulus [MPa]	1200	1500	1800
Compressive strength [MPa]	2.4	3.2	4
Tensile strength [MPa]	0.08	0.16 (experimental value)	0.32

The tensile strength value (middle value provided in table 5.3) is the same previously estimated on the similar specimen tested in the laboratory of the University of Naples, Federico II (see paragraph 4.3.1).

In table 5.3, both the Young's modulus and compressive strength are the values provided by the Italian Building Code 2009 for similar typological masonries.

The experimental estimation of the mechanical properties was limited to the tensile strength only.

The compressive strength has almost no effect on the seismic capacity of the specimen. In fact, the maximum compressive stresses are usually much lower than the compressive strength.

The Young's modulus has an important role both for the internal stress distribution and for the deformability of the vault. However, preliminary calculations showed the negligible influence both of the compressive strength and of the Young's modulus on the ultimate seismic capacity of the specimen.

No effect on the global behaviour has been shown by the wooden beam because it had not a sufficient bonded length and any anchoring device. Hence, this element has not been modelled in the numerical model.

In the case of unreinforced specimen the analytical model provides both the collapse's acceleration (2.26 m/s^2 -i.e. 0.23g- with a tensile strength of 0.16 MPa) and the resulting hinge mechanism (i.e. four hinges activated) as shown in figure 5.12.

Similarly in the following figures, other graphical representations of the numerical results are provided for this specimen.

The method and the average values of mechanical parameters were the same because the vaults were similar in terms of materials.

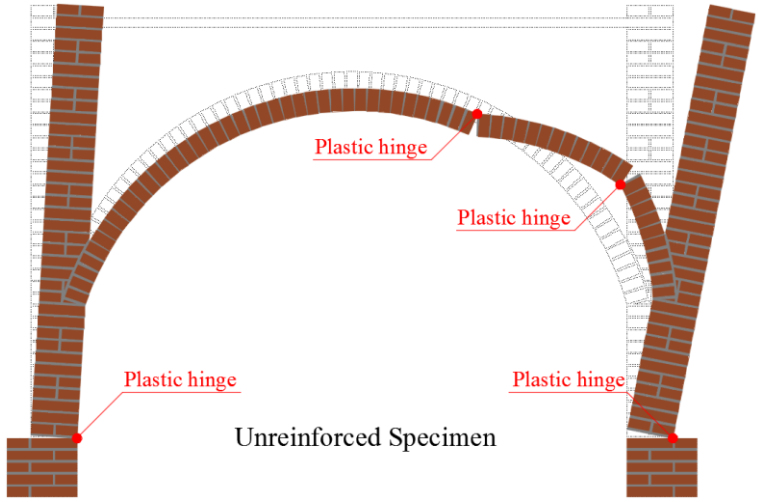

Figure 5.12: *Hinge mechanism activated for the unreinforced specimen.*

The arch and walls were divided into 68 elements according to the specimen geometry. The curved portion was discretized in the same number of elements as previous case, while the walls were divided into two elements only, because potential locations for hinges were at their ends. However, increasing the number of elements in the lateral walls yields to the same results.

A uniform horizontal load was assumed involving both walls and curved portion (i.e. the arch). Figure 5.13 shows the configuration of the thrust line at collapse condition for the curved element only.

The internal forces M_j, P_j reach the plastic surface in two points only, representing the hinges 2 and 4 formation on the arch (figure 5.14).

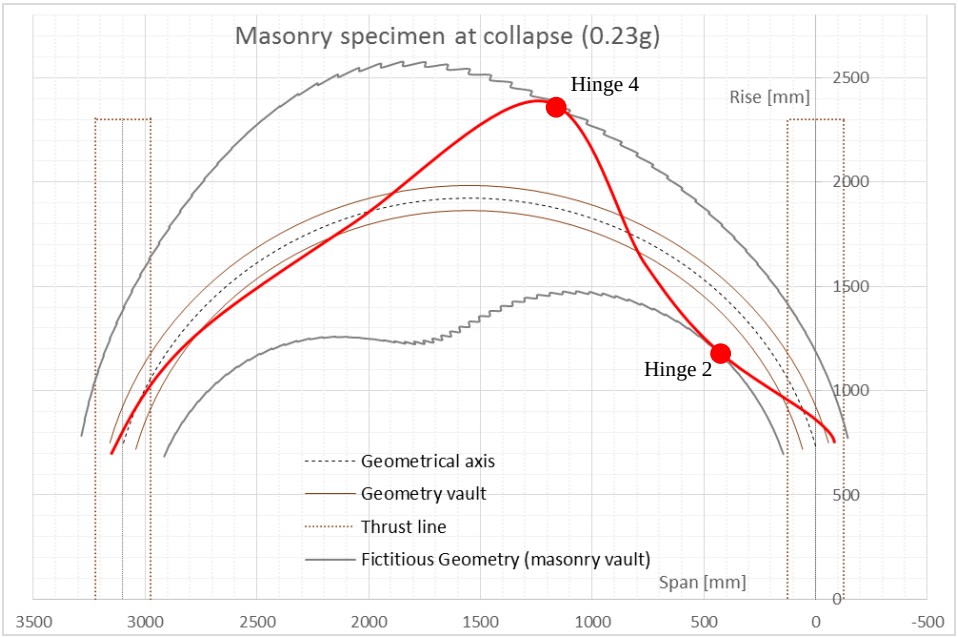

Figure 5.13: *Theoretical thrust line configuration for the masonry specimen (hinge mechanism activated).*

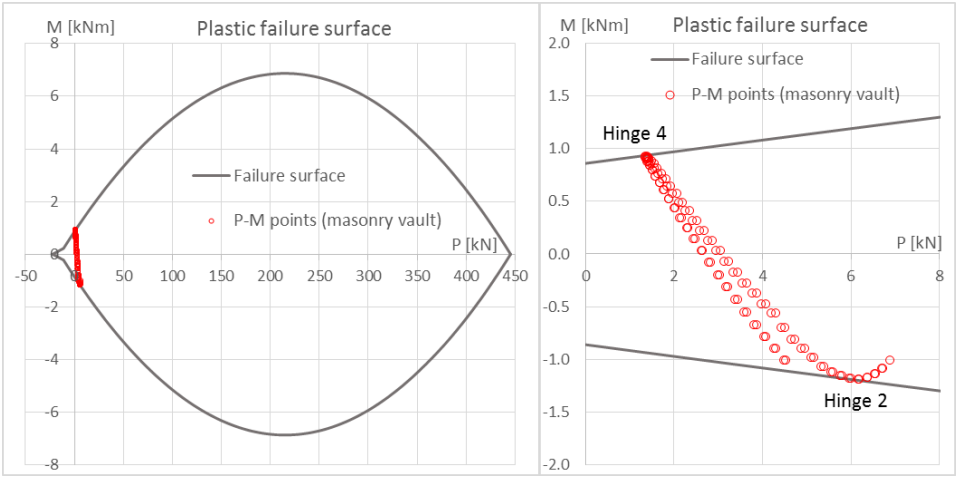

Figure 5.14: *P-M points in the plastic failure surface (curved element).*

Conversely, the figure 5.15 provides the thrust line configuration for the lateral masonry walls at the same load.

It is worth noting that due to very low axial load values, the maximum eccentricity provided by equations (3.26) and (3.63) achieves extremely high values, especially at the top of the walls. On the other hand, at the intersection of the arch with the walls, the concentrated force due to the arch yields to a prompt increase of the axial load, hence a reduction of the fictitious thickness in the lower portion of the walls.

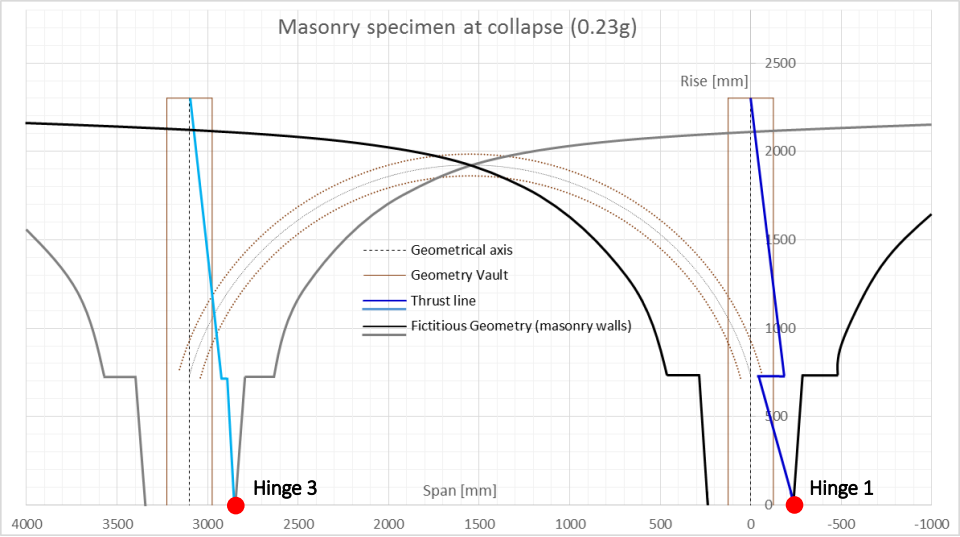

Figure 5.15: *Theoretical thrust line configuration for the masonry specimen (hinge mechanism activated).*

The internal forces M_j, P_j reach the plastic surface at the bases only, representing the hinges 1 and 3 formation at the bases of the lateral walls (figure 5.16).

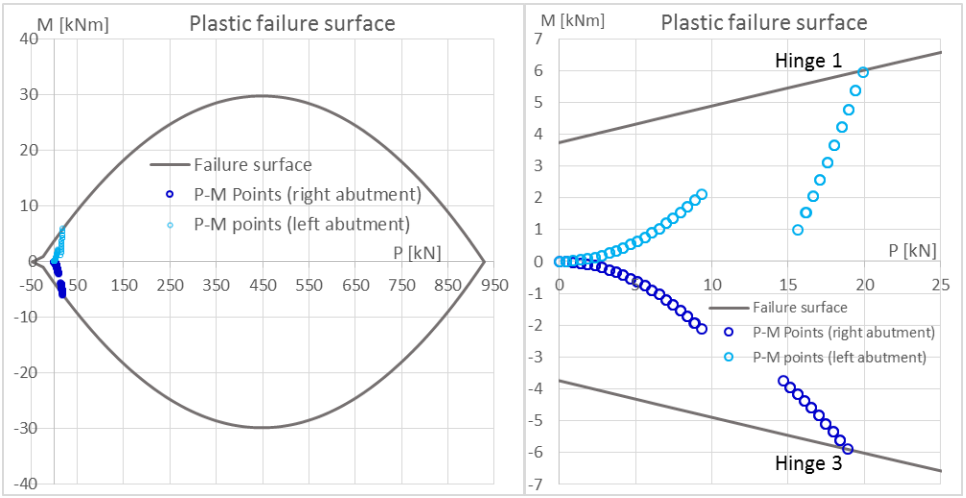

Figure 5.16: *P-M points in the plastic failure surface (curved element).*

The tying at the wood truss location was not included in the model because, as expected, wood truss was free to slip during the experimental shakings. The cracks occurred at almost symmetrical locations at the inversion of the shaking direction.

5.3.2. Seismic capacity assessment of the strengthened vault

A similar approach has been performed for the specimen where several strengthening techniques have been combined.

The assessment of the actual effects of several interventions is not simple, especially in a preliminary analysis. The several strengthening systems involve multiple effects on the global structural behaviour. The several interventions have been performed in order to improve both the seismic capacity and the dynamic behaviour of the specimen.

The curved masonry elements and portions adjacent to the lateral abutments are certainly most interested by the interventions.

In this background the masonry abutments are the most vulnerable elements (especially at the base). The arch element by means of the several strengthening techniques achieves an extremely high stiffness.

For this reason, in a preliminary calculation, the structural elements localized above the level of the vault's imposts have been modelled as a rigid block (figure 5.17).

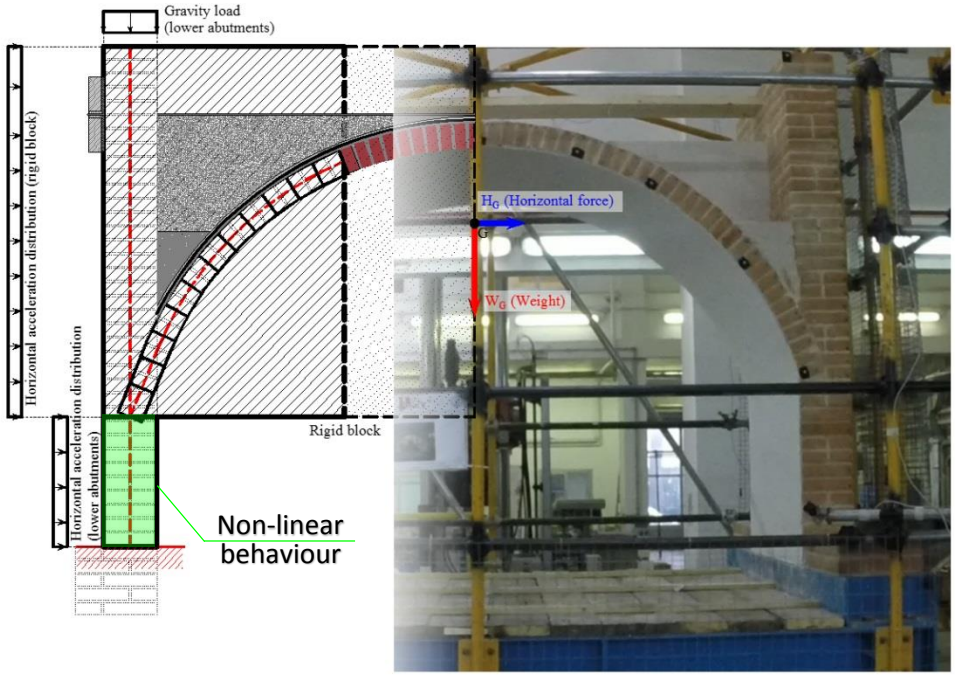

Figure 5.17: *Mechanical model of the strengthened vault under a vertical and horizontal load pattern.*

The resultant of the seismic actions can be applied in the centre of gravity of the rigid block.

The structural model for the strengthened specimen is very simple. In particular the non-linear effect (i.e. plastic behaviour) was considered for the lower portion of the abutments only (figure 5.17). In fact, the plastic hinges activated according to the figure 5.18.

It provides both a reliable collapse acceleration and the collapse configuration.

The collapse mechanism, due to the strengthening techniques adopted, is localized in the lower portion of the masonry abutments. In particular the

hinge mechanism is achieved formerly at the base of each abutment (first plastic hinges) and later at the vault's imposts (two additional plastic hinges).

The use of the predictive model provides a collapse's acceleration of 4.9 m/s^2 (i.e. 0.5 g) with a tensile strength of 0.16 MPa. The hinge mechanism in figure 5.18 is shown for the strengthened specimen.

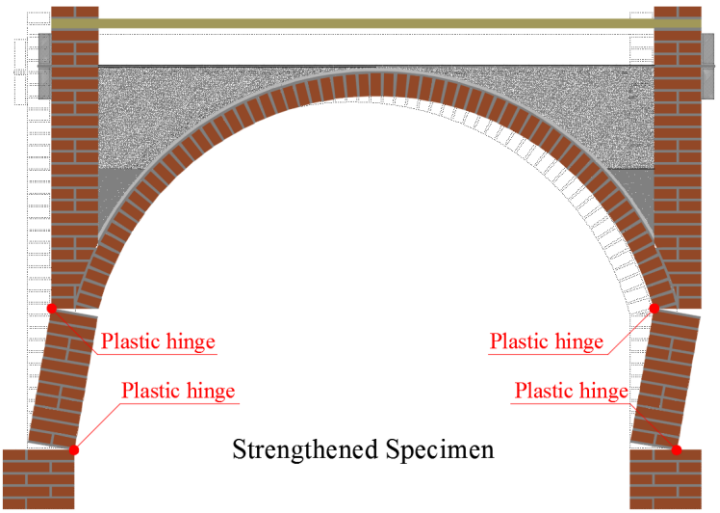

Figure 5.18: *Mechanical model of the strengthened vault under a vertical and horizontal load pattern*

5.3.2.1. Effects of the strengthening systems on the seismic capacity

The collapse mechanism assumed is due to the strengthening systems made on masonry specimen.

The masonry rib has increased arch stiffness. For this reason the vulnerabilities moves from the curved element to the masonry abutments.

It is interesting to note that the additional systems: unidirectional steel tie and TRM system, provide a certainly increase of this effect.

In order to assess the impact of masonry rib (elastic properties) on the strengthening efficiency, several sensitivity analyses have been performed.

The sensitivity analysis have been performed using a numerical FEM model (figure 5.19) where:

- The masonry rib has been modelled with linear-elastic shells;
- The masonry arch and lateral abutments have been modelled thought beam elements;
- The covering made of TRM has an impact on the failure surface. In particular the failure surface has an expansion on the side where the TRM is effective. When the TRM system is applied at extrados of the curved element, it provides an expansion of the failure surface towards the negative bending moments. For this reason the TRM system has been modelled by means of an enlargement of the failure domain *P-M [Ramaglia et al. 2015]*.
- Finally, the steel tie has been modelled using a beam element not reacting in compression and constrained on the extrados of the masonry rib.

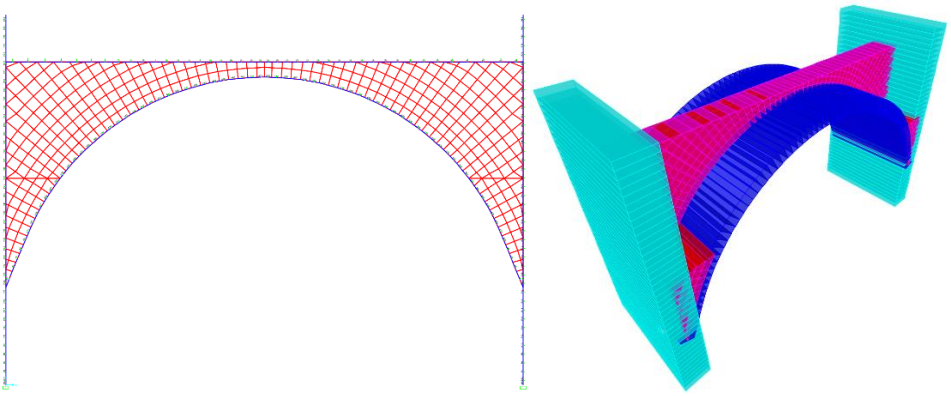

Figure 5.19: *FEM model in order to assess the influence of masonry rib on the seismic behaviour.*

The sensitivity analysis have been performed on two FEM models.

In particular, first model (namely FEM_M_1) has been modelled without both the unidirectional steel tie and the TRM system. Therefore, this model takes into account only the impact of masonry rib on the seismic behaviour. Second FEM model (namely FEM_M_2) was developed in order to assess the effect of two additionally strengthening systems (i.e. steel tie and TRM system) on the seismic response.

For each numerical model, push-over analyses have been performed varying both the geometrical (thickness s_{abut} and height of the abutments h_{abut}) and the mechanical properties (Young's modulus E_{rib} of masonry rib). The non-linear effects have been modelled for the beam elements only. Therefore, the plastic hinges can be achieved only on the arch element or on the masonry abutments (figure 5.20).

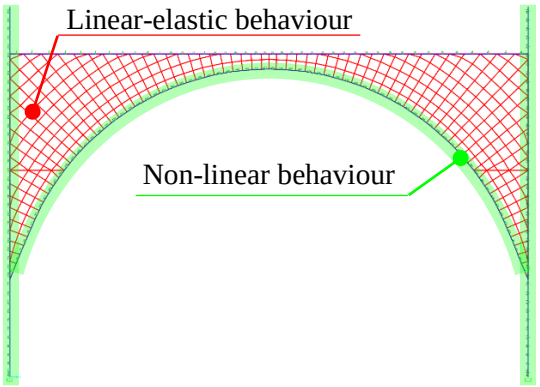

Figure 5.20: *Identification of the elements where the plastic hinges may occur (FEM_M_1 or FEM_M_2).*

The Young's modulus E_{rib} of the masonry rib was changed from a minimum value of 1200 MPa according to the Italian Building Code (IBC, 2009) to a higher value (compatible with the typology of masonry).

In particular, the elastic modulus was increased in order to achieve a failure according to the mechanism shown in figure 5.18 (i.e. the vulnerability moves from the arch element to the masonry abutments).

In order to assess the influence of other geometrical and mechanical parameters, the elastic modulus variation (E_{rib}) has been coupled to the geometrical parameters (s_{abut}, h_{abut}).

Starting from the geometry of the tested vault (figure 5.10), the thickness of masonry abutments s_{abut} and their height h_{abut} have been changed. In particular, the abutments thickness s_{abut} ranged from 0.25m to 1m. Instead, the height of lateral abutments ranged from a value of 0.5m to 5m.

Next section shows the results of these parametric analyses. In particular, the figure 5.21 shows the development of the E_{rib} value (that provides a collapse mechanism according to the figure 5.18) varying the parameter h_{abut} for a tensile strength value of 0.16 MPa. In the following section only the results for a thickness abutment of 0.25 m will be discussed.

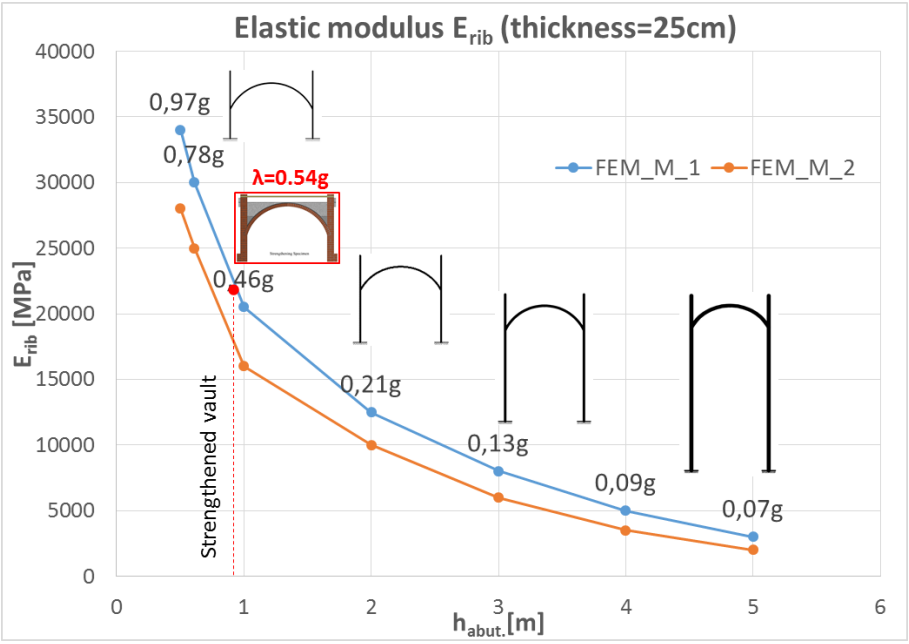

Figure 5.21: *Developing of Young's modulus E_{rib} in order to achieve a failure mode according to figure 5.18 (FEM_M_1 or FEM_M_2).*

It is interesting to note that the additional systems (unidirectional tie and TRM system) provide a beneficial effect on the seismic behaviour.

In particular, without the tie and TRM strengthening systems, the value of E_{rib} with reference to the first model (FEM_M_1) that guarantees the supposed failure mode (figure 5.18) is higher than the E_{rib} with reference to the second numerical model (FEM_M_2) where the additional strengthening systems are not included.
Furthermore, figure 5.21 shows the impact of the parameter E_{rib} varying h_{abut}. In particular, it is noted that for high values of h_{abut} the influence of the E_{rib} can be neglected. In fact, when the masonry abutments are slender (i.e. high h_{abut}/s_{abut} ratio) the interventions made on the curved element show a negligible impact on the global behaviour (full system made of arch element and abutments). This issue is due to the strong vulnerability that show the masonry abutments with high ratio of h_{abut}/s_{abut}.
Therefore, the numerical results show that the additional strengthening systems provide an important beneficial effect on the seismic behaviour. In fact, without the additional systems, the collapse mechanism shown in figure 5.18 may not occur. However, it could be solved by using a masonry rib with higher thickness s_{rib} or, alternatively, reducing the spacing between the masonry ribs.

5.3.3. Dynamic investigation of the unreinforced vault

An estimate of the ultimate lateral capacity only is insufficient in order to design experimental tests on shaking tables. The characteristics of the signal represent a critical aspect to ensure that the vault is adequately tested. In particular, the natural frequency of the vault must be well contained in the input signals. In order to define the frequency content of the signals, several modal analyses have been performed.
For this reason, a numerical FEM model was built on a micro-modelling approach base. Both masonry bricks and mortar joints have been modelled using shell elements with a linear-elastic material (elastic parameters provided in table 5.1).

The non-linear behaviour has been modelled using a specific interface element between mortar and brick. In particular both cohesive and frictional contact models have been considered.
This modelling strategy is due to experimental results obtained from previous dynamic tests on a similar specimen where cracks at the interfaces between mortar and brick have been always observed.
Therefore, the non-linear behaviour is due to the interface behaviour, while both the bricks and mortar joints remain in the elastic state.
The mechanical parameters of the interaction model have been calibrated in previous experimental tests *[Giamundo et al. 2015]* where several dynamic tests have been performed on a masonry specimen with similar curved portion but without abutments. The mechanical values used for the FEM model are shown in table 5.4.

Table 5.4: *Mechanical characterization of the bond at the interface between mortar and brick.*

Mechanical Parameter	Value
Normal stiffness modulus [N/mm^3]	46
Shear stiffness modulus [N/mm^3]	46
Friction angle [°]	38.02

The dynamic behaviour (natural frequency) assessed by preliminary calculations was experimentally confirmed as well. The modal analysis has been conducted in order to estimate the natural frequencies both of the unreinforced and of the strengthened vault.
The numerical model provides a natural frequency of 7.25 Hz on the unreinforced specimen (figure 5.22), whereas experimental results provide a natural frequency equal to 7.22 Hz.

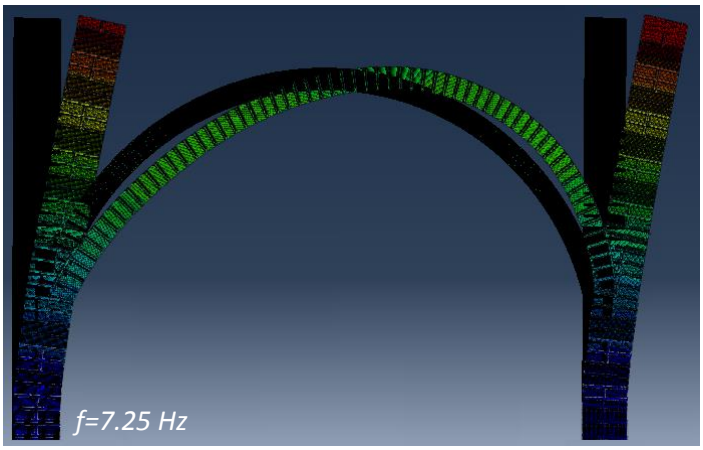

Figure 5.22: *Results of the modal analysis: first mode shape for the unreinforced specimen.*

5.3.4. Dynamic investigation of the strengthening vault

A similar approach has been performed for the strengthened specimen where several strengthening techniques have been combined. The assessment of the actual effects of several interventions is not simple, especially in a preliminary analysis.

The several strengthening systems involve multiple effects on the dynamic behaviour. The several interventions have been performed in order to improve the dynamic behaviour of the specimen.

The curved masonry elements and their portions adjacent to the lateral abutments are certainly most interested by the interventions.

Therefore, another numerical model was developed for the strengthened vault. In particular, the interface model was applied only on curved elements and abutments.

The masonry rib has been modelled by means of homogenous shell elements (both brick and mortar joints) with a linear-elastic behaviour. The elastic properties of the masonry rib are shown in table 5.2.

Then, the TRM system has been modelled with shell element perfectly bonded on the extrados surface. In fact, the perfect bond of strengthening

system to masonry substrate was experimentally confirmed as well. Finally, the steel tie has been modelled by means of an internal constraint.
The FEM model provided a natural frequency of 11.23 Hz (figure 5.23). The experimental results provided a natural frequency equal to 13.38 Hz.

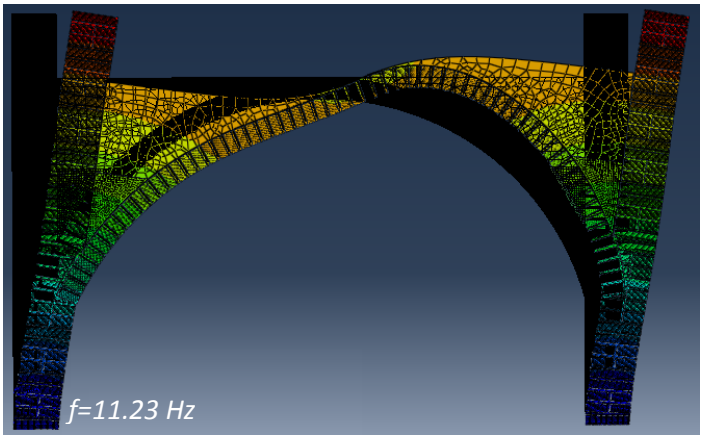

Figure 5.23: *Results of the modal analysis: first mode shape for the strengthened specimen.*

The results of the modal analysis showed the different dynamic response of the two specimens. The unreinforced vault exhibits a first mode shape that involves the entire structure (figure 5.22). The first mode of the strengthened specimen shows a rigid behaviour between left and right side (figure 5.23).
Furthermore, it is interesting to note that the keystone represents a crucial section for the strengthened vault. It is due to the accentuated distortion of the vault's keystone experimentally confirmed as well.

5.4. Instrumentation of specimens

The specimens have been instrumented in order to monitor the structural behaviour of the vault during the dynamic tests. The instruments were placed in several locations of each specimen.

Eight devices were placed on the profile of the curved element in order to monitor the acceleration values on the unreinforced masonry vault.
Figure 5.24 shows the instrumentation configuration (SN devices) used both for the unreinforced specimen and strengthened specimen.

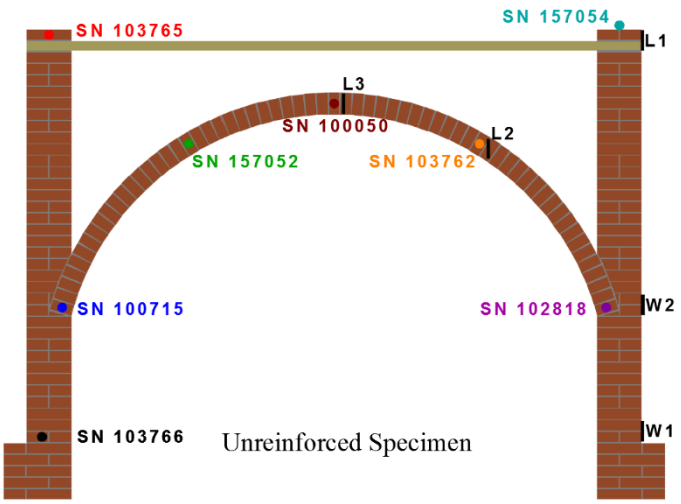

Figure 5.24: *Monitoring system of the unreinforced specimen.*

The displacements have been monitored by means of five laser displacement transducers (L and W devices). The displacement transducers were placed using the same configuration for both specimens (figure 5.25).

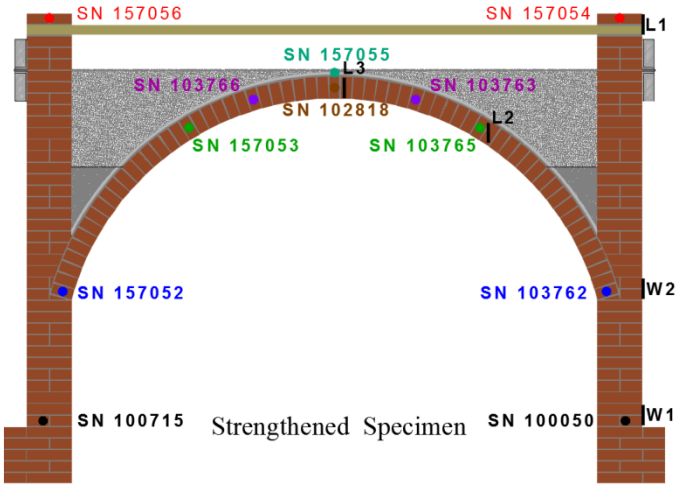

Figure 5.25: *Monitoring system of the strengthened specimen.*

However, the configuration of accelerometers was improved on the strengthened specimen with four additional devices.
The monitoring system records experimental data at 100Hz frequency.

5.5. Test programme: characteristics and description of seismic signals

The preliminary calculation provides information about the requirements for the seismic signals. The seismic capacity assessment on both specimens allows the estimation of the maximum intensity for each signal. Instead, a reliable estimate of the dynamic characteristics of the specimens provides the frequency content that must be contained in the input signals.
The planned test programme is different for the unreinforced and strengthened specimen. Overall, three typologies of input signals have been adopted. The dynamic tests have been performed in the plane of the masonry vault (unidirectional test).
In order to assess natural frequencies of the specimens (unreinforced and strengthened vault) a 30 seconds artificial random time history accelerogram has been adopted. The artificial signal, named random, is

obtained from a non-stationary random excitation having a large frequency content ranging from 1 to 30 Hz (figure 5.26).

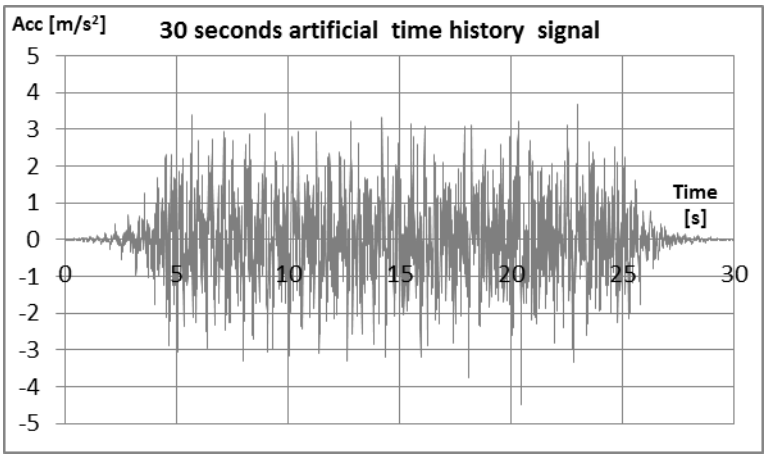

Figure 5.26: *Random signal for artificial time history accelerogram with a scale factor of 100%.*

In fact, only a signal composition obtained through multiple-frequency random excitations, provides an accurate estimation of the natural frequency for both specimens. The dynamic identification of the specimens has been performed according to the transfer function method.
The signal has a PGA of 4.50 m/s^2, and it has been scaled down to a PGA of 0.25 m/s^2 (i.e. scale factor of about 5%) to avoid undesirable damage. This signal has been applied on both specimens (unreinforced and strengthened vault).

5.5.1. Description of seismic signals assigned for the unreinforced specimen

The unreinforced specimen has been tested with a natural time history accelerogram which lasts 72.55 seconds. The signal recorded in Sturno (Campania, Italy) during the 1980 earthquake has been chosen for the entire first set (unreinforced vault).

The original signal (figure 5.27), progressively scaled up to the collapse condition, has a PGA of 1.78 m/s^2 (i.e. scale factor equal to 100%).

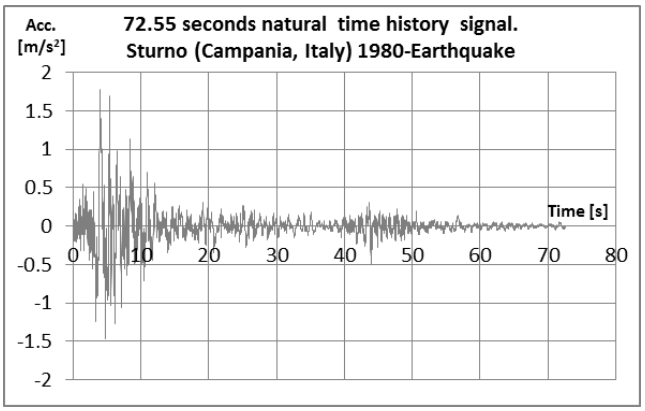

Figure 5.27: *Sturno signal for natural time history accelerogram with a scale factor of 100%.*

Furthermore, this input signal has a frequency content of about 8 Hz, which is very close to the natural frequency estimated from preliminary calculations.

Starting from the Sturno signal scaled from a PGA of 0.432 m/s^2 up to a PGA value of 2.170 m/s^2 (collapse occurrence), five natural signals have been provided to the unreinforced vault. Additionally, the random signal has been applied before of each Sturno signal. Therefore, ten dynamic tests have been performed up to collapse.

It is worth remarking that during experimental tests, shaking tables are not able to exactly match the "desired" signal.

This issue always occurs, even after an accurate calibration of the entire control system. Therefore, at each theoretical PGA value (desired) corresponds an actual PGA value (achieved), achieved by the shaking tables system. In table 5.5, the desired and achieved PGA values have been reported according to the experimental programme with reference the unreinforced specimen.

Table 5.5: *Experimental programme for the unreinforced specimen.*

Test ID	Accelerogram	Scale factor [%]	PGA desired [m/s^2]	PGA achieved [m/s^2]	Specimen
SIGN2	Sturno	25%	0.442	0.432	Unreinforced
SIGN4	Sturno	50%	0.894	0.815	Unreinforced
SIGN6	Sturno	75%	1.336	1.119	Unreinforced
SIGN8	Sturno	100%	1.777	1.650	Unreinforced
SIGN10	Sturno	125%	2.219	2.170	Unreinforced

In order to avoid redundant information in the previous table, the maximum acceleration values of natural signals (Sturno signal) are provided without the (repeated) random signals.

5.5.2. Description of seismic signals assigned for the strengthened specimen

For the strengthened vault the Sturno signals (see paragraph 5.5.1) has been adopted only at the beginning of the experimental test.
In particular, the previous dynamic sequence carried out on the unreinforced specimen (five natural signals with increasing intensity) have been repeated on the strengthened vault.
Indeed, the first aim was to assess the effects of the strengthening interventions, repeating the dynamic sequence used for the unreinforced vault up to the Sturno signal scaled up to 125% when the collapse occurred previously.
Additionally, the same natural signal (Sturno signal) has been used with an intensity higher than 125%. In particular, increasing the signal up to a PGA value of 4.753m/s^2, the first visible damage has been achieved.
After damage occurrence, the Sturno signal with scale factor of 125% has been assigned again to the strengthened vault. In this way the efficacy of the strengthening techniques can be assessed after damage occurred due to

replicas. Starting from the Sturno signal scaled down to a PGA of 0.403 m/s^2 and up to a PGA equal to 4.753 m/s^2 plus a repetition with a scale factor of 125%, fourteen tests have been performed on the strengthened vault.

In addition to the Sturno signal a new set based on the seismic signal recorded during the Gemona (Friuli, Italy) 1976 earthquake has been used after the Sturno sequence.

This latter signal lasts 35.41 seconds with a frequency content of about 12 Hz, which is very close to the natural frequency of the specimen estimated through modal analyses. This latter signal (figure 5.28), progressively scaled up to the collapse condition, has a PGA value of 3.103 m/s^2 (i.e. scale factor equal to 100%).

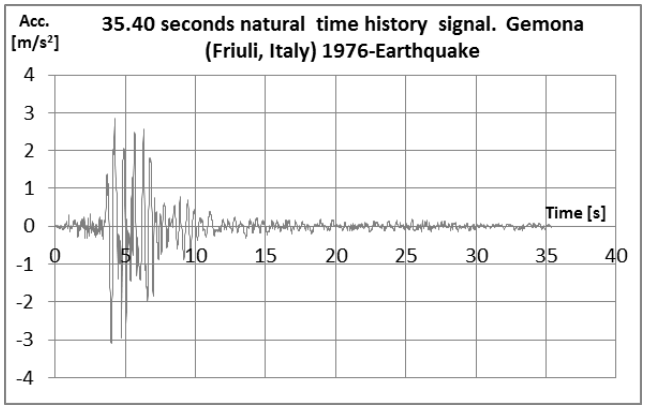

Figure 5.28: *Gemona signal for natural time history accelerogram with a scale factor of 100%.*

Starting from the Gemona signal scaled down to a PGA of 2.759 m/s^2 up to a PGA equal to 5.146 m/s^2, four additional dynamic tests have been performed on the strengthened vault up to the collapse.

Furthermore, in order to assess the natural frequency variation of the strengthened vault, each shaking has been preceded by a random signal. In particular, the last random signal has been applied after the first damage occurred (i.e. after the last Sturno signal). At the end of tests performed on

the strengthened specimen, a total of thirty-three dynamic tests has been carried out.

The natural frequency of the strengthened vault has been assessed again according to the transfer curve method, while after each test the masonry specimens have been inspected in order to detect the damage occurrence.

In table 5.6, the desired and achieved PGA values have been reported according to the experimental programme with reference to the strengthened specimen.

Table 5.6: *Experimental programme for the strengthened specimen.*

Test ID	Accelerogram	Scale factor [%]	PGA desired [m/s^2]	PGA achieved [m/s^2]	Specimen
SIGN12	Sturno	25%	0.442	0.403	Strengthened
SIGN14	Sturno	50%	0.894	0.746	Strengthened
SIGN16	Sturno	75%	1.336	1.178	Strengthened
SIGN18	Sturno	100%	1.777	1.620	Strengthened
SIGN20	Sturno	125%	2.219	2.062	Strengthened
SIGN22	Sturno	135%	2.396	2.219	Strengthened
SIGN24	Sturno	150%	2.661	2.534	Strengthened
SIGN26	Sturno	160%	2.848	2.759	Strengthened
SIGN28	Sturno	180%	3.201	2.838	Strengthened
SIGN30	Sturno	190%	3.378	3.083	Strengthened
SIGN32	Sturno	200%	3.555	3.427	Strengthened
SIGN34	Sturno	220%	3.908	4.419	Strengthened
SIGN36	Sturno	250%	4.439	4.753	Strengthened
SIGN38	Sturno	125%	2.219	2.072	Strengthened
SIGN40	Gemona	100%	3.103	2.759	Strengthened
SIGN41	Gemona	125%	3.879	3.712	Strengthened
SIGN42	Gemona	150%	4.655	3.938	Strengthened
SIGN43	Gemona	175%	5.421	5.146	Strengthened

In order to avoid redundant information in the previous table, the maximum acceleration values of natural signals (Sturno and Gemona signals) are provided without the random signals.

Chapter 6

RESULTS & DISCUSSION

The use of composite materials has shown to be effective for existing structures. In this background the experimental tests can provide an efficient contribution to the interpretation of the strengthening efficiency.
The experimental results of an innovative strengthening system are herein presented. The strengthening technique is based on TRM system (Textile Reinforced Mortar) in addition to traditional strengthening techniques. Their effects have been investigated by using the shaking table tests, both before and after application of the strengthening systems.
The strengthening system has been applied to a full-scale masonry vault typically found as roof in religious buildings. Several shaking table tests have been performed on the unreinforced and strengthened specimen.
In this Chapter the strengthening performance of the vault has been assessed comparing the behaviour detected during the tests.

6.1. Dynamic identification

The monitoring of both specimens allows to estimate their natural frequency evolution. In particular, the application of the transfer function between the signal generated at the base and monitored on the structure allows the calculation of the natural frequency.

6.1.1. Dynamic properties of unreinforced vault

The transfer function was evaluated during each random signal. Figure 6.1 shows the transfer function applied on the random signals before first and last seismic signal (collapse) for the unreinforced vault.

The natural frequency before the first signal (without damage) is 7.22Hz.

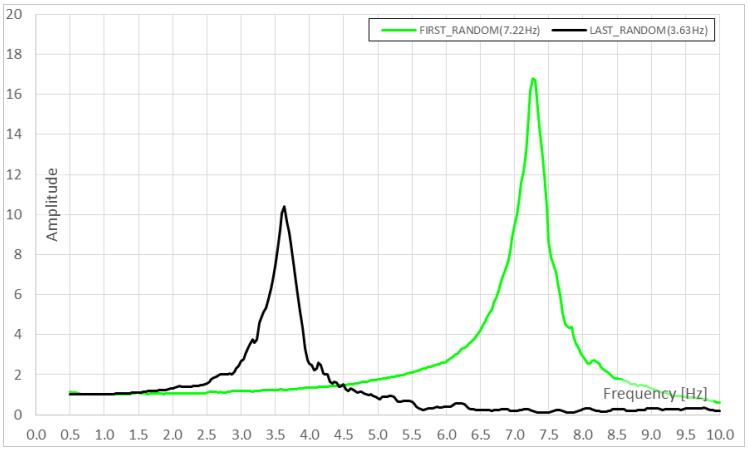

Figure 6.1: *Transfer function trend: undamaged unreinforced specimen (green) and before the collapse (black).*

6.1.2. Dynamic properties of strengthened vault

Similar approach has been performed on the strengthened vault (figure 6.2). The strengthened specimen showed a natural frequency equal to 13.38Hz (without damage).

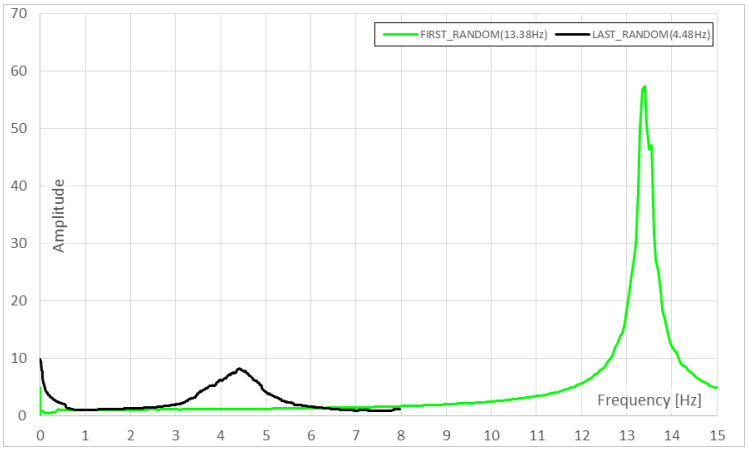

Figure 6.2: *Transfer function trend: undamaged strengthened specimen (green), after the first damage occurred (black).*

6.2. Structural damage assessment based on the transfer curve method

Starting from the transfer functions, also the gradual degradation of stiffness due to progressive damage can be assessed.
The random signal assigned before each seismic signal showed a progressive decrease of the natural frequency. This stiffness degradation has been observed for both specimens (unreinforced and strengthened vault).
In particular, for the unreinforced specimen before the collapse, the natural frequency is reduced up to -50% (3.63Hz) as shown in the figure 6.3.

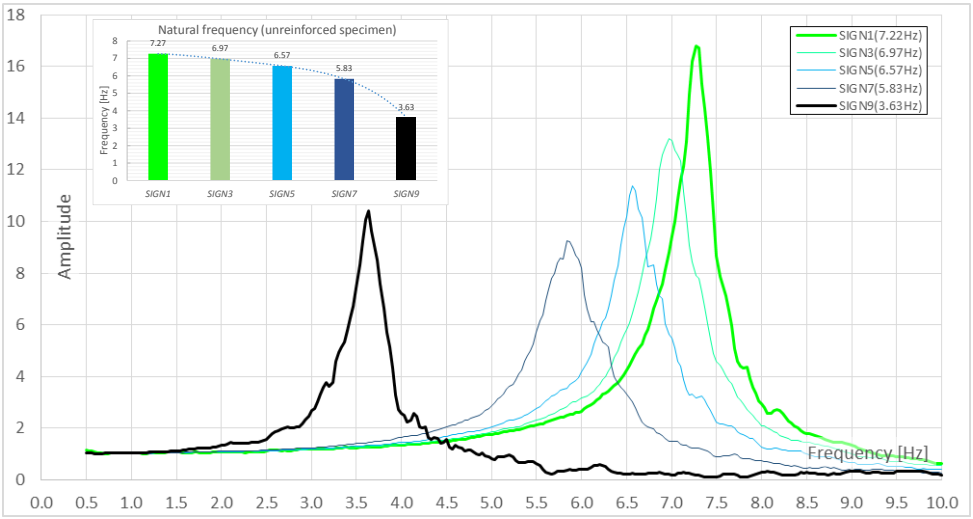

Figure 6.3: *Transfer functions trend: unreinforced specimen.*

Is interesting to assess the natural frequency decay (figure 6.4). The frequency decay can be calculated using following equation:

$$p_{f.d.} = \left| \frac{f_i - f_0}{f_0} \right| 100 \tag{6.1}$$

where f_i is the frequency estimated for a generic seismic signal i and f_0 is the frequency of the undamaged specimen.

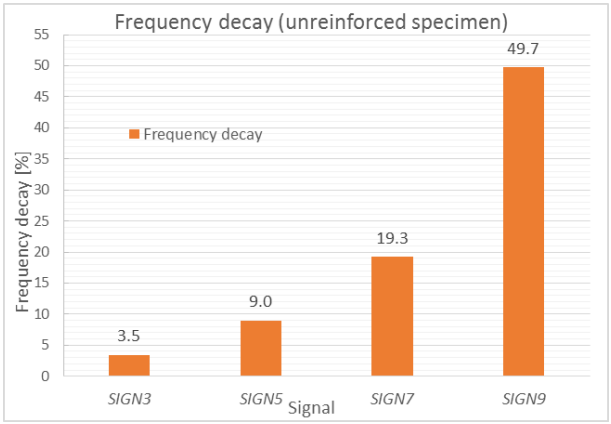

Figure 6.4: *Frequency decay (unreinforced vault).*

Instead, for the strengthened vault, before the first visible damage, the natural frequency is reduced up to -58% (5.67Hz). Before the collapse, the natural frequency is reduced up to -67% (4.48Hz) as shown in the figure 6.5.

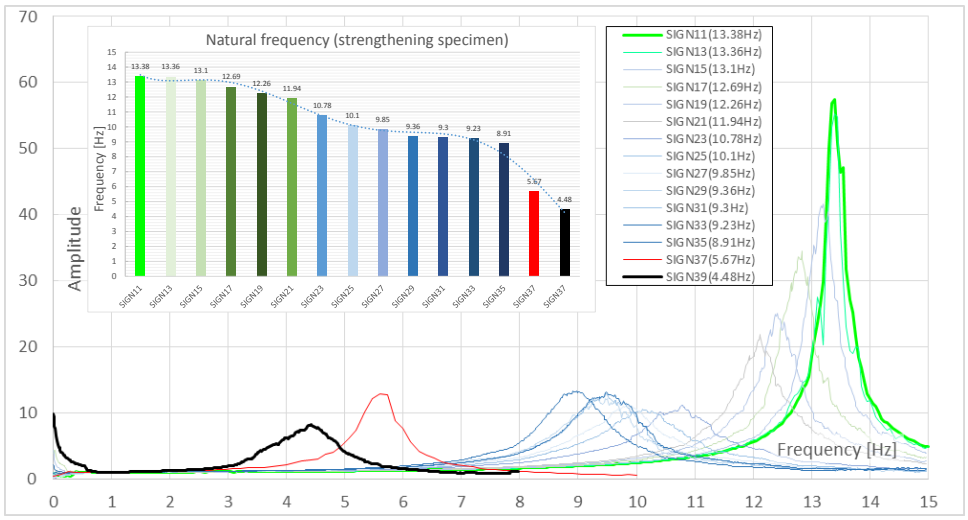

Figure 6.5: *Transfer functions trend: strengthened specimen*

After the signal named SIGN40, additional random signals (aimed to dynamic identification) have not been assigned due to the damage occurred.

In fact, once the damage occurs, the dynamic identification is not reliable. Therefore, the strengthened specimen has been tested by means of natural signals only up to the collapse.

The frequency decay estimation has been performed also for the strengthened masonry specimen. The frequency decay (figure 6.6) have been estimated using the previous equation (6.1).

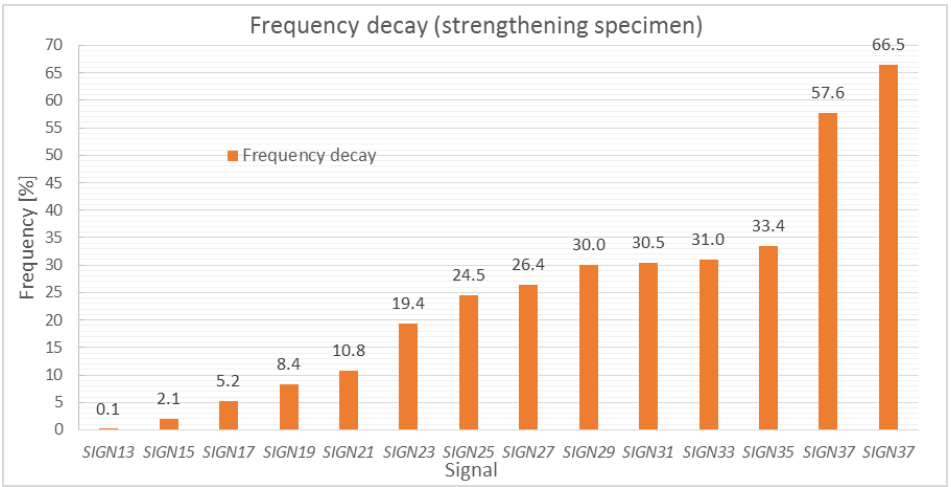

Figure 6.6: *Frequency decay (strengthened vault).*

It is interesting to analyse the development of the natural frequency varying the PGA achieved at base of specimens.

Furthermore, these data coupled with the corresponding frequency decay can provide significant information about the effectiveness of the strengthening techniques (figure 6.7).

This analysis has been provided until the signal named SIGN38, additional random signals (aimed to dynamic identification) have not been assigned due to the damage occurred. In fact, once the damage occurs, the dynamic identification is not reliable. Therefore, the strengthened specimen has been tested by means of natural signals only up to the collapse.

It is noted that with increasing steps of PGA the strengthened specimen shows a frequency decay lower than the one of unreinforced specimen. This

result remarks the effectiveness of the strengthening systems to improve the seismic response.

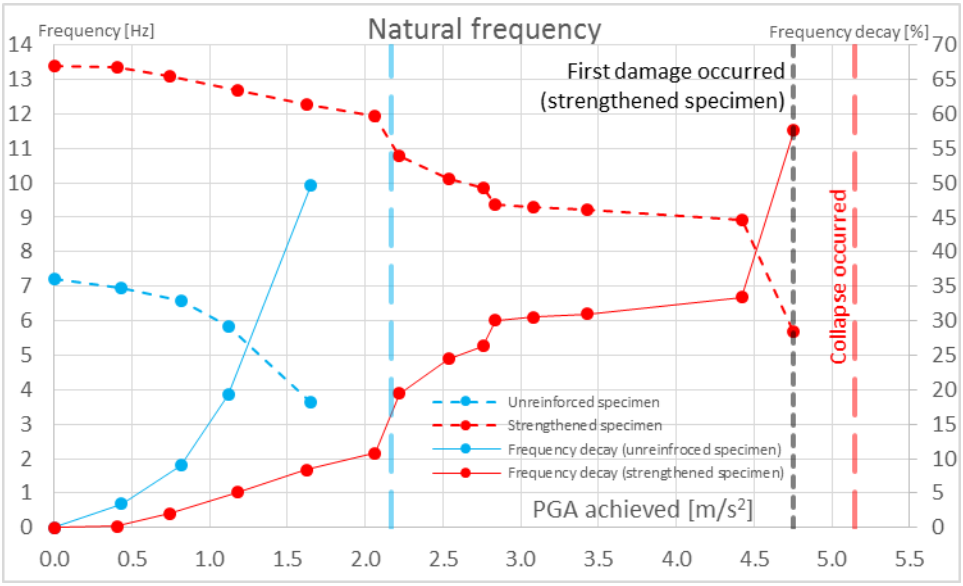

Figure 6.7: *Development of frequency and frequency decay at different PGAs (PGA value achieved at base).*

6.3. Damping ratio assessment

Finally, the half power bandwidth method *[Bracci et al. 1992]* has been adopted in order to assess the structural damping ratio ζ, for both specimens. This analysis has been conducted up to the signal named SIGN39, for previous reasons.

The damping ratio, ζ, has been calculated according to the well-known half-power bandwidth method as:

$$\zeta = \frac{\omega_1 - \omega_2}{2 \cdot \omega_n} \tag{6.2}$$

Where ω_n is the natural frequency and ω_2, ω_2 represent the frequencies for which the power input is half of the input at resonance.

In table 6.1 and 6.2 the experimental estimated damping ratios are shown for the unreinforced and strengthened specimen respectively.
The tested unreinforced specimen showed a damping ratio ζ, ranging between 2.12% and 4.54% (table 6.1).

Table 6.1: *Structural damping values for the unreinforced specimen (ξ values are expressed in %).*

Signal	Damping ζ [%]	Specimen
SIGN1	2.12%	Unreinforced
SIGN3	2.94%	Unreinforced
SIGN5	3.43%	Unreinforced
SIGN7	3.86%	Unreinforced
SIGN9	4.54%	Unreinforced

Indeed, the strengthening masonry vault showed a damping ratio. ζ, ranging from the 0.82% to the 9.45% (table 6.2).

Table 6.2: *Structural damping values for the strengthened specimen (ξ values are expressed in %).*

Signal	Damping ζ [%]	Specimen
SIGN11	0.82%	Strengthened
SIGN13	1.18%	Strengthened
SIGN15	1.52%	Strengthened
SIGN17	1.91%	Strengthened
SIGN19	2.13%	Strengthened
SIGN21	2.23%	Strengthened
SIGN23	4.73%	Strengthened
SIGN25	5.29%	Strengthened
SIGN27	5.45%	Strengthened
SIGN29	6.01%	Strengthened
SIGN31	6.22%	Strengthened
SIGN33	6.52%	Strengthened
SIGN35	6.97%	Strengthened
SIGN37	7.38%	Strengthened
SIGN39	9.45%	Strengthened

6.4. Seismic capacity and collapse mechanism: unreinforced vault

The unreinforced specimen has been tested by means of five natural signals with increasing intensity (Sturno signal) and five random signals characterized by a lower intensity with a constant scale factor. At the end of each test, several visual surveys have been conducted.

Up to the signal named SIGN8 (Sturno signal with scale factor 100%) evident damage has not been detected. However, a progressive damage was achieved at increasing seismic input, highlighted also in the transfer curves (figure 6.3).

The collapse occurred by activation of a hinge mechanism at a PGA value of 2.170 m/s^2 during the test SIGN10. The four plastic hinges activated almost instantaneously (figure 6.8).

The numerical and experimental comparison showed that both the PGA (2.26 m/s^2 according to the numerical model) and failure mode at collapse (location of four hinges activation) were confirmed by the analytical predictive model (see paragraph 5.3.1).

The experimental result endorses the hinge mechanism to be the limiting failure mode in the masonry vaults. The sliding or crushing failure can be achieved for particular geometric configurations, for example, when the *span/thickness* ratio is extremely reduced (i.e. non-slender masonry vaults).

Interesting is the assessment of the maximum acceleration induced in several monitored sections of the unreinforced specimen. The maximum values of the horizontal acceleration for each section (horizontal acceleration profile) provide information both on the acceleration distribution and on the variation of the seismic behaviour.

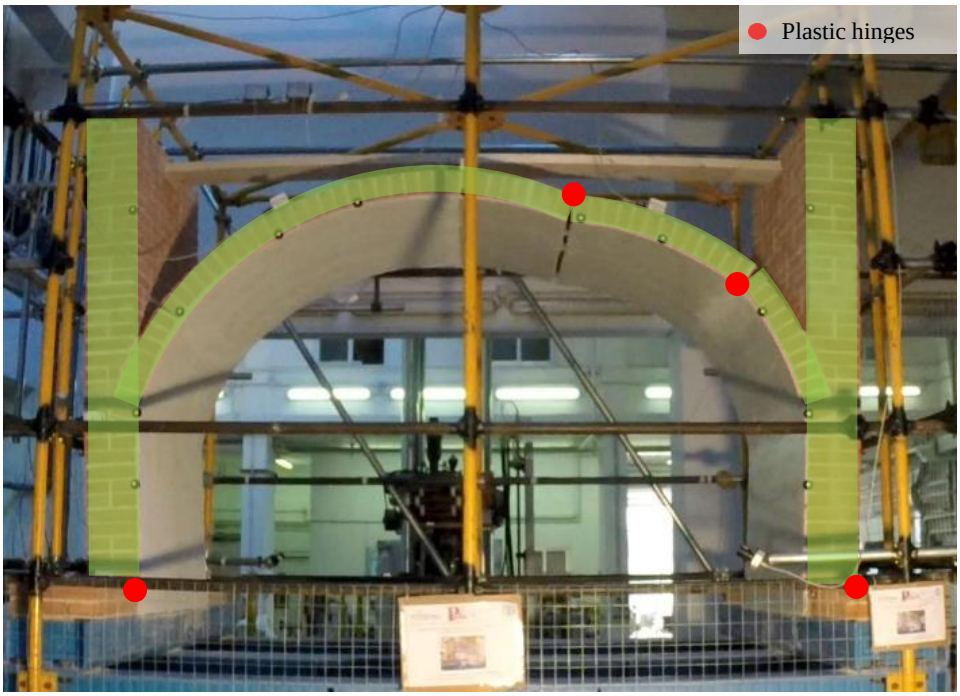

Figure 6.8: *Test SIGN10 for the unreinforced specimen (collapse occurred).*

Figures 6.9 and 6.10 show how the maximum horizontal accelerations are distributed up to the last signal named SIGN10 on the unreinforced vault. To each shape of the acceleration profile is associated a dynamic signal.

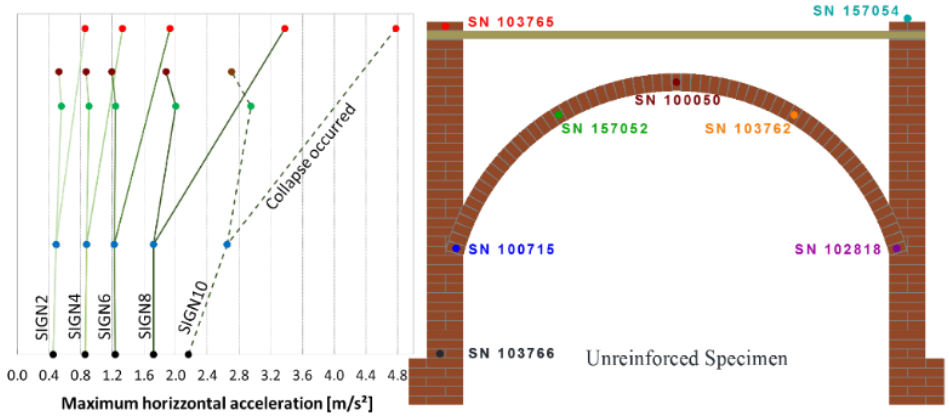

Figure 6.9: *Horizontal acceleration profiles of the unreinforced vault up to collapse (curved element and abutments comparison, left side).*

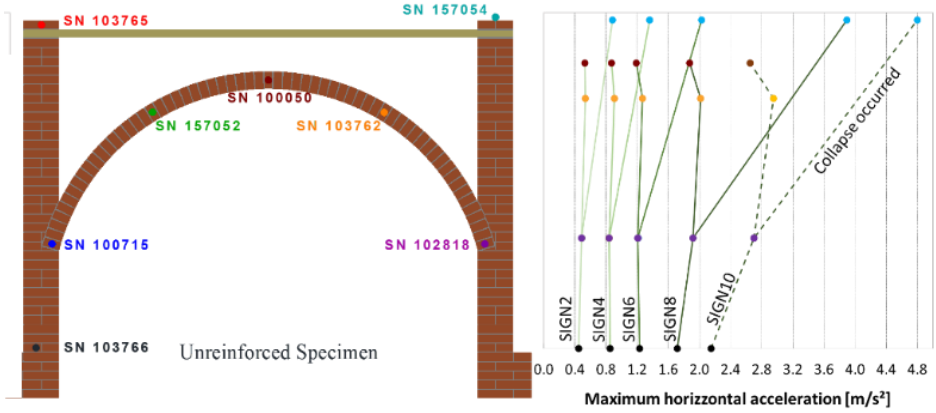

Figure 6.10: *Horizontal acceleration profiles of the unreinforced vault up to collapse (curved element and abutments comparison, right side).*

Starting from the acceleration profile, the different behaviours between the curved element and the abutments can be assessed. The several acceleration profiles show how the curved element exhibits a decoupled behaviour compared to the abutments.

The maximum value of the horizontal acceleration of 4.80 m/s^2 was achieved during the test SIGN10 on the top edge of the masonry abutments (right side, see figure 6.10). Furthermore, a maximum acceleration of 2.95 m/s^2 was achieved on the middle haunch of the curved element (right side, see figure 6.10) during the same signal.

The shape of the acceleration profile did not show a significant variation of the dynamic behaviour due to increase of the PGA value up to the test SIGN6. In fact, starting from the signal named SIGN8 up to the collapse, the distribution of the acceleration experiences a significant variation for both sides (figures 6.9 and 6.10).

The alteration of the dynamic behaviour can be analysed through the transfer curves too (figures 6.3 and 6.7). In particular, the figure 6.3 shows how the maximum frequency decay has been observed moving from the test SIGN6 to the test SIGN8.

Finally, the dynamic amplification between vault's imposts and specimen's bases increases significantly from the signal named SIGN6 to tests SIGN8 and SIGN10. The amplification value remains almost constant up to penultimate signal (i.e. SIGN8).

The horizontal acceleration profile at collapse highlights a symmetrical behaviour between the right and left side of the vault along the horizontal direction.

A symmetrical shape of the acceleration profile was highlighted also along the vertical direction (i.e. vertical acceleration profile), shown as follow (figure 6.11).

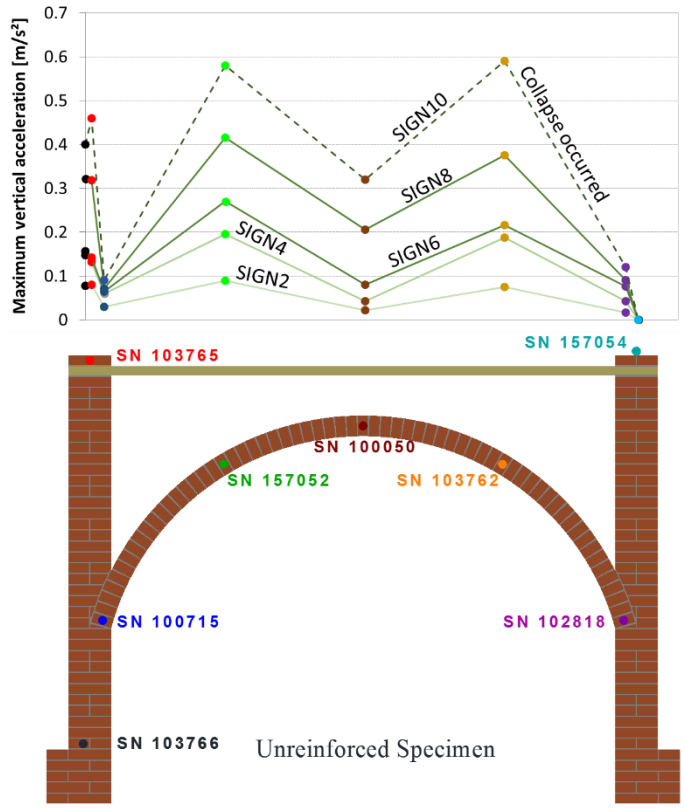

Figure 6.11: *Vertical acceleration profiles of the unreinforced vault up to collapse (curved element and abutments).*

6.5. Seismic capacity and collapse mechanism: strengthened vault

The previous set of signals used on the unreinforced vault has been performed again on the strengthened specimen. During the test SIGN20 (replica of the input signal with a scale factor of 125%), an acceleration of 2.062 m/s^2 was achieved at the base.

Even after this signal, the several visual surveys did not show any evident damage. This first experimental result proves that the strengthening systems strongly improved the seismic capacity of the specimen.

Figure 6.12 and figure 6.13 show the left and right acceleration profiles of first five dynamic signals performed on the strengthened vault.

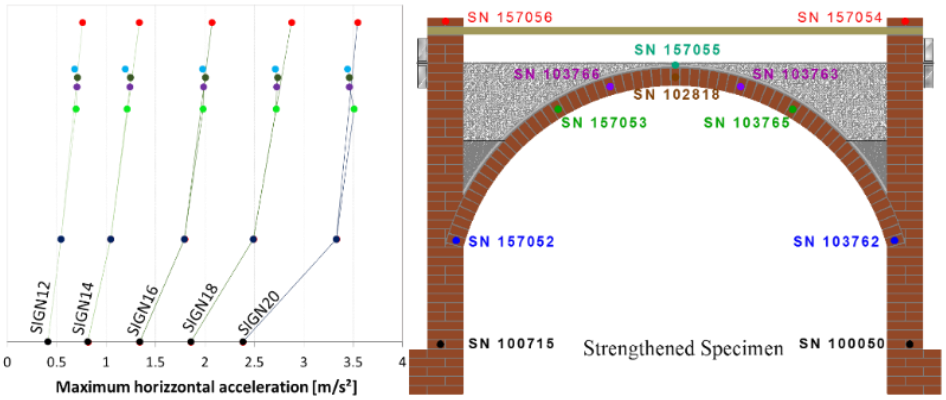

Figure 6.12: *Horizontal acceleration profiles of the strengthened vault up to signal named SIGN20 (curved element and abutments comparison, lift side).*

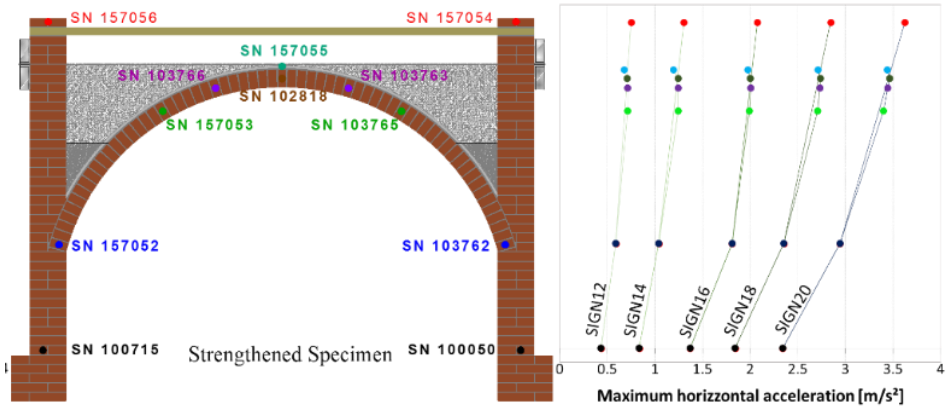

Figure 6.13: *Horizontal acceleration profiles of the strengthened vault up to signal named SIGN20 (curved element and abutments comparison, right side).*

The effects of the strengthening techniques are evident starting from the preliminar analyses. However, after strengthening, both the arch and the lateral abutments show a sort of rigid motion because their amplification profiles become almost overlapping.

The horizontal acceleration profile shows a symmetrical behaviour between left and right side of the vault. This effect is accentuated by the strengthening systems adopted.

The maximum value of the horizontal acceleration of 3.65 m/s^2 was achieved during the test SIGN20 on the abutments (right side, see figure 6.13). Furthermore, on the curved element, the maximum acceleration of 3.51 m/s^2 was achieved on the middle haunch (left side, see figure 6.12) during the same signal.

The shape and intensity of the acceleration profiles show a significant alteration at increasing intensity of the input signals. A variation of the shape of profile corresponds to a significant alteration of the dynamic behaviour as can be seen from the signal named SIGN24 (with scale factor of 150%).

However, already starting from the signal named SIGN22 the shape of the acceleration profile denotes how the stiffening effect of the strengthening

systems has been reduced. Then, the stiffness decay rapidly increases with the subsequent signals.

The change of dynamic behaviour can be analysed through the transfer curves also (figures 6.5 and 6.7), where the higher decay of the fundamental frequency between the test SIGN22 and SIGN24 is evident.

After the test SIGN34, the strengthened specimen resulted still not damaged at all.

A first local damage was achieved during the signal named SIGN36 (Sturno signal with a scale factor of 250%). An evident crack at the interface between mortar and brick was detected (figure 6.14 a)). In particular, the damage was localized at the vault's impost (right side) for an acceleration at the base of 4.753 m/s^2.

Furthermore, a surface cracking occurred close to the keystone (figure 6.14 b)). In particular, at the intrados, interface cracking occurred along the entire depth (116cm) of the curved element, in two sections.

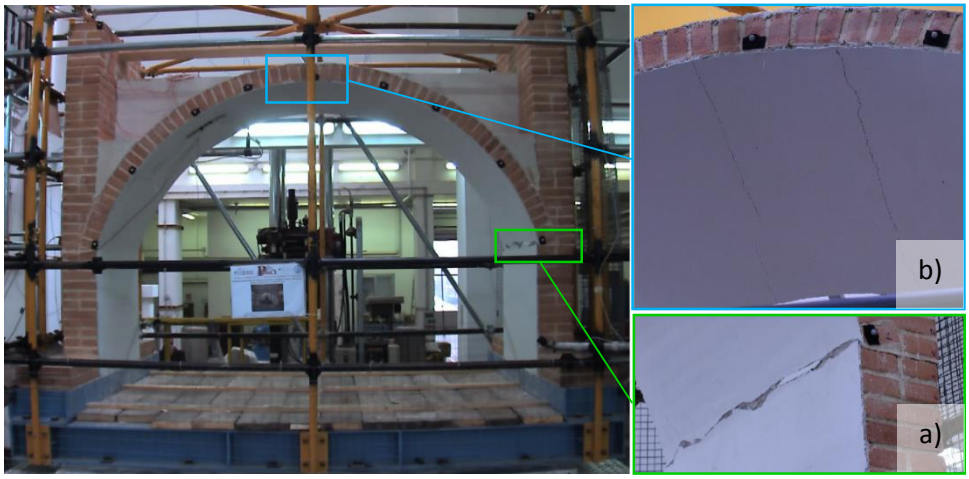

Figure 6.14: *Test SIGN36 for the strengthened specimen (damage occurred)*

Afterwards, the first evident damage occurred and the signal with a scale factor of 125% (i.e. the shaking yielding to collapse of the unreinforced

specimen) has been performed again (SIGN38). After the last Sturno signal, the specimen did not show any additional damage.

Figures 6.15 and 6.16 show the acceleration profiles starting from signal named SIGN38 (signal replica with a scale factor equal to 125%) up to signal SIGN43 when the collapse occurred. The acceleration profiles were shown separately for the left and right side.

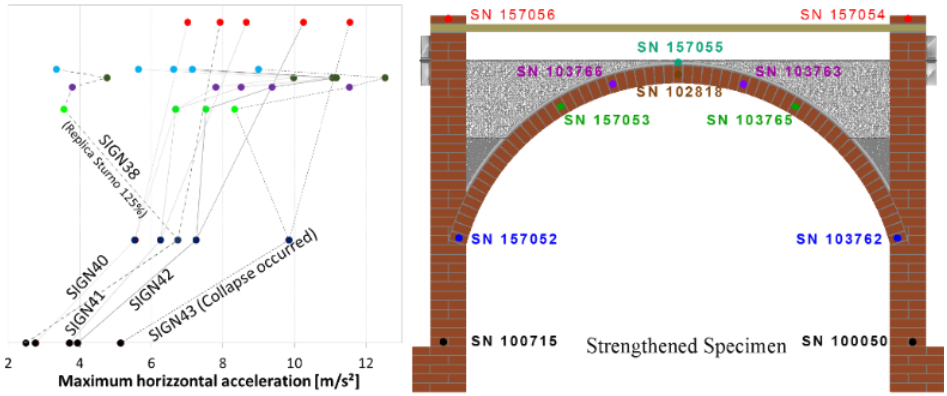

Figure 6.15: *Horizontal acceleration profiles of the strengthened vault starting from signal named SIGN40 up to SIGN43 (curved element and abutments comparison, left side).*

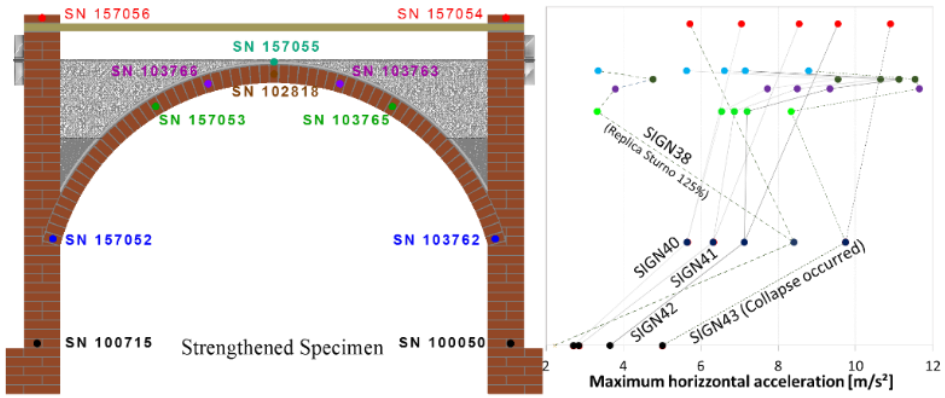

Figure 6.16: *Horizontal acceleration profiles of the strengthened vault starting from signal named SIGN40 up to SIGN43 (curved element and abutments comparison, right side).*

It is interesting to note how the signal replica (SIGN38) yields to a shape of the acceleration profiles totally changed compared to test SIGN20. In particular, on the right side and left side, they are completely different both in terms of shape and of intensity (non-symmetrical response between the right and left side of the specimen), and it is attributed to impairment of strengthening efficiency.

Finally, the acceleration profiles calculated during the last set of signals show the complete loss of the stiffening effect due to the strengthening systems.

The present section shows the main aspects related to the experimental results. For a thorough chart refer to Appendix ***A*** where the full results are provided with different acceleration profiles.

The experimental test has been performed up to the global collapse by means of a new set of signals (Gemona signal) with increasing intensity.

The collapse occurred with a hinge mechanism for a PGA of 5.146 m/s^2 recorded at the base of the vault during the signal named SIGN43. The numerical and experimental comparison shows that both the PGA (4.9 m/s^2 according to the numerical model) and the failure mode at collapse (four hinges localized at the two ends of the masonry abutments) were achieved according to the analytical predictive model (figure 6.17a). In addition to the hinge mechanism, an increase of the cracking at the intrados of the curved element occurred (figure 6.17b)).

The presence of the TRM strengthening prevented the formation of hinges. Indeed, the formation of the described cracks has occurred at the intrados of the curved element only. This effect was predicted by the preliminary calculation after the several strengthening techniques used.

It is interesting to note that no debonding failure occurred between the TRM system and the masonry substrate. In fact, after the test SIGN43 (collapse) the inorganic matrix resulted still perfectly bonded to the masonry substrate, with exception of the keystone where the debonding failure occurred.

Figure 6.17: *Test SIGN43 for the strengthened specimen (collapse occurred).*

However, it is due to the weight of an entire masonry block hanging after cracking occurred (figure 6.17 b)). These experimental results confirm the high bond properties of the TRM strengthening.

6.6. An actual case study in Italy: the monastery of Santo Spirito

The experimental tests (statically or dynamically performed) can provide important information about the structural behaviour and the effectiveness of several strengthening interventions. However, it is fundamental not to confine these results to scientific environment only.

The experimental results remark the effectiveness of the strengthening techniques adopted to strengthen the damaged specimen. Furthermore, the reversibility and compatibility of these strengthening techniques support its application in heritage buildings (like as monumental buildings and churches). Given the experimental results, these strengthening techniques have been applied on an actual heritage building on some masonry cross vaults.

The Monastery of Ocre in Italy (figure 6.18) has been chosen as demonstrator project according to the Research Project namely PON-

PROVACI (Technologies for Earthquake Protection and Valorisation of Cultural Heritage Sites).

Figure 6.18: *Monastery of Santo Spirito, Ocre (Italy).*

The Monastery was built in 13th century B.C.. The masonry system is characterised by a strong inhomogeneity both in texture and in masonry units. The masonry was mainly built with chaotic stones as shown in figure 6.19.

Figure 6.19: *Characteristics of masonry (Monastery of Santo Spirito).*

In the Monastery there are several masonry vaults made of solid clay bricks. Figure 6.20 shows a masonry cross vault typically found as roofs.

Figure 6.20: *Masonry vaults typically found as roofs (Monastery of Santo Spirito).*

With this demonstrator project several strengthening systems have been performed according to experimental results.

In the next section the construction phases by means of several strengthening systems will be shown.

The TRM application aimed to improve the seismic performance of the masonry curved elements. This strengthening system (figure 6.21) has been applied at the extrados of the curved element according to the construction phases previously discussed (see paragraph 5.2.2).

In addition, some masonry ribs were built over the extrados. These masonry ribs were located starting from the imposts up to haunch of the curved element (figure 6.22).

Figure 6.21: *TRM strengthening applied on the extrados of the masonry cross vault (Monastery of Santo Spirito).*

The masonry ribs were made of clay hollow bricks using single rows according to the strengthening system used for the experimental test (see paragraph 5.2.2).

Figure 6.22: *Masonry rib made of single rows of bricks (Monastery of Santo Spirito).*

In order to improve effectiveness of TRM system between the masonry ribs and the extrados of the vault, an additional basalt fibre grid has been applied (figure 6.23).

Figure 6.23: *Additional TRM strengthening on the masonry ribs and its covering (Monastery of Santo Spirito).*

In this way the connection between masonry ribs and substrate is guaranteed by an additional TRM system. The entire surface (masonry ribs and additional TRM strengthening) was covered by two mortar layers according to the manufacture phases previously discussed (see paragraph 5.2.2).
The engineering application briefly discussed shows an actual implementation of the strengthening techniques previously tested (see chapter 5).

Chapter 7

CONCLUSIONS

The Ph.D. thesis debated about the main aspects related to the analysis of slender masonry vaults without any backfill and with high *span/thickness* ratios, as those typically used in religious buildings as roofing.

Their analysis by using the Heyman's Theory cannot be performed due to the very low axial force values, typically reached. Indeed, if no-tension is assumed, the collapse is expected, by means of theoretical analysis, even under gravitational load (even if the real structure shows no evidence of any structural problem) hence a tensile strength value should be assumed.

An analytical model aimed at the assessment of slender masonry barrel vaults has been proposed.

The equations in closed form are provided to account for three possible material behaviours (linear-elastic, cracking and plastic with stress block model).

The proposed model is easily implementable by means of a solving algorithm in order to perform a limit or incremental analysis. The solving algorithm has been implemented by means of the Wolfram Mathematica software.

Through the numerical and experimental comparison, the proposed analytical method has been validated. In particular, the specimen experimentally tested by means of shaking table test has been analysed by using the proposed simplified model.

The plastic failure surface has been chosen for the masonry material.

Starting from mechanical parameters estimated by experimental tests the analytical model has been used to estimate the seismic capacity of the vault.

An incremental analysis has been performed in order to evaluated both the

evolution of the plastic hinges (i.e. evolution of the collapse mechanism) and the collapse acceleration.

The numerical result provides a λ of 0.54 g. The theoretical PGA value at collapse is very close to experimental PGA achieved during the last signal (i.e. 0.48g).

The agreement in terms of both activation multiplier and failure mode (i.e. hinge mechanism pattern, comparing experimental locations and theoretical outcomes) is very satisfactory.

Starting from the validated model, several sensitivity analyses have been performed. The results of the sensitivity analysis provide the impact of different parameters, both geometrical and mechanical, on the structural capacity.

The results showed that, under no-tensile strength assumption, the influence of the typologies of masonry can be neglected.

Indeed, the model is sensitive to tensile strength of masonry and its impact on the seismic capacity was estimated for a large number of cases.

In this background a reliable estimation of the tensile strength is essential.

The number of elements used for the discretization has a reduced impact on the capacity assessment.

Therefore, the proposed method is valuable to estimate the ultimate capacity of the masonry vaults, by using a simplified approach.

Furthermore, the model can be extended to the FRP, FRCM or TRM retrofit systems, being able to increase the load carrying capacity of the vaults.

This capacity increment is due to the expansion of the failure surface which moves far away from unreinforced failure condition. A further validation is required with experimentally tested retrofitted vaults.

Then, the analytical model has been used to design the shaking table tests performed on other masonry specimens. In particular, several shaking table tests have been carried out on a full-scale masonry vault with abutments. The tested specimen is representative of vaulted roofs typically used in religious buildings without any backfill.

After the unreinforced specimen has been tested, it has been repaired and strengthened by means of several techniques and tested again.

The analytical model provided reliable results and the hinge locations were correctly predicted. Furthermore, the structural capacity has been estimated with a good accuracy.

Finally, the experimental results have provided key information about the effectiveness of the strengthening systems.

In particular, a set of natural signals was used to shake the vault and damage evolution was analyzed by means of visual surveys while low intensity artificial random signals allowed performing dynamic identification and monitoring.

The benefits were experimentally confirmed by comparing the performance of the specimens, yielding to the following conclusions.

The failure mode of unreinforced specimen was achieved due to instant formation of four plastic hinges, which showed the fragility of the specimen at a PGA level of only 2.170 m/s^2.

After strengthening by combined system of TRM and traditional interventions, the seismic behavior of the vault was significantly improved.

The horizontal acceleration profiles showed a perfect symmetrical response of the vault up to almost the same PGA yielding to the failure of unreinforced specimen.

Increasing the PGA the instrumental response of the specimen started to change, however first visible damage occurred at a PGA almost doubled.

After a replica with the PGA of the unreinforced specimen failure, no additional damage was evident up to the collapse.

The collapse involved the formation of hinges in the abutments only, at a PGA level of 5.146 m/s^2.

The monitoring of both specimens allowed estimating their natural frequency evolution.

The initial natural frequency of the strengthened specimen was quite higher than unreinforced one and the reduction trends proved to be effective to identify damage occurrence even before visual evidence.

An estimate of damping ratio showed that maximum values reached at collapse are about 5% and 10%, respectively for unreinforced and strengthened specimen.

Finally, there was no debonding between TRM and the masonry substrate. The several strengthening strategies (combination of innovative and traditional ones) were effective in preventing global failure in the vault.

The seismic capacity of the specimen was more than doubled and the vulnerability moved from the curved element to the masonry abutments; hence additional interventions must be eventually made on the lateral abutments.

Finally, this strengthening system has been already implemented on a real heritage building. In particular, the Monastery of Santo Spirito (Ocre, Italy) has been chosen as demonstrator of the research project PROVACI, to implement the strengthening system presented and discussed in this Ph.D. thesis.

References

Akcay C., T. S. Bozkurt, B. Sayin & B. Yildizlar, (2016). *"Seismic retrofitting of the historical masonry structures using numerical approach"*. Construction and Building Materials, Vol. 113, pages 752-763. DOI:10.1016/j.conbuildmat.2016.03.121.

Akhaveissy A.H. & G. Milani, (2013). *"Pushover analysis of large scale unreinforced masonry structures by means of a fully 2D non-linear model"*. Construction and Building Materials, Vol. 41, pages 276-295. DOI:10.1016/j.conbuildmat.2012.12.006.

Almeida J.A.P.P., E.B. Pereira, J.A.O. Barros, (2015). *"Assessment of overlay masonry strengthening system under in-plane monotonic and cyclic loading using the diagonal tensile test"*. Construction and Building Materials, Vol. 94, pages 851-865. DOI:10.1016/j.conbuildmat.2015.07.040.

Andrejkovičová S., C. Alves, A. Velosa & F. Rocha, (2015). *"Bentonite as a natural additive for lime and lime–metakaolin mortars used for restoration of adobe buildings"*. Cement and Concrete Composites, Vol. 60, pages 99-110. DOI:10.1016/j.cemconcomp.2015.04.005.

Angelillo M. & A. Fortunato, (2004). *"Equilibrium of masonry vaults"*. In: M. Frémond, F. Maceri editors. Novel Approaches Civil Engineering S.E. – 6, vol. 14, Berlin Heidelberg: Springer. DOI: 10.1007/978-3-540-45287-4.

Angelillo M., E. Babilio & A. Fortunato, (2013). *"Singular stress fields for masonry-like vaults"*. Continuum Mech Thermodyn, Vol. 25, pages 423–441. DOI: 10.1007/s00161-012-0270-9.

Angelillo M., A. Fortunato, M. Lippiello & A. Montanino, (2014). *"Singular stress fields in masonry structures: derand was right"*. Meccanica, Vol. 49, pages 1243-1262. DOI: 10.1007/s11012-014-9880-6.

Asteris P.G., M.P. Chronopoulos, C.Z. Chrysostomou, H. Varum, V. Plevris, N. Kyriakides & V. Silva, (2014). *"Seismic vulnerability assessment of historical masonry structural systems"*. Engineering Structures, Vol. 62–63, pages 118-134. DOI:10.1016/j.engstruct.2014.01.031.

Augenti N., F. Parisi, A. Prota & G. Manfredi, (2010). *"In-plane lateral response of a full-scale masonry subassemblage with and without an inorganic matrix-grid strengthening system"*. Journal of Composites Construction, Vol. 15, pages 578–90. DOI: 10.1061/(ASCE)CC.1943-5614.0000193.

Banfill P.F.G., E.M. Szadurski & A.M. Forster, (2016). *"Deterioration of natural hydraulic lime mortars, II: Effects of chemically accelerated leaching on physical and*

mechanical properties of carbonated materials". Construction and Building Materials, Vol. 111, pages 182–190. DOI:10.1016/j.conbuildmat.2016.02.055.

Basili M., G. Marcari & F. Vestroni, (2016). *"Nonlinear analysis of masonry panels strengthened with textile reinforced mortar"*. Engineering Structures, Vol. 113, pages 245-258. DOI:10.1016/j.engstruct.2015.12.021.

Benedetti D. & V. Petrini, (1984). *"On the seismic vulnerability of masonry buildings: Proposal of an evaluation procedure"*. L'Industria Italiana delle Costruzioni, No. 149, pages 66-78.

Bernardini A., R. Gori & C. Modena, (1990). *"Application of Coupled Analytical Models and Experiential Knowledge to Seismic Vulnerability Analyses of Masonry Buildings"*. Earthquake Damage Evaluation and Vulnerability Analysis of Buildings Structures.

Bertolesi E., G. Milani & R. Fedele, (2016). *"Fast and reliable non-linear heterogeneous FE approach for the analysis of FRP-reinforced masonry arches"*. Composites Part B: Engineering, Vol. 88, pages 189-200. DOI:10.1016/j.compositesb.2015.11.005.

Bolhassani M., A.A. Hamid & FL. Moon, (2016). *"Enhancement of lateral in-plane capacity of partially grouted concrete masonry shear walls"*. Engineering Structures, Vol. 108, pages 59-76. DOI:10.1016/j.engstruct.2015.11.017.

Borri A. & G. Cangi, (2004). *"Vulnerabilità ed interventi di prevenzione sismica nei centri storici umbri dell'alta Val Tiberina"*. XI Congresso Nazionale "L'ingegneria Sismica in Italia", ANIDIS, Genoa, Italy, 25-29 January.

Borri A., P. Casadei, G. Castori & J. Hammond, (2009). *"Strengthening of Brick Masonry Arches with Externally Bonded Steel Reinforced Composites"*. Journal of Composites for Construction, Vol. 13(6), pages 468-475. DOI:10.1061/(ASCE)CC.1943-5614.0000030.

Bosiljkov V., A. Page, V. Bokan-Bosiljkov & R. Zarnic, (2003). *"Performance based studies on in-plane loaded unreinforced masonry walls"*. Masonry International, Vol. 16, No. 2, pages 39-50.

Bracci J.M., A.M. Reinhorn & J.B. Mander, (1992). *"Seismic Resistance of Reinforced Concrete Frame Structures Designed Only for Gravity Loads-Part III: Exp Performance and Analytical Study of a Model"*. State University of New York at Buffalo, Buffalo, New York (USA).

Brencich A. & R. Morbiducci, (2007). *"Masonry Arches: historical rules and modern mechanics"*. International Journal of Architectural Heritage, Vol. 1, pages 165–189. DOI: 10.1080/15583050701312926.

Briccoli Bati S., L. Rovero & U. Tonietti, (2007). *"Strengthening masonry arches with composite materials"*. Composite for Construction. DOI:10.1061/(ASCE)1090-0268(2007)11:1(33).

Bruggi M. & G. Milani, (2015). *"Optimal FRP reinforcement of masonry walls out-of-plane loaded: A combined homogenization–topology optimization approach complying with masonry strength domain"*. Computers & Structures, Vol. 153, pages 49-74. DOI:10.1016/j.compstruc.2015.02.004.

Calderini C., S. Cattari & S. Lagomarsino, (2009). *"In-plane strength of unreinforced masonry piers"*. Earthquake Engineering and Structural Dynamics, Vol. 38, pages 243-267. DOI:10.1002/eqe.860.

Calderini C. & S. Lagomarsino, (2014). *"Seismic Response of Masonry Arches Reinforced by Tie-Rods: Static Tests on a Scale Model"*. Structural Engineering. DOI:10.1061/(ASCE)ST.1943-541X.0001079.

Callaway P., M. Gilbert & C.C. Smith, (2012). *"Influence of backfill on the capacity of masonry arch bridges"*. Proceedings of the ICE – Bridge Engineering, Vol. 165, pages 147–57. DOI:10.1680/bren.11.00038.

Calvi G.M., (1999). *"A displacement-based approach for vulnerability evaluation of classes of buildings"*. Journal of Earthquake Engineering, Vol. 3, pages 411-438.

Caporale A., F. Parisi, D. Asprone, R. Luciano & A. Prota, (2014). *"Micromechanical analysis of adobe masonry as two-component composite: Influence of bond and loading schemes"*. Composite Structures, Vol. 112, pages 254–263. DOI:10.1016/j.compstruct.2014.02.020.

Caporale A., F. Parisi, D. Asprone, R. Luciano & A. Prota, (2015). *"Comparative micromechanical assessment of adobe and clay brick masonry assemblages based on experimental data sets"*. Composite Structures, Vol. 120, pages 208-220. DOI:10.1016/j.compstruct.2014.09.046.

Carozzi F.G., G. Milani & C. Poggi, (2014). *"Mechanical properties and numerical modeling of fabric reinforced cementitious matrix (FRCM) systems for strengthening of masonry structures"*. Composite Structures, Vol. 107, pages 711–725.

Černý R. & V. Kočí, (2015). *"4 - Traditional fired-clay bricks versus large and highly perforated fired-clay bricks masonry: Influence on buildings thermal performance"*. Eco-Efficient Masonry Bricks and Blocks, pages 63–81. DOI:10.1016/B978-1-78242-305-8.00004-8.

D'Ambrisi A., L. Feo & F. Focacci, (2013a). *"Experimental and analytical investigation on bond between carbon-FRCM materials and masonry"*. Composite Part. B Engineering, Vol. 46, pages 15–20.

D'Ambrisi A., L. Feo, F. Focacci, (2013b). *"Masonry arches strengthened with composite unbonded tendons"*. Composite Structures, Vol. 98, pages 323–329.

D'Ayala D. & E. Speranza, (2003). *"Definition of collapse mechanisms and seismic vulnerability of historic masonry buildings"*. Earthquake Spectra, No. 19, pages 479-509. DOI:10.1193/1.1599896.

Darbhanzi A., M.S. Marefat & M. Khanmohammadi, (2013). *"Investigation of in-plane seismic retrofit of unreinforced masonry walls by means of vertical steel ties"*. Construction and Building Materials, Vol. 52, pages 122-129. DOI:10.1016/j.conbuildmat.2013.11.020.

De Buhan P. & G. de Felice, (1997). *"A homogenization approach to the ultimate strength of brick masonry"*. Journal of the Mechanics and Physics of Solids, Vol. 45(7), pages 1085-1104. DOI: 10.1016/S0022-5096(97)00002-1.

De Santis S., G. de Felice G & D. Peluso, (2012). *"An overview on Italian railway masonry bridges with load-carrying capability estimate"*. Structural Analysis of Historical Constructions, Wroclae, Poland. ISSN 0860-2395H, ISBN 978-83-7125-216-7.

De Santis S. & G. de Felice, (2014). *"A fibre beam-based approach for the evaluation of the seismic capacity of masonry arches"*. Earthquake Engineering & Structural Dynamics, Vol. 43, pages 1661-1681. DOI: 10.1002/eqe.2416.

Dimitri R., L. De Lorenzis & G. Zavarise, (2011). *"Numerical study on the dynamic behavior of masonry columns and arches on buttresses with the discrete element method"*. Engineering Structures, Vol. 33(12), pages 3172–3188. DOI: 10.1016/j. engstruct.2011.08.018.

Dipasquale L., L. Rovero & F. Fratini, (2016). *"11 - Ancient stone masonry constructions"*. Nonconventional and Vernacular Construction Materials, pages 301-332. DOI:10.1016/B978-0-08-100038-0.00011-1.

Doglioni F., A. Moretti, & V. Petrini, (1994). *"Le chiese ed il terremoto"*, LINT, Trieste, Italy.

Drosopoulos G.A., G.E. Stavroulakis, & C.V. Massalas, (2007). *"FRP reinforcement of stone arch bridges: unilateral contact models and limit analysis"*. Composite Part B: Engineering, Vol. 38, pages 144–51. DOI: 10.1016/j.compositesb.2006.08.004.

EN. (2002). *"Methods of test for masonry units – Part 1: determination of compressive strength."* EN 772-1.

EN-11128. (2004). *"Prodotti da costruzione di laterizio – Tavelloni, tavelle e tavelline – Terminologia, requisiti e metodi di prova"*, [in Italian].

Esmaeeli E., E. Manning & J.A.O. Barros, (2013). *"Strain hardening fibre reinforced cement composites for the flexural strengthening of masonry elements of ancient structures"*. Construction and Building Materials, Vol. 38, pages 1010-1021. DOI:10.1016/j.conbuildmat.2012.09.065.

Fajfar P., P. Gašperšič, (1996). *"The N2 method for the seismic damage analysis of rc buildings"*. Earthquake Engineering and Structural Dynamics, Vol. 25, pages 31-46.

Fajfar P., (1999). *"Capacity spectrum method based on inelastic demand spectra"*. Earthquake Engineering and Structural Dynamics, Vol. 28, pages 979-993.

Falchi L., C. Varin, G. Toscano & E. Zendri, (2015). *"Statistical analysis of the physical properties and durability of water-repellent mortars made with limestone cement, natural hydraulic lime and pozzolana-lime"*. Construction and Building Materials. Vol. 78, pages 260-270. DOI:10.1016/j.conbuildmat.2014.12.109.

Falchi L., U. Müller, P. Fontana, F.C. Izzo & E. Zendri, (2013). *"Influence and effectiveness of water-repellent admixtures on pozzolana–lime mortars for restoration application"*. Construction and Building Materials, Vol. 49, pages 272–280. DOI:10.1016/j.conbuildmat.2013.08.030.

Fang S.Q., H. Zhang, B.J. Zhang & Y. Zheng, (2014). *"The identification of organic additives in traditional lime mortar"*. Journal of Cultural Heritage, Vol. 15(2), pages 144-150. DOI:10.1016/j.culher.2013.04.001.

Fanning J.P. & T.E. Boothby, (2001a). *"Three-dimensional modelling and full-scale testing of stone arch bridges"*. Computer & Structures, Vol. 79, pages 2645-2662. DOI: 10.1016/S0045-7949(01)00109-2.

Fanning J.P., T.E. Boothby & B.J. Roberts, (2001b). *"Longitudinal and transverse effects in masonry arch assessment"*. Construction and Building Materials, Vol. 15(1), pages 54-60. DOI: 10.1016/S0950-0618(00)00069-6.

Foraboschi P., (2004). *"Strengthening of masonry arches with fiber-reinforced polymer strips"*. Journal of Composites Construction, Vol. 8, pages 191–202. DOI: 10.1061/ (ASCE)1090-0268(2004) 8:3(191).

Foraboschi P. & A. Vanin, (2013). *"Non-linear static analysis of masonry buildings based on a strut-and-tie modeling"*. Soil Dynamics and Earthquake Engineering, Vol. 55, pages 44-58. DOI:10.1016/j.soildyn.2013.08.005.

Fortunato A., F. Fraternali & A. Angelillo, (2014). *"Structural capacity of masonry walls under horizontal loads"*. Ingegneria Sismica/International Journal Earthquake Engineering, Cap. 31, pages 41–51.

Furtado A., H. Rodrigues, A. Arêde & H. Varum, (2015). *"Experimental Characterization of the In-plane and Out-of-Plane Behaviour of Infill Masonry Walls"*. Procedia Engineering, Vol. 114, pages 862-869. DOI:10.1016/j.proeng.2015.08.041.

Furtado A., H. Rodrigues, A. Arêde & H. Varum, (2016). *"Experimental evaluation of out-of-plane capacity of masonry infill walls"*. Engineering Structures, Vol. 111, pages 48-63. DOI:10.1016/j.engstruct.2015.12.013.

Gago A.S., J. Alfaiate & A. Lamas, (2011). *"The effect of the infill in arched structures: analytical and numerical modelling"*. Engineering Structures, Vol. 33, pages 1450–1458. DOI: 10.1016/j.engstruct.2010.12.037.

Garmendia J.T. San-José, D. García & P. Larrinaga, (2011). *"Rehabilitation of masonry arches with compatible advanced composite material"*. Construction Building Materials, Vol. 25, pages 4374–4385.

Gattesco N., C. Amadio & C. Bedon, (2015). *"Experimental and numerical study on the shear behavior of stone masonry walls strengthened with GFRP reinforced mortar coating and steel-cord reinforced repointing"*. Engineering Structures, Vol. 90, pages 143-157. DOI:10.1016/j.engstruct.2015.02.024.

Giamundo V., G. P: Lignola, A. Prota & G. Manfredi, (2014). *"Nonlinear analyses of adobe masonry walls reinforced with fiberglass mesh"*. Polymers (Basel), Vol. 6, pages 464–78. DOI: 10.3390/polym6020464.

Giamundo V., G.P. Lignola, G. Maddaloni, A. Balsamo, A. Prota & G. Manfredi, (2015). *"Experimental investigation of the seismic performances of IMG reinforcement strengthening on curved masonry elements"*. Composite Part. B Engineering, Vol. 70, pages 53-63.

Girardello P., A. Pappas, F. da Porto & R. M. Valluzzi (2013). *"Experimental testing and numerical modelling of masonry vaults"*. 13th Int. Conf. Rehabil. Restor. Struct., Chennai, pages 1–10.

Giresini L., M. Fragiacomo & M. Sassu, (2016). *"Rocking analysis of masonry walls interacting with roofs"*. Engineering Structures, Vol. 116, pages 107-120. DOI:10.1016/j.engstruct.2016.02.041.

Giuffrè A., (1993). *"Sicurezza e conservazione dei centri storici in area sismica, il caso Ortigia"*. Laterza, Bari, Italy.

Grünthal G., (1998). *"European Macroseismic Scale 1998"*. Cahiers du Centre Européen de Géodynamique et de Séismologie. Vol. 15.

Heyman J., (1995). *"The stone skeleton"*. Structural engineering of masonry architecture. Cambridge: Cambridge University Press.

IBC2009. Italian Building Code: *"Circolare 617/2009 ministero delle Infrastrutture dei trasporti. Istruzioni per l'applicazione delle "Norme Tecniche per le Costruzioni" D.M. 14/01/2008"*.

Illampas R., D.C. Charmpis & I. Ioannou, (2014). *"Laboratory testing and finite element simulation of the structural response of an adobe masonry building under horizontal loading"*. Engineering Structures, Vol. 80, pages 362–376. DOI:10.1016/j.engstruct.2014.09.008.

Jasienko J., A. Di Tommaso & L. Bednarz L, (2009). *"Experimental investigation into collapse of masonry arches reinforced using different compatible technologies"*. MuRiCo3 Mechanics of Masonry Structures Strengthened Eith Composite Materials.

Katalin B., (2014). *"When Heyman's Safe Theorem of rigid block systems fails: Non-Heymanian collapse modes of masonry structures"*. International Journal of Solids and Structures, Vol. 51(14), pages 2696-2705. DOI: 10.1016/j.ijsolstr.2014.03.041.

Lagomarsino S., (1998a). *"Seismic damage survey of the churches in Umbria"*. Workshop on Seismic Performance of Monuments, Lisbon, Spain, pages 167-176.

Lagomarsino S., (1998b). *"A new methodology for the post-earthquake investigation of ancient churches"*. XI European Conference on Earthquake Engineering, Paris, France, page 67.

Lagomarsino S. & S. Podestà, (2004a). *"Seismic Vulnerability of Ancient Churches: I. Damage Assessment and Emergency Planning"*. Earthquake Spectra, Vol. 20, No. 2, pages 377-394.

Lagomarsino S. & S. Podestà, (2004b). *"Damage and vulnerability assessment of the churches after the 2002 Molise, Italy, earthquake"*. Earthquake Spectra, Vol. 20, pages 271-283.

Lagomarsino S., S. Podestà, S. Resemini, E. Curti & S. Parodi, (2004c). *"Mechanical models for the seismic vulnerability assessment of churches"*. IV International Seminar on Structural Analysis of Historical Constructions - SAHC04, Padua, Italy, Vol. 2, pages 1091-1101.

Landi L., R. Gabellieri & P.P. Diotallevi, (2015). *"A model for the out-of-plane dynamic analysis of unreinforced masonry walls in buildings with flexible diaphragms"*. Soil Dynamics and Earthquake Engineering, Vol. 79, Part A, pages 211-222. DOI:10.1016/j.soildyn.2015.09.013.

Leone G., A. De Vita, A. Magnani & C. Rossi, (2016). *"Characterization of archaeological mortars from Herculaneum"*. Thermochimica Acta, Vol. 624, pages 86–94. DOI:10.1016/j.tca.2015.12.003.

Lignola G.P., A. Flora & G. Manfredi, (2008). *"Simple Method for the Design of jet Grouted Umbrellas in Tunneling"*. Journal of Geotechnical and Geoenvironmental Engineering, Vol. 134(12), pages 1778-1790. DOI: 10.1061/(ASCE)1090-0241(2008)134:12(1778).

Lignola G.P., A. Prota & G. Manfredi, (2009). *"Nonlinear analyses of tuff masonry walls strengthened with cementitious matrix-grid composites"*. Composite Construction. 10.1061/(ASCE)CC.1943-5614.0000007.

Lignola G.P., A. Prota & G. Manfredi, (2012). *"Numerical investigation on the influence of FRP retrofit layout and geometry on the in-plane behavior of masonry walls"*. Composite Construction. DOI:10.1061/(ASCE)CC.1943-5614.0000297.

Lombillo I., C. Thomas, L. Villegas, J.P. Fernández-Álvarez & J. Norambuena-Contreras, (2013). *"Mechanical characterization of rubble stone masonry walls using non and minor destructive tests"*. Construction and Building Materials, Vol. 43, pages 266–277. DOI:10.1016/j.conbuildmat.2013.02.007.

Lourenço P.B., D.V. Oliveira, P. Roca & A. Orduna, (2005). *"Dry joint stone masonry walls subjected to in-plane combined loading"*. Journal of Structural Engineering, ASCE. Vol. 131, No.11, pages 1665-1673. DOI:10.1061/(ASCE)0733-9445(2005)131:11(1665).

Magenes G. & G.M. Calvi (1992). *"Cyclic behaviour of brick masonry walls"*. X World Conference on Earthquake Engineering, Madrid, Spain, pages 3517-3522.

Magenes G. & G.M. Calvi (1997). *"In-plane seismic response of brick masonry walls"*. Earthquake Engineering and Structural Dynamics, Vol. 26, pages 1091-1112.

Mazzotti C., E. Sassoni & G. Pagliai, (2014). *"Determination of shear strength of historic masonries by moderately destructive testing of masonry cores"*. Construction and Building Materials, Vol. 54, pages 421-431. DOI:10.1016/j.conbuildmat.2013.12.039.

Melbourne C. & M. Gilbert, (1995). *"The behaviour of multiring brickwork arch bridges"*. Journal of the Institution Structural Engineers, Vol. 73, pages 39–47.

Mendes N. & P.B. Lourenço, (2014). *"Sensitivity analysis of the seismic performance of existing masonry buildings"*. Engineering Structures, Vol. 80, pages 137-146. DOI:10.1016/j.engstruct.2014.09.005.

Milani G. & M. Valente, (2015a). *"Comparative pushover and limit analyses on seven masonry churches damaged by the 2012 Emilia-Romagna (Italy) seismic events: Possibilities of non-linear finite elements compared with pre-assigned failure mechanisms"*. Engineering Failure Analysis, Vol. 47, Part A, pages 129-161. DOI:10.1016/j.engfailanal.2014.09.016.

Milani G., M. Valente, (2015b). *"Failure analysis of seven masonry churches severely damaged during the 2012 Emilia-Romagna (Italy) earthquake: Non-linear dynamic analyses vs conventional static approaches"*. Engineering Failure Analysis, Vol. 54, pages 13-56. DOI:10.1016/j.engfailanal.2015.03.016.

Milankovitch M., (1907). *"Theorie der Druckkurven. Zeitschrift Für Math Und Phys 1907"*. Vol. 55, pages 1–27.

Milosevic J., M. Lopes, A. S. Gago & R. Bento, (2015). *"In-plane seismic response of rubble stone masonry specimens by means of static cyclic tests"*. Construction and Building Materials, Vol. 82, pages 9-19. DOI:10.1016/j.conbuildmat.2015.02.018.

Minaie E., F.L. Moon & A.A. Hamid, (2014). *"Nonlinear finite element modeling of reinforced masonry shear walls for bidirectional loading response"*. Finite Elements in Analysis and Design, Vol. 84, pages 44-53. DOI:10.1016/j.finel.2014.02.001.

Mojsilović N., M. Petrović and X. R. Anglada, (2015). *"Masonry elements with multi-layer bed joints: Behaviour under monotonic and static-cyclic shear"*. Construction and Building Materials, Vol. 100, pages 149-162. DOI:10.1016/j.conbuildmat.2015.09.065.

Moseley H., (1843). *"The theory, practice and architecture of bridges of stone, iron, timber and wire with examples on the principle of suspension"*. J. Weale, London 1843.

Mueller A., A. Schnell & K. Ruebner, (2015). *"The manufacture of lightweight aggregates from recycled masonry rubble"*. Construction and Building Materials, Vol. 98, pages 376–387. DOI:10.1016/j.conbuildmat.2015.07.027.

Noor-E-Khuda S., M. Dhanasekar & D.P. Thambiratnam, (2016a). *"An explicit finite element modelling method for masonry walls under out-of-plane loading"*. Engineering Structures, Vol. 115, pages 103-120.

Noor-E-Khuda S., M. Dhanasekar & D.P. Thambiratnam, (2016b). *"Out-of-plane deformation and failure of masonry walls with various forms of reinforcement"*. Composite Structures, Vol. 140, pages 262-277. DOI:10.1016/j.compstruct.2015.12.028.

Oppenheim I.J., (1992). *"The masonry arch as a four-link mechanism under base motion"*. Earthquake Engineering and Structural Dynamics, Vol. 21(11), pages 1005–1017. DOI: 10.1002/eqe.4290211105.

Papanicolaou C.G., T.C. Triantafillou., K. Karlos & M. Papathanasiou, (2007). *"Textile reinforced mortar (TRM) versus FRP as strengthening material of URM walls: in-plane cyclic loading"*. Materials and Structures, Vol. 40, pages 1081–1097.

Papanicolaou C.G., T.C. Triantafillou, M. Papathanasiou, K. Karlos, (2008). *"Textile reinforced mortar (TRM) versus FRP as strengthening material of URM walls: out-of-plane cyclic loading"* Materials Structurers Vol. 41, pages 143–157.

Parisi F., G.P. Lignola, N. Augenti, A. Prota & G. Manfredi (2011). *"Nonlinear behavior of a masonry subassemblage before and after strengthening with inorganic matrix-grid composites"*. Composite Construction. DOI:10.1061/(ASCE)CC.1943-5614.0000203.

Parisi F., I. Iovinella, A. Balsamo, N. Augenti & A. Prota, (2013). *"In-plane behaviour of tuff masonry strengthened with inorganic matrix-grid composites"*. Composite Part B: Engineering, Vol. 45, pages 1657–66. DOI: 10.1016/j.compositesb2012.09.068.

Parisi F., D. Asprone, L. Fenu & A. Prota, (2015). *"Experimental characterization of Italian composite adobe bricks reinforced with straw fibers"*. Composite Structures, Vol. 122, pages 300–307. DOI:10.1016/j.compstruct.2014.11.060.

Parisi F., C. Balestrieri & D. Asprone (2016). *"Blast resistance of tuff stone masonry walls"*. Engineering Structures, Vol. 113, pages 233-244. DOI:10.1016/j.engstruct.2016.01.056.

Pineda P., (2016). *"Collapse and upgrading mechanisms associated to the structural materials of a deteriorated masonry tower. Nonlinear assessment under different damage and loading levels"*. Engineering Failure Analysis, Vol. 63, pages 72-93. DOI:10.1016/j.engfailanal.2016.02.013.

Polese M., G. M. Verderame, C. Mariniello, I. Iervolino & G. Manfredi, (2008). *"Vulnerability analysis for gravity load designed RC buildings in Naples"*. Journal of Earthquake Engineering, Vol. 12, pages 235-245. DOI: 10.1080/13632460802014147.

Portioli F., C. Casapulla, L. Cascini, (2015) *"An efficient solution procedure for crushing failure in 3D limit analysis of masonry block structures with non-associative frictional joints"*. International Journal of Solids and Structures. Vol. 69–70, pages 252-266. DOI:10.1016/j.ijsolstr.2015.05.025.

Portioli F. & L. Cascini, (2016). *"Assessment of masonry structures subjected to foundation settlements using rigid block limit analysis"*. Engineering Structures, Vol. 113, pages 347-361. DOI:10.1016/j.engstruct.2016.02.002.

Preciado A., (2015). *"Seismic vulnerability and failure modes simulation of ancient masonry towers by validated virtual finite element models"*. Engineering Failure Analysis, Vol. 57, pages 72-87. DOI:10.1016/j.engfailanal.2015.07.030.

Prota A., G. Marcari, G. Fabbrocino, G. Manfredi & C. Aldea, (2006). *"Experimental in-plane behavior of tuff masonry strengthened with cementitious matrix-grid composites"*. Journal Composites Construction, Vol. 10, pages 223–33. DOI: 10.1061/(ASCE)1090-0268(2006)10:3(223).

Quagliarini E., M. D'Orazio & S. Lenci, (2015). *"The properties and durability of adobe earth-based masonry blocks"*. Eco-Efficient Masonry Bricks and Blocks, pages. 361–378. DOI:10.1016/B978-1-78242-305-8.00016-4.

Ramaglia G., G. P. Lignola & A. Prota, (2015) . *"A simplified approach to evaluate retrofit effects on curved masonry structures".* Proceedings of Third International Conference on Smart Monitoring, Assessment and Rehabilitation of Civil Structures SMAR 2015. Antalya (Turkey) 2015. ISBN 9783905594652

Ramaglia G., G. P. Lignola & A. Prota, (2016). *"Collapse analysis of slender masonry barrel vaults"* Engineering Structures, Vol. 117, pages 86-100. DOI:10.1016/j.engstruct.2016.03.016.

Roca P., G. Araiza, (2010). *"Shear response of brick masonry small assemblages strengthened with bonded FRP laminates for in-plane reinforcement strengthening"*. Construction Building Materials, Vol. 24, pages 1372–1384.

Rondelet J.B., (1834). *"Trattato teorico pratico sull'arte di edificare"*. Mantova, Italy.

Rovero L. & F. Fratini, (2013). *"The Medina of Chefchaouen (Morocco): A survey on morphological and mechanical features of the masonries"*. Construction and Building Materials, Vol. 47, pages 465-479. DOI:10.1016/j.conbuildmat.2013.05.025.

Sayın E., B. Yön, Y. Calayır & M. Karaton, (2013). *"Failures of masonry and adobe buildings during the June 23, 2011 Maden-(Elazığ) earthquake in Turkey"*. Engineering Failure Analysis, Vol. 34, pages 779–791. DOI:10.1016/j.engfailanal.2012.10.016.

Schwarz S., A. Hanaor, D.Z & Yankelevsky, (2015). *"Experimental Response of Reinforced Concrete Frames With AAC Masonry Infill Walls to In-plane Cyclic Loading"*. Structures, Vol. 3, pages 306-319. DOI:10.1016/j.istruc.2015.06.005.

Serhal J., O. Deck, M. A. Heib, F.H. Chehade & D.Y.A. Massih, (2016). *"Damage of masonry structures relative to their properties: Development of ground movement fragility curves"*. Engineering Structures, Vol. 113, pages 206-219. DOI:10.1016/j.engstruct.2016.01.054.

Tabbakhha M. & A. M.-F.-Razavi, (2016). *"Analyzing the effect of workmanship quality on performance of unreinforced masonry walls through numerical methods"*. Original Research Article. Computers & Structures, Vol. 167, pages 1-14. DOI:10.1016/j.compstruc.2016.01.013.

Tomazevic M., (2000). *"Earthquake-resistant design of masonry buildings"*. Imperial College Press, London.

Tran V.H., E. Vincens, J.C. Morel, F. Dedecker & H.H. Le, (2014). *"2D-DEM modelling of the formwork removal of a rubble stone masonry bridge"*. Engineering Structures, Vol. 75, pages 448–456. DOI:10.1016/j.engstruct.2014.05.048.

UNI 8942-3. (1986). *"Prodotti di laterizio per murature. Metodi di prova"*. UNI 8942-3, [in Italian].

UNI-EN 101. (2007). *"Metodi di prova per malte per opere murarie – Parte 11: determinazione della resistenza a flessione e a compressione della malta indurita"*. UNI-EN 101, [in Italian].

UNI-EN. 998 (2010). *"Specifiche per malte per opere murarie – Parte 2: Malte per muratura"*. UNI-EN 998 [in Italian].

Ural A., F.K. Fırat, Ş. Tuğrulelçi, M.E. Kara, (2015). *"Experimental and numerical study on effectiveness of various tie-rod systems in brick arches"*. Engineering Structures, Vol. 110, pages 209-221. DOI:10.1016/j.engstruct.2015.11.038.

Valente M. & G. Milani, (2016). *"Non-linear dynamic and static analyses on eight historical masonry towers in the North-East of Italy"*. Engineering Structures, Vol. 114, pages 241-270. DOI:10.1016/j.engstruct.2016.02.004.

Valluzzi M., M. Valdemarca & C. Modena, (2001). *"Behavior of brick masonry vaults strengthened by FRP laminates"*. Composite Construuction. DOI:10.1061/(ASCE)1090-0268(2001)5:3(163).

Valluzzi M.R., D. Tinazzi & C. Modena, (2002). *"Shear behavior of masonry panels strengthened by FRP laminates"*. Construction Building Materials, Vol.16, pages 409–416.

Valluzzi M.R., G. Cardani, L. Binda & C. Modena, (2004). *"Seismic vulnerability methods for masonry buildings in historical centres: validation and application for prediction analyses and intervention proposals"*. 13th. World Conference on Earthquake Engineering, 1 August 2004, Vancouver, B.C., Canada.

Vasconcelos G. & P.B. Lourenço, (2006). *"Assessment of the in-plane shear strength of stone masonry walls by simplified models"*. V International Seminar on Structural Analysis of Historical Constructions - SAHC06, New Delhi, India, pages 843-850.

Walsh K.Q., D.Y. Dizhur, J. Shafaei, H. Derakhshan and J.M. Ingham, (2015). *"In Situ Out-of-Plane Testing of Unreinforced Masonry Cavity Walls in as-Built and Improved Conditions"*. Structures, Vol. 3, pages 187-199. DOI:10.1016/j.istruc.2015.04.005.

Wang C., J.P. Forth, N. Nikitas & S. Vasilis, (2016). *"Retrofitting of masonry walls by using a mortar joint technique; experiments and numerical validation"*. Engineering Structures, Vol. 117, pages 58-70. DOI:10.1016/j.engstruct.2016.03.001.

Whitney C.S., (1937). *"Design of Reinforced Concrete Members Under Flexure and Combined Flexure and Direct Compression"*. ACI Journal 1937, Vol. 33, pages 483-498.

Appendix A

EXPERIMENTAL ACCELERATION PROFILES

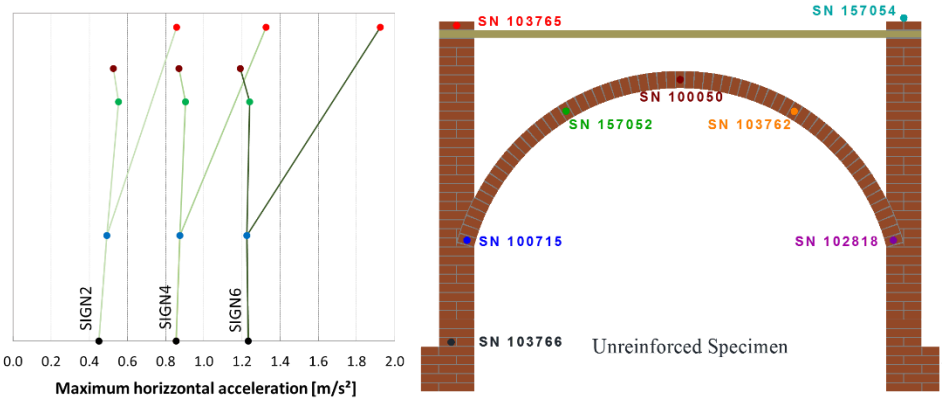

Figure A.1: *Horizontal acceleration profiles (Sturno signal) of the unreinforced vault with, scale factor of 25%, 50% and 75% (curved element and abutments comparison, left side).*

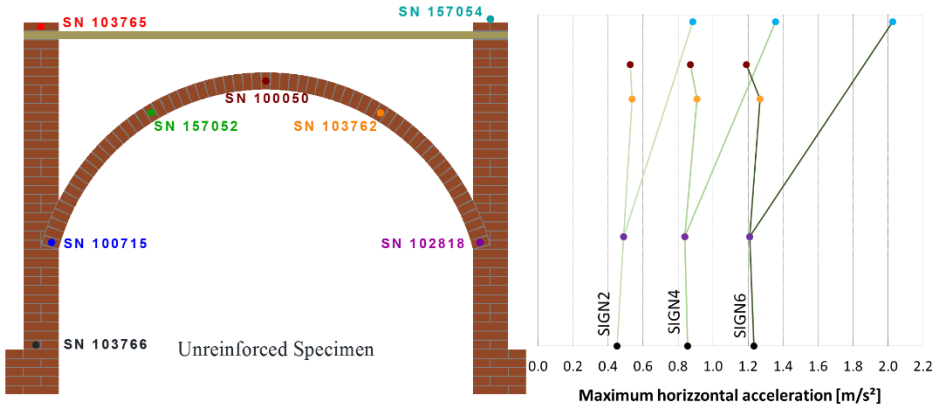

Figure A.2: *Horizontal acceleration profiles (Sturno signal) of the unreinforced vault with, scale factor of 25%, 50% and 75% (curved element and abutments comparison, right side).*

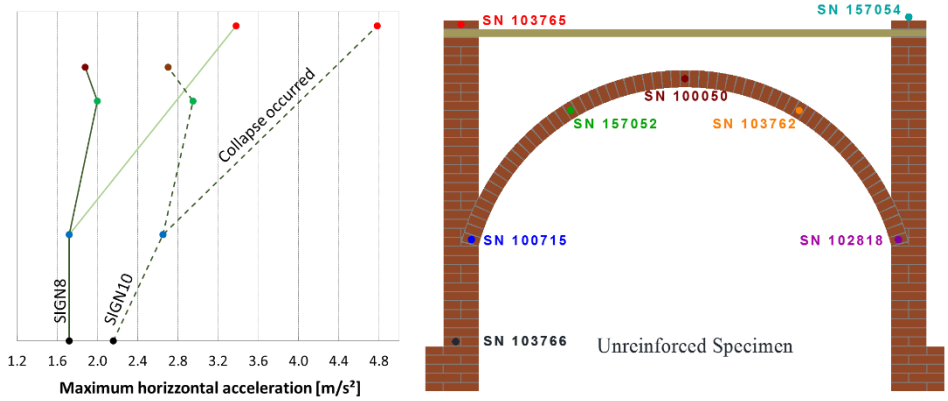

Figure A.3: *Horizontal acceleration profiles (Sturno signal) of the unreinforced vault with, scale factor of 100% and 125% (curved element and abutments comparison, left side).*

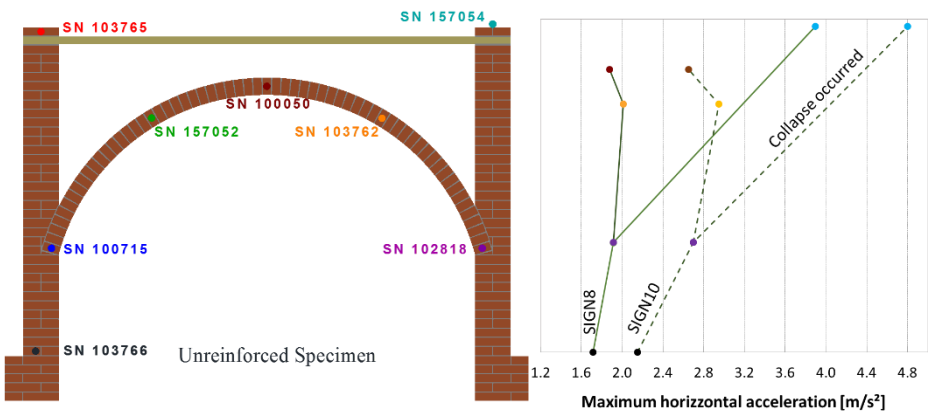

Figure A.4: *Horizontal acceleration profiles (Sturno signal) of the unreinforced vault with, scale factor of 100% and 125% (curved element and abutments comparison, right side).*

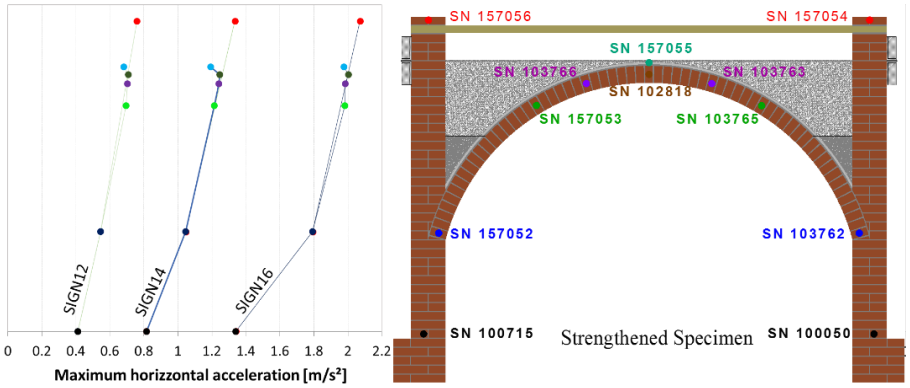

Figure A.5: *Horizontal acceleration profiles (Sturno signal) of the strengthened vault with, scale factor of 25%, 50% and 75% (curved element and abutments comparison, left side).*

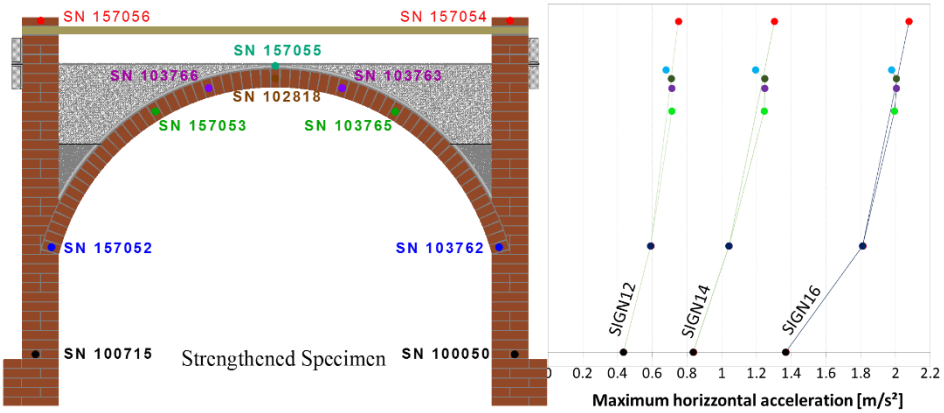

Figure A.6: *Horizontal acceleration profiles (Sturno signal) of the strengthened vault with, scale factor of 25%, 50% and 75% (curved element and abutments comparison, right side).*

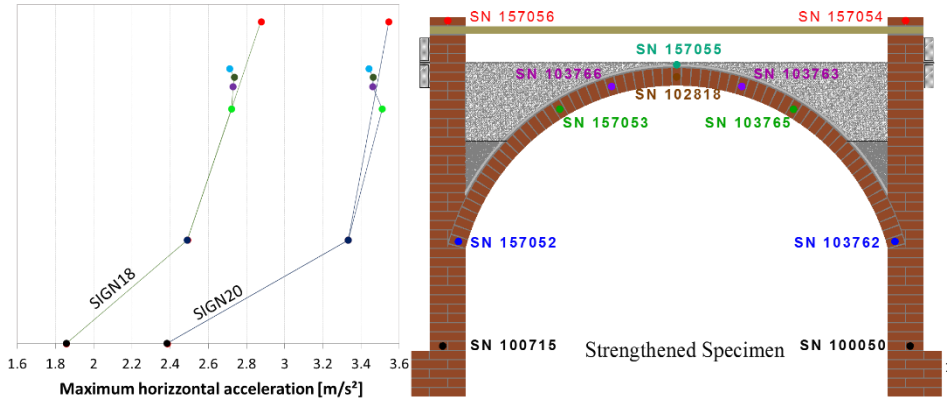

Figure A.7: *Horizontal acceleration profiles (Sturno signal) of the strengthened vault with, scale factor of 100% and 125% (curved element and abutments comparison, left side).*

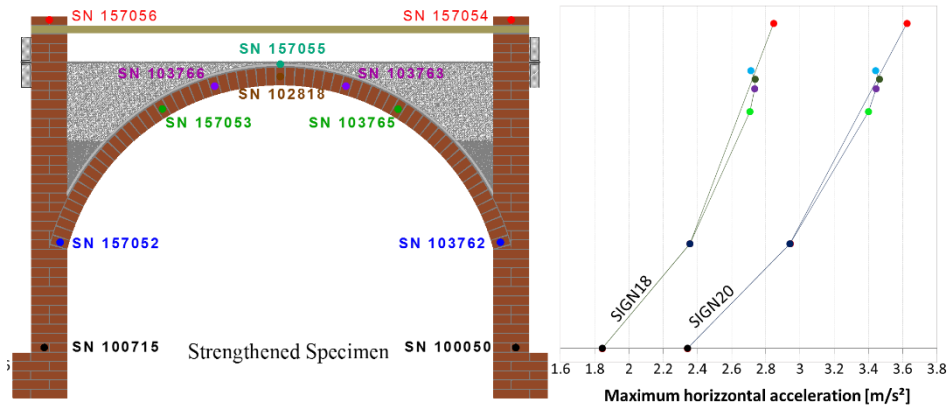

Figure A.8: *Horizontal acceleration profiles (Sturno signal) of the strengthened vault with, scale factor of 100% and 125% (curved element and abutments comparison, right side).*

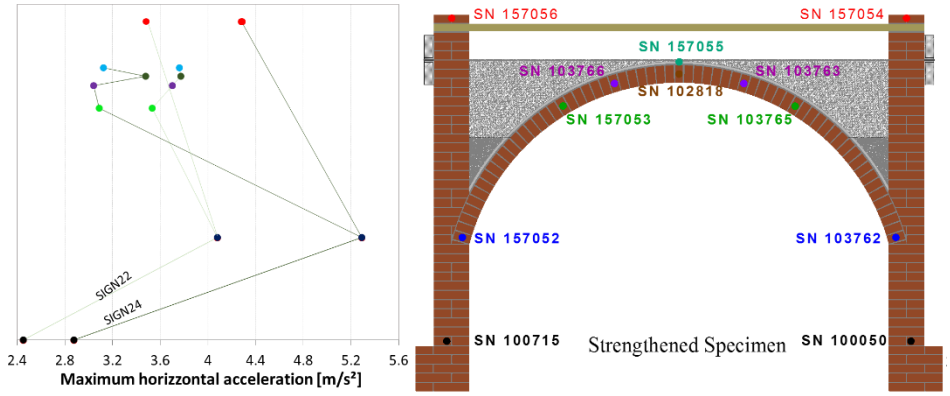

Figure A.9: *Horizontal acceleration profiles (Sturno signal) of the strengthened vault with, scale factor of 135% and 150% (curved element and abutments comparison, left side).*

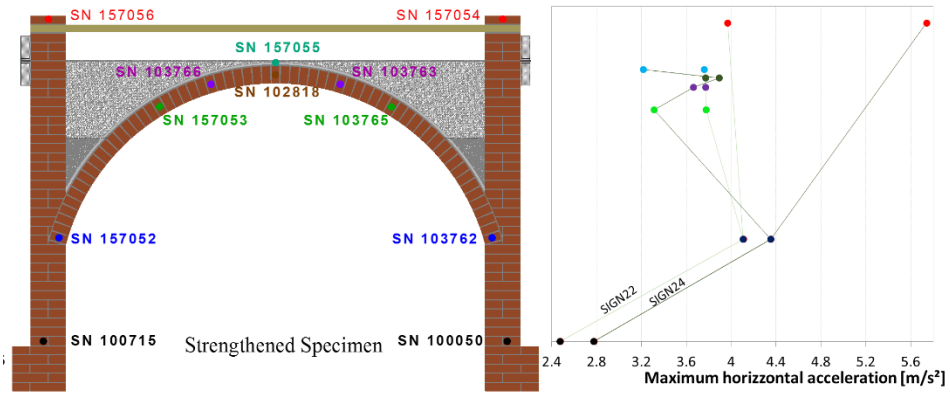

Figure A.10: *Horizontal acceleration profiles (Sturno signal) of the strengthened vault with, scale factor of 135% and 150% (curved element and abutments comparison, right side).*

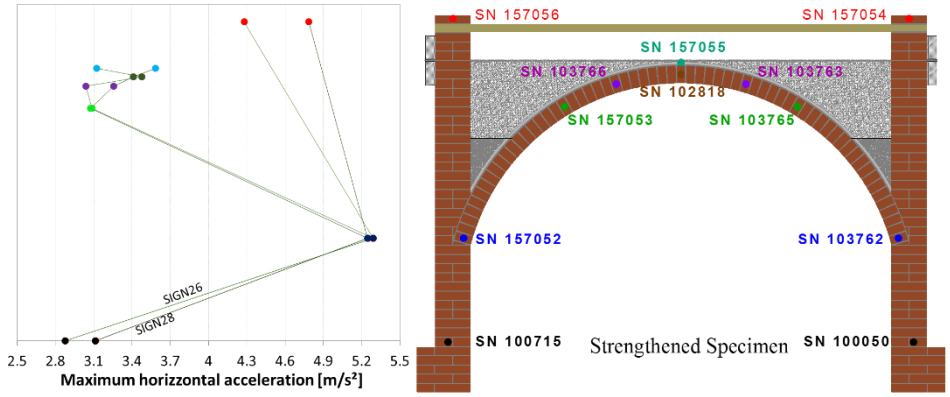

Figure A.11: *Horizontal acceleration profiles (Sturno signal) of the strengthened vault with, scale factor of 160% and 180% (curved element and abutments comparison, left side).*

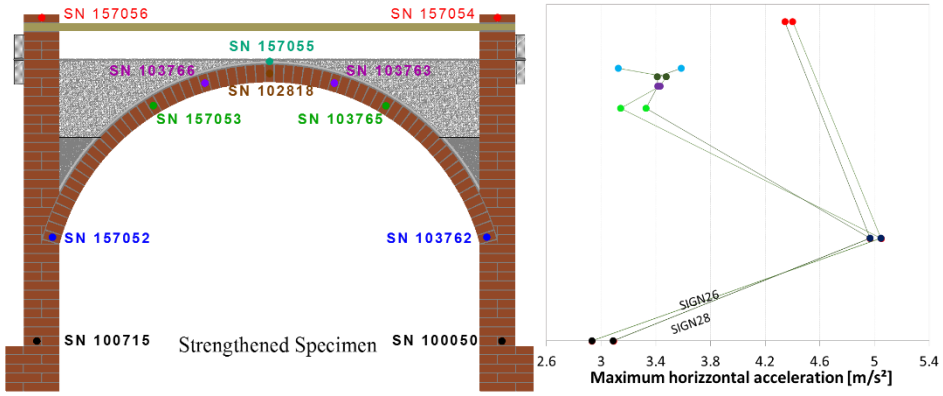

Figure A.12: *Horizontal acceleration profiles (Sturno signal) of the strengthened vault with, scale factor of 160% and 180% (curved element and abutments comparison, right side).*

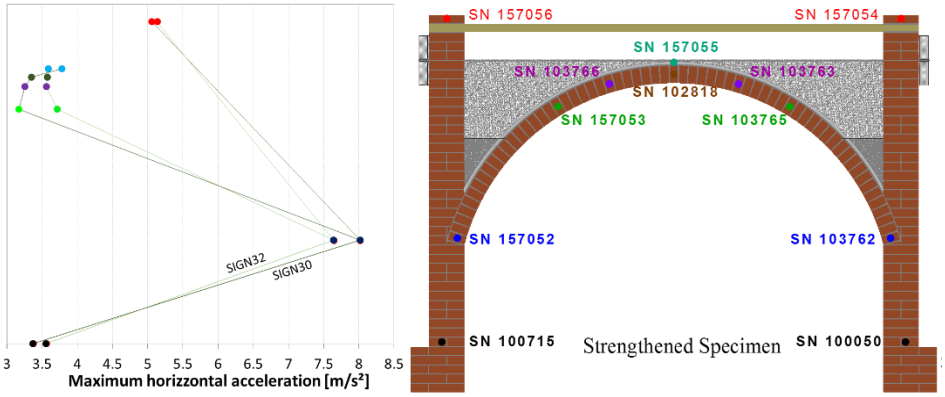

Figure A.13: *Horizontal acceleration profiles (Sturno signal) of the strengthened vault with, scale factor of 190% and 200% (curved element and abutments comparison, left side).*

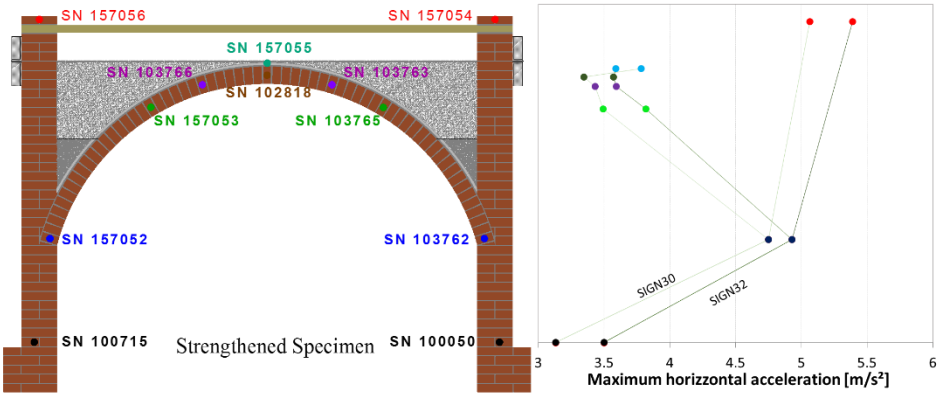

Figure A.14: *Horizontal acceleration profiles (Sturno signal) of the strengthened vault with, scale factor of 190% and 200% (curved element and abutments comparison, right side).*

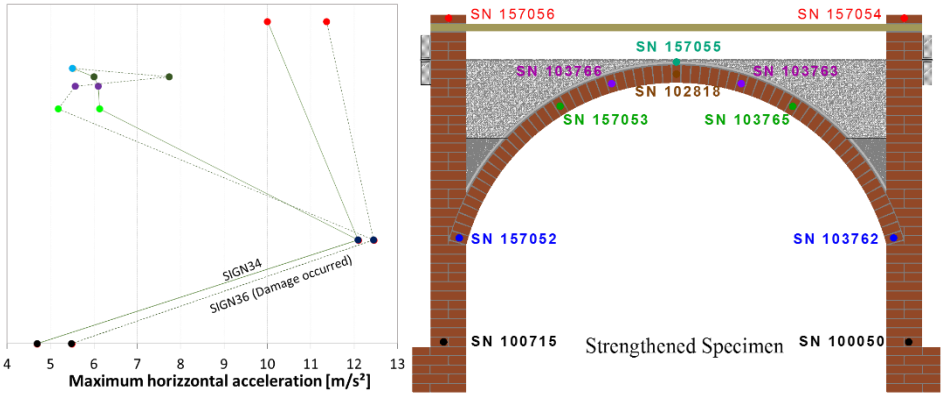

Figure A.15: *Horizontal acceleration profiles (Sturno signal) of the strengthened vault with, scale factor of 220% and 250% (curved element and abutments comparison, left side).*

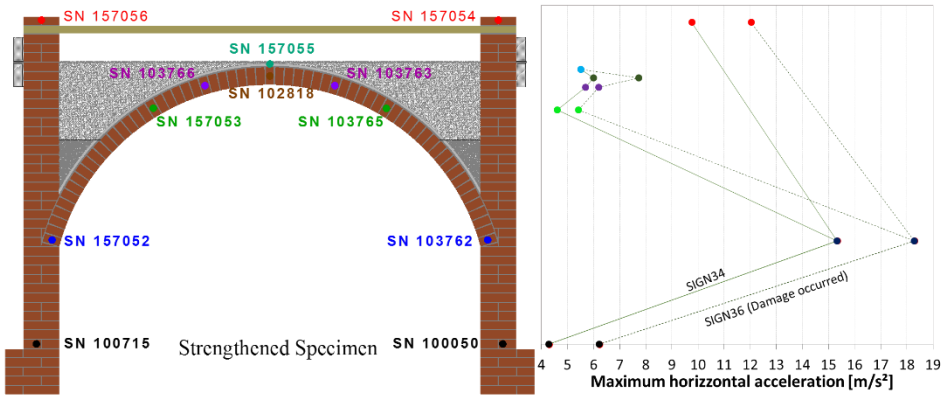

Figure A.16: *Horizontal acceleration profiles (Sturno signal) of the strengthened vault with, scale factor of 220% and 250% (curved element and abutments comparison, right side).*

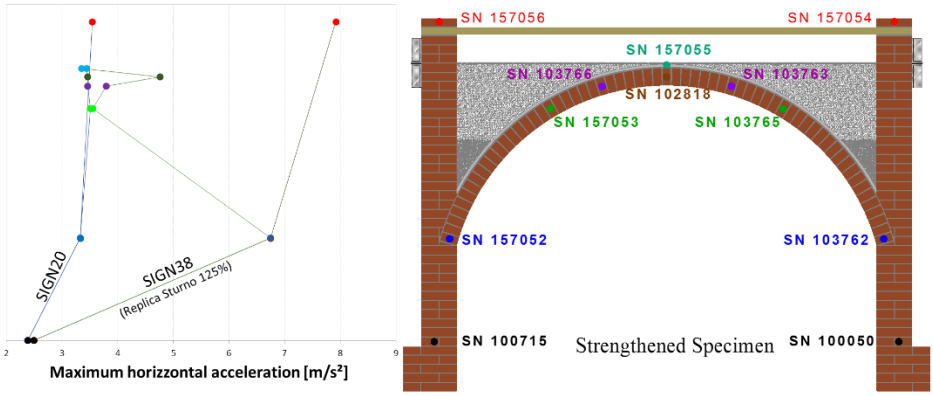

Figure A.17: *Horizontal acceleration profiles (Sturno signal) of the strengthening vault, two replicas with scale factor of 125% (curved element and abutments comparison, left side).*

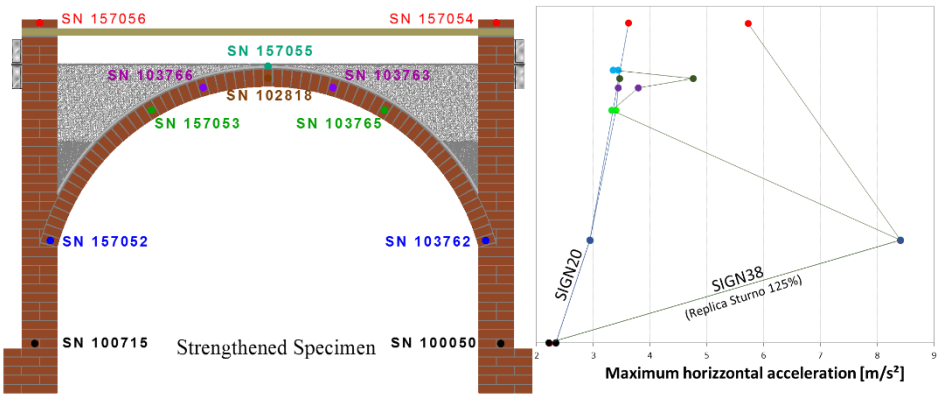

Figure A.18: *Horizontal acceleration profiles of (Sturno signal) the strengthening vault, two replicas with scale factor of 125% (curved element and abutments comparison, right side).*

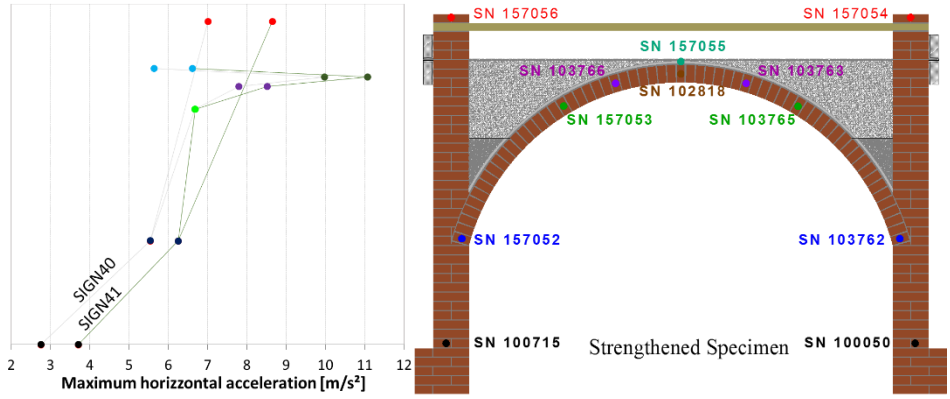

Figure A.19: *Horizontal acceleration profiles (Gemona signal) of the strengthened vault with, scale factor of 100% and 125% (curved element and abutments comparison, left side).*

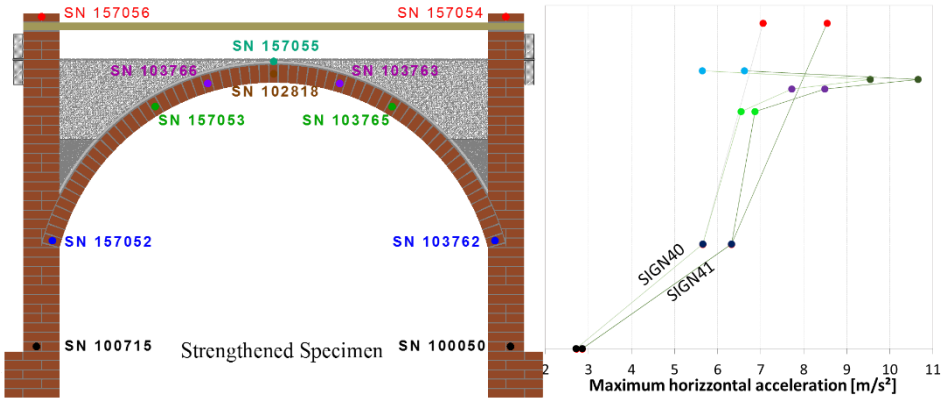

Figure A.20: *Horizontal acceleration profiles (Gemona signal) of the strengthened vault with, scale factor of 100% and 125% (curved element and abutments comparison, right side).*

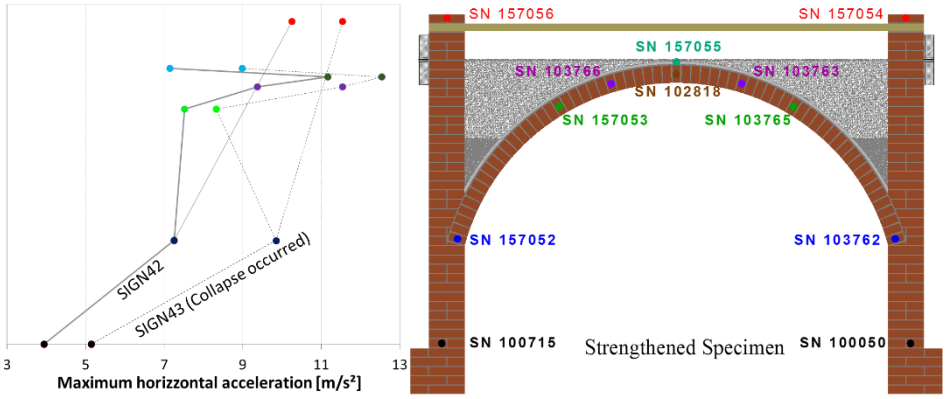

Figure A.21: *Horizontal acceleration profiles (Gemona signal) of the strengthened vault with, scale factor of 150% and 175% (curved element and abutments comparison, left side).*

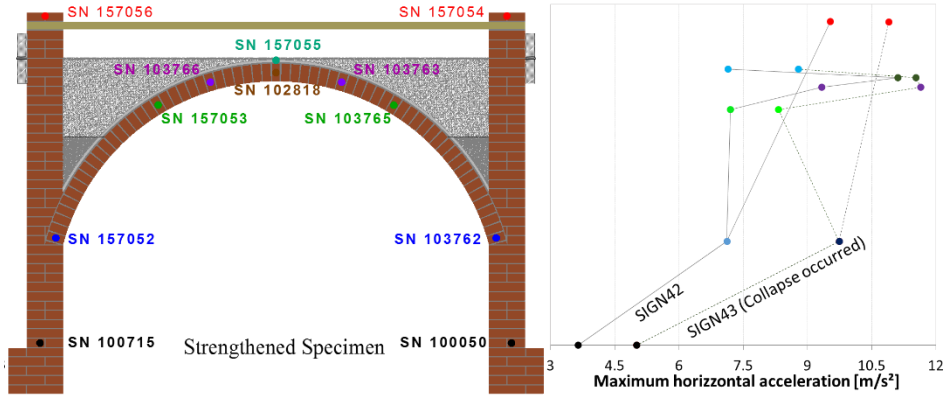

Figure A.22: *Horizontal acceleration profiles (Gemona signal) of the strengthened vault with, scale factor of 150% and 175% (curved element and abutments comparison, right side).*